Sentinel-3 ©ESA/ATG

Experimental Assessment of Sea State Bias for Low Resolution Mode and SAR Altimetry

Nelson Ribeiro Pires

Programa Doutoral em Engenharia Geográfica

Departamento de Geociências, Ambiente e Ordenamento do Território

2018

Orientador

Maria Joana Fernandes, Professor Auxiliar

Faculdade de Ciências, Universidade do Porto

Porto, Portugal

Coorientador

Christine Gommenginger

National Oceanography Centre

Natural Environment Research Council

Southampton, UK

EXPERIMENTAL ASSESSMENT OF SEA STATE BIAS FOR LOW RESOLUTION MODE AND SAR ALTIMETRY

A Thesis submitted to
University of Porto
Faculty of Sciences

For the Doctoral Programme in
Surveying Engineering

Nelson Ribeiro Pires
2018

Department of Geosciences, Environment and Spatial Planning

Supervisor
Maria Joana Fernandes
Department of Geosciences, Environment and Spatial Planning
University of Porto, Faculty of Sciences, Porto, Portugal

Co-supervisor
Christine Gommenginger
National Oceanography Centre
Natural Environment Research Council, Southampton, UK

September 11, 2018

THIS PAGE IS INTENTIONALLY LEFT BLANK.

Experimental Assessment of Sea State Bias for Low Resolution Mode and SAR Altimetry

Nelson Ribeiro Pires

Abstract

Over the last 25 years, satellite radar altimetry has already shown its ability to revolutionise our understanding of the physical ocean. Nowadays, this remote sensing technique can provide measurements for a number of applications involving most of the geoscience fields, from ocean variability or ice topography, to hydrology or coastal monitoring.

The efficiency of this technique is entirely dependent on the accuracy of the measured altimeter range, satellite orbit, and on the correction models accounting for the errors affecting the observations. One of the major contribution in the error budget linked to altimeter radar measurements, is the sea state bias, an altimeter ranging error caused by the influence of sea-state effects in the area surveyed by the satellite.

This thesis aims to understand, develop, test and validate innovative methods and solutions associated with the altimetric range bias induced by sea-surface waves, being the ultimate goal, the generation of reliable sets of sea state bias corrections, to be implemented in the altimetric observations retrieved by past, present, and future missions.

To accomplish the purposed goal, the research is divided into three main chapters, corresponding to the output of the three scientific papers written during this period, the first one proposes a new empirical sea state bias model for Jason-1 mission using information retrieved entirely from altimetric data; the second describes a more refined parametrization, extending the model methodology to all reference missions (TOPEX, Jason-1, Jason-2 and Jason-3); and the third propose a synergetic approach using Jason-3, Sentinel-3 and Sentinel-1 sea-state related parameters in order to find new correlators as model predictors for sea state bias estimations.

With the three scientific articles, this thesis provides an integrated overview of the conducted study on the sea state bias in different sea-state regimes, and performed for all reference missions on a global scale.

Keywords: remote sensing; satellite altimetry; sea state bias; non-parametric model; smoothing splines; directional wave spectra

Estudo e avaliação experimental do erro provocado pelo estado do mar na Altimetria por Satélite

Nelson Ribeiro Pires

Resumo

Durante os últimos 25 anos, a altimetria radar já deu provas da sua capacidade para revolucionar a nossa compreensão sobre o oceano. Atualmente, esta técnica de detecção remota é capaz de fornecer informação precisa para uma variedade aplicações que envolvem a maioria dos campos ligados às geociências, desde o estudo da variabilidade oceânica ou da topografia do gelo, até à hidrologia e monitorização das zonas costeiras.

A eficiência desta técnica é totalmente dependente da precisão das medidas efetuadas, da órbita do satélite e dos modelos de correção responsáveis pelos erros que afetam as observações. Uma das principais contribuições para a imprecisão destas observações, deve-se ao erro relativo ao estado do mar, um erro de variação do altímetro, devido à influência dos efeitos do estado marítimo na área iluminada pelo satélite.

A presente tese tem como objetivo, a compreensão, desenvolvimento, teste e validação de métodos e soluções inovadoras associadas ao erro do sinal altimétrico induzido pela ondulação marítima da superfície oceânica, tendo como objetivo final a geração de correções relativas ao estado do mar, de modo a serem depois implementadas nas observações das missões altimétricas mais recentes e futuras.

Para a execução do objetivo proposto, o estudo divide-se em três capítulos principais, correspondendo aos três artigos científicos escritos durante este período. O primeiro artigo propõe um novo modelo empírico aplicado à missão Jason-1 para a correção do efeito do estado marítimo; o segundo descreve uma parametrização mais refinada, estendendo a metodologia do modelo a todas as missões de referência (TOPEX, Jason-1, Jason-2 e Jason-3); o terceiro artigo propõe uma abordagem sinergética entre as missões Jason-3, Sentinel-3 e Sentinel-1, com a finalidade de encontrar novos parâmetros de modelação para as estimativas do erro no sinal altimétrico devido ao efeito do estado marítimo.

Com os três artigos científicos apresentados, esta tese fornece uma visão geral e integrada da avaliação feita sobre o erro devido ao estado do mar, aplicado a todas as missões de referência, à escala global.

Palavras chave: deteção remota; altimetria por satélite; modelo não-paramétrico; espetro direcional

Acknowledgements

During this period of four years of research work, there was a number of people who helped me finding the right motivation and perseverance, the calmness, and even the humour to surpass and finish this stage of my life. To each one of them, I would like to express my gratitude:

Firstly, I would like to express my sincere gratitude to my supervisor Prof. Joana Fernandes for her trust and continuous support, not only during this Ph.D. period, but over the last ten years we have been working together. Her example, motivation and guidance always helped me to believe that this endeavour would be possible. More than the professional connection, I would like to thank her for the long years of our friendship, which is perhaps the main reason that makes me feel happy in my workplace and with what I do.

Secondly, my sincere thanks to my co-supervisor, Dr. Christine Gommenginger, who despite not knowing me professionally at the beginning of this Ph.D., gladly accepted to support this work, always being available to give guidance and suggestions in the most critical times when it was necessary.

My sincere thanks also goes to Dr. Remko Scharroo, who supported my work from the very beginning with his pragmatic and intelligent way of solving problems. His trust and shared knowledge have always been a valuable help throughout the course of this Ph.D.

At the office, I would like to thank my fellow labmates, colleagues and friends, Telmo Vieira and Eliana Vieira, for their support and friendship. Everything becomes easier when we work on a daily basis with people we like, and I could not wish better companions than these two.

From Department of Geosciences, Environment and Spatial Planning, my sincere thanks goes to my colleagues and friends, Ana Cláudia and Lia Duarte, for their cooperation and support, for our conversations during the lunch times, but above all, for their heartfelt and deep friendship over the past years and those to come.

To my oldest friends, Raquel Caetano and David Fernandes, I would like to thank their affection and companionship over the years. They were always present, in person and online, sharing with me the victories and anxieties of this adventure. The years go by, and our friendship remains the same from day one.

To my CIBIO's friends, João Campos, Ana Serronha, Helena Santos and Sofia Vaz, almost all of them finishing their own Ph.D. during this time, I would like to thank them for the dinners and lively conversations, the many laughs during the board games, but fundamentally, all the support and help they gave me to carry on with good mood.

If I'm proud and grateful with the person and the professional who I am today, I owe it to my parents, my sister, my brother in law, and my two beautiful nieces. These six people shaped my personality with their love and affection, and I want to thank them for being part of me and for giving me what is most important for living a truly happy life.

Last but not the least, I want to thank my cat, Paco, for the hours and hours he slept on my legs as I worked through the countless nights, and who will probably be one of the most educated cats in history.

List of Acronyms

ASAR	Advanced SAR (EnviSat)
AVISO	Archiving, Validation and Interpretation of Satellite Oceanographic data (France)
C-band	Microwave frequencies in the range 4 – 8 GHz
CLS	Collecte, Localisation, Satellites
CNES	Centre National d'Etudes Spatiales (French Space Agency)
CryoSat-2	Earth Explorer Opportunity Mission-2
EC	European Commission
ECMWF	European Centre for Medium-range Weather Forecasting
EnviSat	Environmental Satellite
ERS-1, -2	European Remote-Sensing Satellite
ESA	European Space Agency
EUMETSAT	European Organization for the Exploitation of Meteorological Satellites
GAM	Generalized Additive Model
GDR	Geophysical Data Record(s)
GEOS-3	Geodynamic Experimental Ocean Satellite
GEOSAT	Geodetic/Geophysical Satellite
GFO	GEOSAT Follow-On
GNSS	Global Navigation Satellite System
HY-2A	Haiyang-2A
ISRO	Indian Space Research Organization
Jason-1, -2, -3	United States/France altimeter satellites
JPL	Jet Propulsion Laboratory

K_a-band	Microwave frequencies in the range 26.5 – 40 GHz
K_u-band	Microwave frequencies in the range 12 – 18 GHz
LRM	Low Resolution Mode
MSS	Mean Sea Surface
NASA	National Aeronautics and Space Administration
NCEP	National Centres for Environmental Prediction
NOAA	National Oceanic and Atmospheric Administration
OCN	Sentinel-1 Level-2 ocean products
OSW	Ocean Swell Spectra (from Sentinel-1 OCN products)
RADS	Radar Altimeter Database System
SAR	Synthetic Aperture Radar
SARAL	Satellite with ARgos and ALtiKa
SeaSat	Seafaring Satellite
Sentinel-1	Copernicus: Sentinel-1 - The SAR Imaging Constellation for Land and Ocean Services
Sentinel-3	Copernicus: Sentinel-3 - Global Sea/Land Monitoring Mission including Altimetry
SLA	Sea Level Anomaly
SSB	Sea State Bias
SSH	Sea Surface Height
SSHA	Sea Surface Height Anomaly
SWH	Significant Wave Height (H_s)
TOPEX/Poseidon	Topography Experiment/Poseidon
USN	United States Navy
WAM	Third generation wave model developed at ECMWF
WW3	Third generation wave model developed at NOAA/NCEP

Glossary

The following list of terms and definitions are reprinted from the tutorial [1].

Along-track	Data chronologically ordered, following the satellite "ground track", i.e. the virtual track left by the radar beam on the ground.
Backscatter coefficient	The amplitude of the useful radar altimeter echo signal with respect to the emission amplitude gives the backscatter coefficient, sigma0. The backscatter coefficient can be related to wind speed.
Brown model	Over an ocean surface, the radar altimeter echo waveform has a characteristic shape that can be described analytically (the Brown model).
Collinear	Measurements along repeated satellite ground tracks.
Crossover	Measurements where ascending and descending tracks cross over oceans at different epochs.
Cycle	Satellite repetitivity, or repeat orbit.
Dynamic topography	Sea level driven by thermodynamic processes in the ocean.
Geophysical corrections	The radar pulse used to measure altimetry is subjected to a number of disturbances as it passes through the atmosphere and when it is reflected by the sea surface.
MSL	Mean Sea Level: The sea surface height averaged across all the oceans of the globe.
MSS	Mean Sea Surface: Permanent component of the sea surface height.
Range	The altimeter satellite-to-surface distance, deduced from the return echo time delay.

Retracking	Retracking altimetry data is done by computing the departure of the waveform's leading edge from the altimeter tracking gate and correcting the satellite range measurement (and surface elevation) accordingly.
SLA	Sea Level Anomalies: Difference between the observed Sea Surface Height (SSH) and the Mean Sea Surface (MSS).
SSB	Sea State Bias: Geophysical correction due to the sea-surface state.
SSH	Sea Surface Height: Height measured with respect to an arbitrary reference level, called the reference ellipsoid, includes the geoid and the dynamic topography.
SSHA	Sea Surface Height Anomalies or SLA.
Waveform	The magnitude and shape of the radar altimetry return echoes.

Contents

List of Figures

List of Tables

Chapter 1

Introduction

During the last 25 years, the technique of satellite altimetry has been providing a unique tool for the understanding of global ocean circulation, accomplishing significant progress in the study and knowledge of processes involving climate change. The efficiency of this technique is entirely dependent on the accuracy of the measured altimeter range, satellite orbit, and on the correction models accounting for the errors from different origins (instrumental, range and geophysical) that affect the altimeter observations. One of these inherent errors is the so-called sea state bias (SSB), which is an altimeter range error caused by the influence of ocean surface waves on the radar altimeter measurements, whose study will be the main focus of this thesis.

The SSB effect arises mainly from the interactions between the altimetric signal and wind-driven ocean gravity waves, since the surface scattering elements do not contribute equally to the radar return. Usually, this effect is characterized by three different contributions: (a) An electromagnetic bias evidenced by the signal-surface interactions, where ocean wave troughs are better radar reflectors than wave crests, thus overestimating the measured satellite-to-surface range. (b) A skewness bias, which can occur due to the assumption in the onboard algorithms that the probability density function of heights is symmetric, while in reality it is skewed. (c) A tracker bias, which can occur due to retracking effects and an imprecise tracker determination of the midpoint location of the altimeter return or waveform leading edge [2].

In classical hydrodynamics, wind-driven waves of a given height are usually generated by complex wave systems moving freely across the ocean. Most of the times, these systems are composed from long-period sinusoidal waves with short slopes generated by a distant storm and/or from locally storm-generated trochoidal waves, sustained by the local wind, with steep facets and large wave slopes. When a given microwave sensor overflies an oceanic region with a particular sea-state characterized by ocean surface gravity waves, the accuracy of measurements is limited in part by how the sea roughness influences the reflected signal, perturbing all microwave frequencies with wavelengths of a few centimetres. This effect occurs on all kind of sensors operating in the microwave range of frequencies of the electromagnetic spectrum, since the Ka-, Ku-, C-, and S-bands regularly used for satellite altimetry [2], [3], until the L-band frequency usually adopted for Global Navigation Satellite Systems Reflectometry (GNSS-R)

altimetry [4]. In addition to the microwave sensors, recent studies show that even laser altimeters operating in the visible region of the electromagnetic spectrum, are also affected by the roughness of ocean sea surface [5].

The SSB noise on the altimetric signal, depends mainly on the noise of the significant wave height H_s derived from the altimeter, and its relationship with the backscatter power σ_0 often used to derive the wind speed U10. Thus, the most common approach used in SSB estimation is by means of empirical modelling using H_s and σ_0 or U10. Due to the extreme complexity of the surface ocean waves systems propagating freely in various directions and interacting non-linearly, the geophysical wave information of H_s and U10 provided by the satellite altimetry technique is not sufficient to explain some of the sea surface height (SSH) variability associated with ocean waves and their multiple interactions while propagating across the sea. In order to overpass this insufficient information on the non-linear characteristics of the oceanic surface, several studies have tried different approaches to explain more of the remaining SSH variability by using additional sea-state parameters. These extra information could be retrieved from a variety of distinct sources, such as parameters indirectly derived from the altimetric signal [3], [6], obtained from numerical wave models [7]–[9], or through the wave system bi-dimensional spectral response expressing the mean sea-surface elevation variance due to ocean waves as a function of frequency and propagation direction.

Over the past years, different empirical approaches have been adopted in the modelling of SSB, leading to progressively improved predictions and better explaining the remaining SSH variability. In the early years, parametric formulations were carried out by [10], [11] estimating SSB from a multiple linear regression approach on the basis of two predictor variables, the H_s and U10 derived from the altimetric signal. In the subsequent years, more sophisticated statistical approaches were used, leading to improved SSB estimates obtained from non-parametric regression methods based on kernel smoothing approaches [12], local linear kernel [13], [14], and smoothing splines [15] using the same two altimeter-derived predictors. More recently, [7] tested the use of additional wave field statistics available in numerical ocean wave model fields to develop new SSB correction models, leading to an enhanced 3-dimensional SSB model using the classical altimetric predictors of H_s and U10, but also the mean wave period (T_z), retrieved from a third-generation global wave model [8].

Nowadays, SSB is the range correction that represents the most significant challenge for further improvement in the altimetric error budget of past and present missions. The studies conducted so far, using different theoretical and empirical approaches, helped to better understand not only how the sea-state roughness affects the altimetric signal and related physical phenomena, but also the instrumental component associated with the algorithmic choices used to retrieve the geophysical information from the altimeter raw signal. With an order of magnitude ranging between 3%-4% of H_s, this centimetre-scale measurement bias remains one of the largest sources of uncertainty linked with the altimetric signal.

1.1 Aim and Objectives

This research aims to understand, develop, test and validate innovative methods and solutions associated with the altimetric range bias induced by ocean surface waves, the *sea state bias*. The ultimate goal is the development of appropriate methodologies to find new ways of minimizing the impact of sea-state effect on the altimeter radar pulse, providing specific solutions for each altimetric mission and promoting an effective integration on the set of geophysical corrections to be applied at regional and global scales.

1.2 Thesis Outline

This thesis is arranged into five main chapters, after the present one, as follows:
Chapter 2 presents an overview of the theoretical foundations with the purpose of putting into context the added value of this research with respect to the state-of-the-art. It begins with a brief introduction to the satellite altimetry measurement principles, followed by an historical description of the main contributions given by each mission to the development of this technique. The chapter follows with a detailed explanation on the effect of surface waves and wind on the altimeter return, putting into context the thorough characterization of wind-generated waves, presented later. An overview of the statistical description of wave parameters is given, where the most commonly used variables of significant wave height, wind speed at the sea surface, wave period and wave propagation direction, are described and related between each other. The theoretical concept of directional wave spectrum, regularly used to illustrate and interpret complex wind-generated wave systems, is introduced in order to better understand the ocean swell spectra products, delivered by the C-band synthetic-aperture radar sensor coupled on Sentinel-1 mission. This chapter ends with a brief literature review of the sea state bias correction and its different components, as well as the various theoretical and empirical approaches, currently available to estimate this geophysical correction for radar altimeters. The following three chapters (3 to 5) constitute the core of this thesis, containing the conducted research, organised in the form of three research papers, the first two published in Remote Sensing and IEEE Transactions on Geoscience and Remote Sensing respectively, and the last in the process of submission for publication. Although the content of these chapters has been extracted from the respective articles, all information has been formatted in a similar fashion, to make this thesis more uniform and consistent.

Chapter 3 presents the first article written in the scope of this research, where a conceptually simple formulation is proposed for a new empirical SSB model, using information retrieved entirely from altimetric data. For this, non-parametric regression techniques have been performed, based on penalized smoothing splines adjusted to each model predictor, and then combined in a generalized additive model (GAM). In this approach, the classical altimetry derived estimations of H_s and U10 has been used, but combined with a coupled mediator parameter designed by the mean wave period also derived from radar altimetry. This additional third predictor exhibits im-

provements in the model performance, explaining some of the SSB variability, especially in swell ocean regions with medium-high H_s and low U10. For validation purposes, a collinear analysis of scaled sea level anomalies (SLA) variance differences has been performed and demonstrated a conformity between the proposed model and the established SSB models usually available in the official altimetric geophysical data records (GDR). The new formulation was tested on Jason-1 mission, and proved to be a fast and reliable approach for SSB computation, in line with the well-settled SSB corrections, showing positive results for a wide range of sea-state conditions. The proposed methodology is also computationally efficient and flexible enough to be adapted for new launched missions, when little information is still available.

Chapter 4 presents the second article developed in the scope of this research, where the proposed SSB formulation, first tested on Jason-1 mission, was improved with a more refined parametrization, and extended to all reference missions (TOPEX, Jason-1, Jason-2 and Jason-3). An in-depth study of the design, development and assessment was conducted to inspect five SSB model designs tuned with different degrees of freedom and basis functions, using two and three predictors. Two different empirical algorithms for altimeter ocean wave period have been tested and implemented, improving the SSB model performance in some ocean regions. After having tested the various approaches, the selected model was subsequently used to evaluate the outputs obtained with four training datasets of different lengths with 120, 50, 20 and 10 cycles of data. Systematic comparisons using collinear analyses and temporal evolutions of SLA variance differences, were conducted between the new proposed model and the established SSB models usually available in the official altimetric GDR. Results showed that this method can derive a reliable SSB model with only 20 cycles of altimeter data, making it an interesting option to rapidly estimate SSB for newly-launched missions. The instrumental component of the SSB (tracker bias) was also assessed by comparing the various SSB models during the altimeter missions' tandem phases, leading to the conclusion that the instrumental component of SSB is larger for Jason-2 than for the other missions.

Chapter 5 presents the third main study conducted in the scope of this research, where a synergistic approach using Jason-3, Sentinel-3 and Sentinel-1 sea state related parameters is proposed, with the goal to inspect the correlations between the swell systems and the altimeter-derived parameters mostly used as predictors for SSB estimations. This approach makes use of Sentinel-1 Level-2 (L2) Ocean (OCN) products, operating in the nominal acquisition Wave mode (WV) for wave applications, which can provide the two-dimensional ocean surface swell spectrum in the form of imagettes with a spatial resolution of 20 km by 20 km, and additional parameters, such as the dominant wave direction, length and height for each wave partition derived from the ocean wave spectra (integrated wave parameters) and from the imagette (image statistics). This study spans the year 2017, for which the different data sources were collocated and analysed in the sense of using swell information retrieved from Sentinel-1 L2 products in order to study the possible impact of these sea state correlators on the SSB estimations. An in-depth study was also carried out to determine how the measures H_s and U10 of Sentinel-3 SAR mode (SARM) differ from the altimeter Pseudo-Low Resolution mode (PLRM) measures. The final goal of this

work, is the derivation of new SSB models for Jason-3 and Sentinel-3, using improved descriptors and statistical information about their inter-dependencies.

Chapter 6 depicts the main conclusions of this research work, highlighting the main contribution and achievements of the proposed techniques and methodologies for minimizing the repercussion of sea-state effects on the altimeter radar pulse. At the end, several suggestions are made, acknowledging further developments and delivering new perspectives or possible directions for future research.

Chapter 2

Theoretical Background

2.1 Satellite altimetry measurement principles

The basic principle of satellite altimetry can be simply described as a remote sensing technique for measuring height, since the radar altimeter is an active sensor which transmits short pulses of energy, vertically downwards towards the ocean surface, and deducing the range by measuring the pulse travel time between the satellite antenna and the illuminated surface [2]. The range R from the satellite to the instantaneous sea surface is estimated from the round-trip travel time by:

$$R = \hat{R} - \sum_{j} \Delta R_j \tag{2.1}$$

where $\hat{R} = ct/2$ is the range computed neglecting refraction based on the free-space speed of light c and ΔR_j, $j = 1,\ldots$ are corrections for the various components of atmospheric refraction and for biases between the actual scattering surface and the actual mean sea level at the air-sea surface within the altimeter footprint [2]. Figure 2.1 shows the variables used to describe the satellite altimetry measurement principle. Along the radial line between the satellite and the Earth's centre of mass, the altimeter measures the height or range $R(\chi, \psi, t)$ of the satellite above the sea surface, where χ is the latitude and ψ is the longitude corresponding to the passage time t of the satellite. The other radial variable is the height $H(\chi, \psi, t)$ of the satellite above an arbitrary *reference ellipsoid*, where the length of one of the axes at the Equator is chosen so that the ellipsoid coincides with the mean sea level, and which is known relative to the Earth's centre of mass [16].

The difference between H and R is represented by $h_s(\chi, \psi, t)$, corresponding to the height of the sea surface above the ellipsoid in the following form:

$$h_s = H - R \tag{2.2}$$

and which relative to the geoid undulation $N(\chi, \psi)$, takes the form of:

$$\zeta(\chi, \psi, t) = h_s(\chi, \psi, t) - N(\chi, \psi) \tag{2.3}$$

The height ζ describes the sea level variability traduced by a non-equilibrium surface of a dynamic ocean, apart from geostrophic flows, tides, atmospheric pressure changes, and seasonal heating and cooling. The purpose of satellite altimetry is to measure ζ and determine the sea surface response to a variety of geophysical forcing.

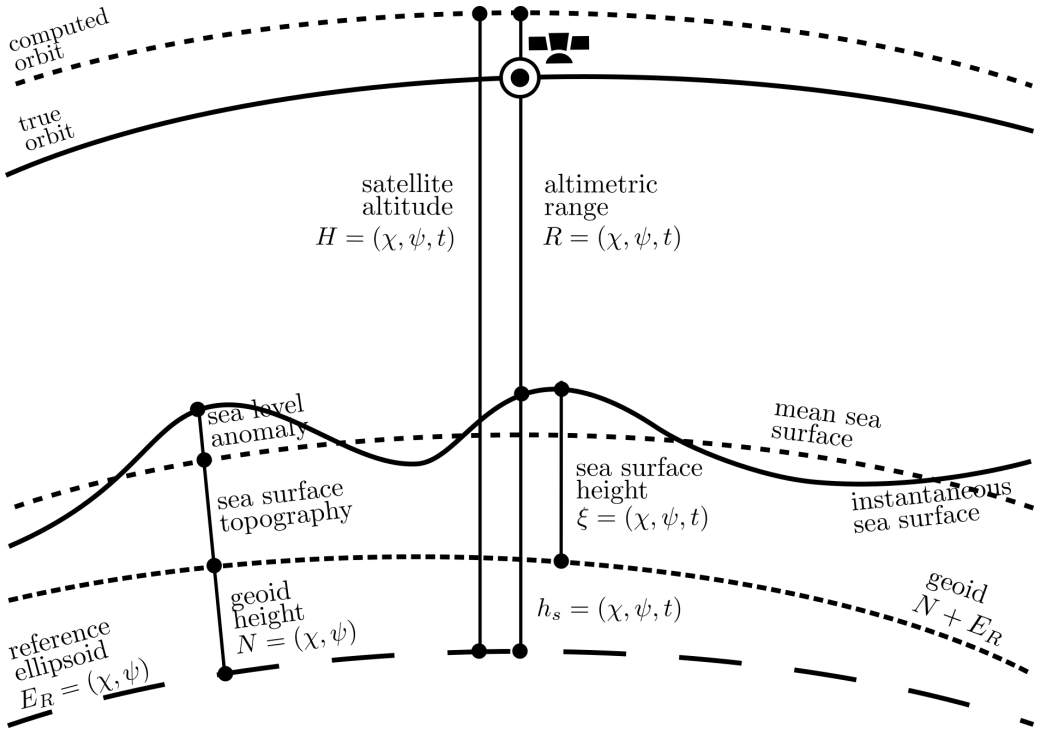

Figure 2.1: Definition sketch of the geometry of the altimetric measurement of the sea surface topography from satellite altimetry, showing the satellite orbit, the reference ellipsoid, geoid height and height of the sea surface, where χ is the latitude and ψ is the longitude. (Adapted figure from [16])

The final goal of satellite altimetry is to determine the sea surface height (SSH represented as h_s) to within 2-3 cm accuracy, and as shown by equation 2.2, this determination depends on the accurate measurement of the satellite height H above the ellipsoid from precise orbit determination and its range R from the sea surface [16].

The accuracy of SSH estimated from radar altimeters is directly linked with the achieved accuracies for corrections applied to the range R and orbit determination:

$$h_s = h - (R + \Delta R_{dry} + \Delta R_{wet} + \Delta R_{ion} + \Delta R_{ssb}) \tag{2.4}$$

where h_s is the altimeter derived SSH estimate, h is the height of the satellite's centre of mass above the reference ellipsoid determined from precise orbit determination (POD) analysis, R is the nadir range from satellite's centre of mass to the sea-surface and corrected for instrument effects, ΔR_{dry} is the atmospheric refraction range delay caused by the dry gases component of the troposphere, ΔR_{wet} is the atmospheric refraction range delay caused by the water vapour and cloud liquid water content of the troposphere, ΔR_{ion} is the atmospheric refraction range delay caused by the free electron content of the ionosphere, and ΔR_{ssb} is the range correction accounting for the interaction of the radar signal and the sea surface.

Altimetric Missions

The development of altimeter technology was a constant effort for the last 40 years. After the successful tests during the Skylab missions (NASA:1973), the technique of satellite altimetry continued to be developed in the following missions GEOS-3 (NASA:1975) and SeaSat (NASA/JPL:1978). GEOS-3 was the first dedicated radar altimeter mission of its kind, primarily focused on the knowledge of Earth's gravity field, the geoid, ocean tides, currents and remote sensing technology [17].

The SeaSat mission pioneered satellite oceanography increasing the precision of ocean surface mapping from 25 cm to 5 cm in 1 s averages [18], but after three months of operation the mission was cancelled due to electronic problems. Nevertheless, the quality of the dataset fully met the initial requirements, speeding up the development of the following altimetric missions. After 7 years of interregnum, the GEOSAT mission (USN:1985) with an improved version of the radar altimeter flown on SeaSat, was launched into the same orbit of its predecessor, and is considered to be the first altimeter mission to provide the research community with long-term global observations of sea level, wind speed, wave height, and ice topography.

In the early 90's, ESA started its ERS (European Remote Sensing) earth observation program with ERS-1 (ESA:1991) and the follow-on ERS-2 (ESA:1995). The twin satellites carried a suit of microwave and infrared remote sensing instruments, designed to measure wind speeds, wave heights, ocean temperature and elevation, ice elevations, scattering properties of land and ocean, and ozone concentration [19]. Placed at the same orbit of its predecessors and using ten complementary instruments, EnviSat (ESA:1999) was a multi-purpose satellite for environmental studies and continued with ESA's Earth observation program until 2012.

In the following years, new technologies were tested with CryoSat-2 (ESA:2010) and SARAL (ISRO/CNES:2012). CryoSat-2 carried an innovative radar altimeter using a delay-Doppler mode primarily focused for ice measurements, but also proved to be useful for ocean monitoring. With a different concept, SARAL was the first altimetric mission operating at a high frequency in Ka-band (≈35 GHz), in place of the traditional Ku-band (≈13.5 GHz) adopted in the previous missions, making it more compact and promising better accuracies.

After a four-year hiatus of operational and fully dedicated ESA's platforms to measure sea-surface topography, Sentinel-3A (ESA/EUMETSAT:2016) and the subsequently Sentinel-3B

(ESA/EUMETSAT:2018) currently provides a long-term commitment for altimetry measurement in the context of Copernicus Programme, the world's largest single earth observation programme, directed by EC in partnership with ESA. Sentinel-3 builds directly on the heritage pioneered by ERS-2 and EnviSat satellites, with the addition of a continuous delay-Doppler capability inherited from CryoSat-2, providing high along-track resolution with reduced noise level.

TOPEX/Poseidon (NASA/JPL/CNES:1992) was a cooperative Earth observation mission between USA and France, and was mainly designed to explore ocean circulation and its interaction with atmosphere. With an expected lifetime between 3 and 5 years, the mission delivered more than 13 years of data to study and describe global ocean dynamics and its relationship to the Earth's environment and climate change. Followed by Jason-1 (NASA/CNES:2001), Jason-2 (NASA/CNES/NOAA/EUMETSAT:2008) and Jason-3 (NASA/CNES/NOAA/EUMETSAT:2016), the four missions share the same orbit and started an oceanography mission series with the objective to monitor global ocean circulation, delivering high accuracy measurements of sea surface elevation for the last 25 years. For verification and cross-calibration reasons, Jason-1, Jason-2 and Jason-3 flew in the same orbit of their respective previous mission separated by $\sim$70 seconds over periods of about six months. These verification campaigns are called the *tandem mission phases*, when both satellites overflew the same ground-track within a minute of each other, thus observing the same ocean conditions and atmospheric properties.

The ocean topography missions can then be roughly divided into two large groups sharing the same instrumental inheritance and orbital characteristics. The first group led by ESA, includes the ERS-1, ERS-2 and EnviSat missions in a near-circular sun-synchronous orbit at an 800 km altitude, a revisit time of 35-day, covering the Earth between latitudes of $\pm 81°$ and with a track space at the equator of 80 km. A second group, constituted by the NASA/CNES missions TOPEX/Poseidon, Jason-1, Jason-2 and Jason-3, carry double-frequency altimeters, orbiting in a circular non-sun-synchronous orbit at a 1336 km altitude, with a 10-day exact repeat orbit between latitudes of $\pm 66°$ and with a track space at the Equator of 315 km. With slightly different orbital characteristics, Sentinel-3 has a sun-synchronous orbit with a mean altitude of 815 km and a ground inter-track space at the equator of 104 km, providing a revisit time of 27 days for a global coverage of topography data at mesoscale.

Table 2.1 gives an overview of the cited altimeter missions. The bullet markers identify those missions considered in the scope of the presented research, where it can be verified that primacy was given to the NASA/CNES Integrated Multi-Mission Ocean Altimeter Data for Climate Research. This choice was due to the possibility of making use of the information collected during the tandem phases, as well as to the consistency and coherency of the time-series availability in a continuous way over the last 25 years.

Table 2.1: List of satellite altimeter missions in order of their launch dates. The missions signalled with bullets correspond to those used in the present study.

Satellite	Launch	End	H (km)	Inclination	Bands	Freq. (GHz)
GEOS-3	1975	1979	856	115°	Ku	13.6
SeaSat	1978	1978	800	108°	Ku	13.6
GEOSAT	1985	1990	800	108°	Ku	13.5
ERS-1	1991	1996	784	98°	Ku	13.8
TOPEX/Poseidon •	1992	2006	1336	66°	Ku/C	13.6/5.3
ERS-2	1995	2001	784	98°	Ku	13.8
GFO	1998	2008	800	108°	Ku	13.5
EnviSat	1999	2012	784	98°	Ku/S	13.5/3.2
Jason-1 •	2001	2013	1336	66°	Ku/C	13.6/5.3
Jason-2 •	2008	-	1336	66°	Ku/C	13.6/5.3
CryoSat-2	2011	-	717	92°	Ku	13.575
HY-2A	2011	-	970	99°	Ku/C	13.6/5.3
SARAL	2013	-	781	98°	Ka	35.75
Jason-3 •	2016	-	1336	66°	Ku/C	13.6/5.3
Sentinel-3A •	2016	-	815	99°	Ku/C	13.6/5.4
Sentinel-3B	2018	-	815	99°	Ku/C	13.6/5.4

2.2 Altimeter echo characterization and processing

The satellite altimeter antenna transmits a short rectangular impulse which is reflected back from the sea surface at the moment of contact. The illuminated circular area is called the *footprint*, and its size depends on the sensor altitude above the sea, the signal propagation velocity and the pulsewidth [2].

From figure 2.2 and equation 2.5, the maximum radius of the illuminated area is proportional to the pulse duration τ, satellite height h and the speed of light during the signal travel time between the emitted and reflected signals:

$$r^2 = 2hc\tau \tag{2.5}$$

The reflected energy is dependent on the size of the reflecting area, causing this way an increase of the reflected energy at the same extent as the signal submerges the reflected surface (Fig. 2.2 (a), (b)), and at the moment as the outer edge of the pulse has arrived at the surface, the reflecting area takes an annular form with a nearly constant area (Fig. 2.2 (c)).

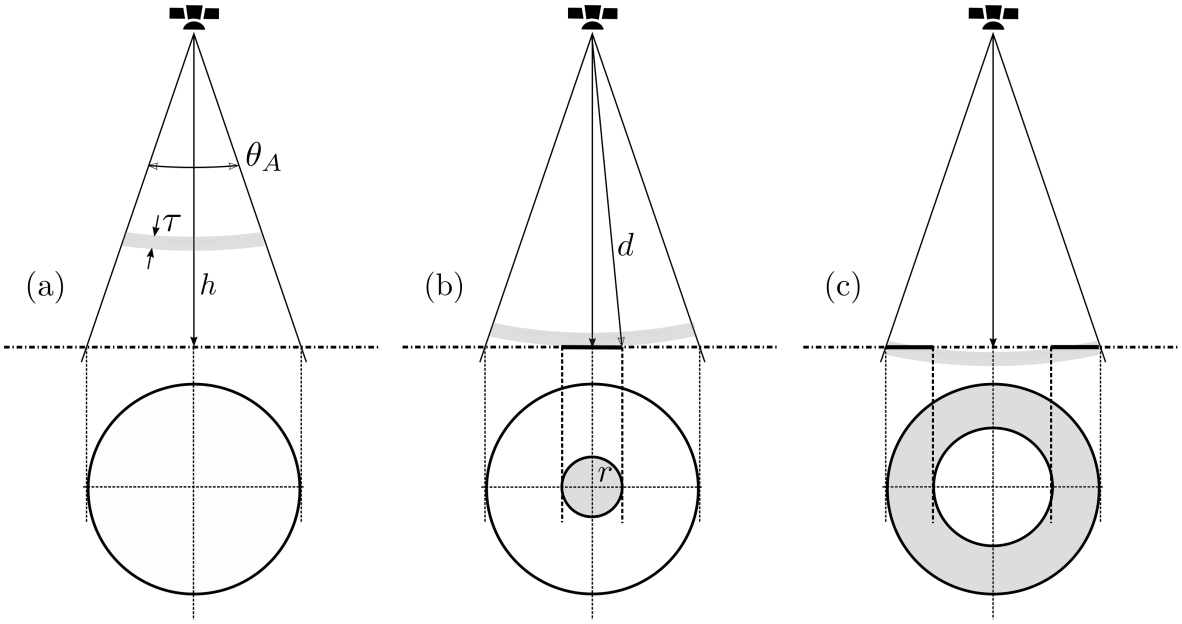

Figure 2.2: Variation of the illuminated reflecting area for a radar pulse penetrating the sea surface.

Equation 2.5 is valid for a quiet sea surface without roughness, but the final performance of the altimeter is directly dependent on the geophysical conditions of observations and the sea state when the sensor overflies the illuminated region. A detailed discussion of footprint sizes, and their dependence on geophysical parameters, can be found in [2].

The shape of the reflected signal is known as the *waveform*, where the magnitude and shape of the echoes can provide information on the nature and characteristics of the reflected surface. Over the oceans, satellite altimeters are able to retrieve information on the global distribution and variability of the sea surface height (SSH). In addition, the shape of the returned echo can be related to the significant wave height (H_s) and the amplitude of the useful signal with respect to the emission amplitude allows to derive the backscatter of the sea surface (σ^0) from which scalar wind speed (U_{10}) can be inferred [20]. Over an ocean surface, the altimeter pulse echo waveform has a characteristic shape which can be described analytically using the classical Brown model [20] allowing the estimation of the mentioned geophysical parameters (H_s and U_{10}) by fitting a theoretical model to the measured waveforms.

Figure 2.3 shows the schematics of the real (averaged) waveform retrieved from the altimeter, and the theoretical curve (also called the retracking function) providing the best fitting for geophysical parameters estimation. The extracted features of the fitted curve can be described and linked to three ocean parameters through the following form: the time (epoch) when the amplitude of the received signal represents half of the maximum amplitude in the leading edge is connected with the estimated sea surface height; from the slope of the leading edge, the significant wave height can be deduced; the backscatter coefficient of the ocean can be related to wind speed and is estimated from the maximum received amplitude. Two additional parameters

can be also considered through this approach: the trailing edge slope linked to the radar antenna deviation from nadir (mispointing), and the skewness linked to the leading edge curvature.

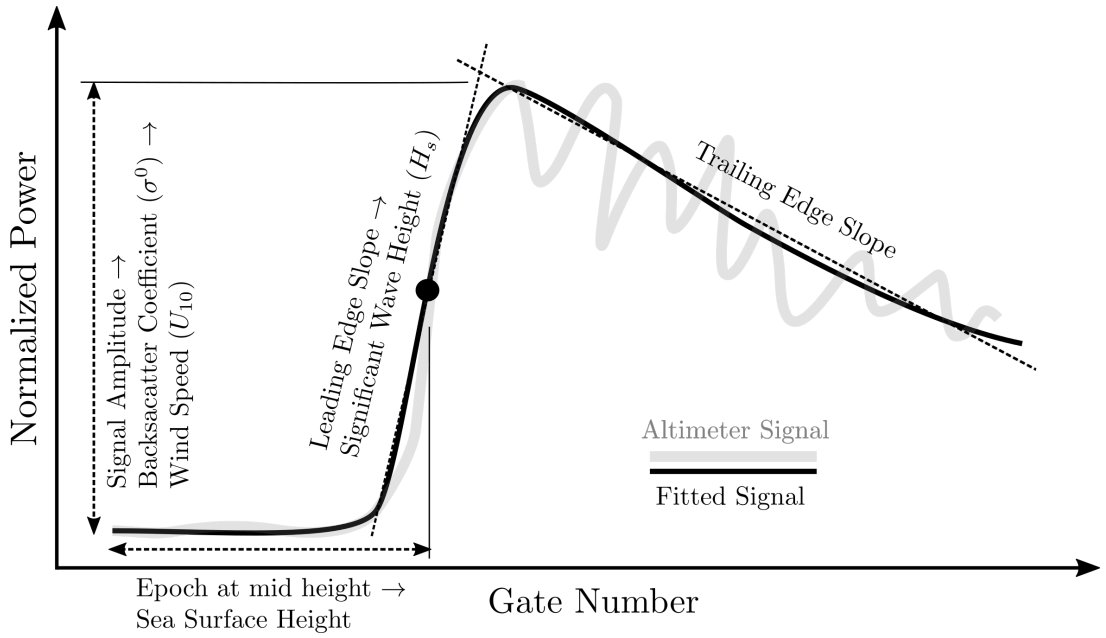

Figure 2.3: Schematic diagram of the theoretical Brown Waveform fitted to the averaged altimetric signal.

Effect of surface waves and wind on the altimeter return

As seen in the previous section, the effect of the sea state on the reflected signal is related to the footprint size and to the retrieved energy which influences the echo magnitude and shape of the waveform. When surface waves are present, three main contributions may alter the radar return: (1) the small-scale surface roughness; (2) the random nature of the sea surface; (3) the presence of large-scale ocean swell.

The first contribution is dependent on the occurring wind speed when the altimeter antenna receives the echo of the footprint. In the absence of surface wind, the water surface is undisturbed, the radar signal is specular and the maximum intensity is echoed back to the altimeter. If the wind speed increases, the increase in roughness and mean-square surface slope reflects more energy away from the antenna, decreasing this way the retrieved signal amplitude and the backscatter coefficient (σ^0) while leaving unchanged the rise time of the echo waveform [2].

If the ocean surface has no waves, the reflection from the surface is specular and the waveform leading edge is vertical, but if an increase in the ocean swell is verified, the slope of the leading edge of the waveform is reduced, inferring this way a relation with a decrease on the retrieved significant wave height (H_s). Figure 2.4 gives a graphical representation on how the two types of geophysical conditions (wind and waves) can affect the altimetric signal and the retrieved waveform. The behaviour of the returned signal in the presence or absence of ocean swell (Fig. 2.4 (a)) is characterized by the leading edge slope which allows the retrieval of the global fields

of H_s. When the altimeter senses an ocean swell region, the rise time of the backscattered signal is longer, reducing the slope of the response. However, the half-power point occurs at the same time delay (t_{RT}) as for a specular surface, i.e., when $H_s = 0$ m. On the other hand, when the altimeter retrieves information from a wind-induced roughness regions (Fig. 2.4 (b)), the signal is attenuated and the signal amplitude decreases, while leaving the rise time (t_{RT}) unchanged. Because this response to surface roughness also occurs when ocean swell is present, this wind-dependence forms the basis for a wind speed algorithm [2].

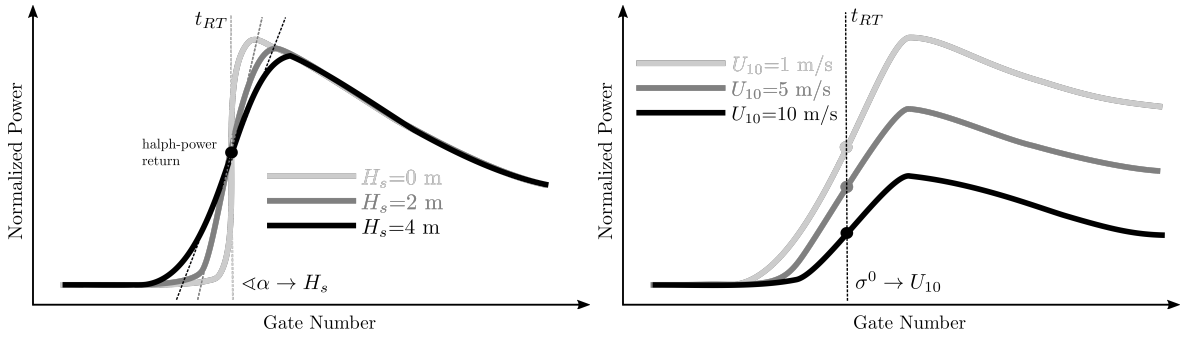

(a) Altimeter waveforms of the backscattered signal from a specular surface ($H_s = 0$ m) and from an ocean swell surface ($H_s = 2$ m and $H_s = 4$ m)

(b) Altimeter waveforms of the backscattered signal from different sea-surface roughnesses. The signal amplitude decreases as the U_{10} increases.

Figure 2.4: Theoretical waveforms of the backscattered energy and scattering cross sections for the reflection received from different ocean swell and sea-surface roughness conditions.

The presence of long-period ocean swell on the altimeter illuminated area has a direct impact on the footprint size, but due to the impossibility of the altimeter in resolving the separation between swell and wind-seas, the swell amplitude is described in terms of the significant wave height (H_s). The maximum footprint area contributing to the radar return is related with H_s by the following expression [21]:

$$A_{max} = \frac{\pi R_0 (c\tau + 2H_s)}{1 + R_0/R_e} \tag{2.6}$$

where c is the speed of light, τ is the pulse length, H_s is the significant wave height, R_0 is the altitude of the satellite, and R_e is the radius of the Earth. Equation 2.6 shows that the maximum footprint area contributing to the radar return increases linearly with H_s and is dependent on the satellite altitude. Table 2.2 shows the dependence of the effective footprint diameter on H_s [21]. For typical values of H_s between 1 and 3 m, it is observed that the effective footprint diameters are among the values of 3.6 and 5.5 km for satellites flying at an altitude of 1336 km (Topex/Poseidon, Jason-1, Jason-2 and Jason-3). However, if the radar altimeter is flying at an altitude of $\approx$ 800 km (Sentinel-3), the effective footprint diameters are reduced to values between 2.9 and 4.4 km for the same typical values of H_s. The presence of swell increases the area of the surface footprint, limiting differently the spatial resolution of the altimeter, function of the satellite altitude.

Table 2.2: Altimeter antenna effective footprint diameters function of significant wave height H_s computed from eq. 2.6 for satellite altitudes of 800 km and 1336 km.

H_s (m)	**800 km altitude (km)**	**1336 km altitude (km)**
0	1.6	2.0
1	2.9	3.6
3	4.4	5.5
5	5.6	6.9
10	7.7	9.6
15	9.4	11.7
20	10.8	13.4

2.3 Description of wind-generated waves

Wind-driven waves are generated as a result of the wind action on the water surface. Usually, this type of ocean waves can be either actively forced by the local wind field, generating *wind seas*, or they can have left their generation area, traveling long distances over the deep water, generating a *swell*. Wind seas are normally relatively steep and are often short in wavelength and height, irregular and propagate mainly with the wind direction. In contrast, swell waves are often relatively long in wavelength, of moderate height, regular and unidirectional, propagating in different directions from the generating wind.

There are many aspects which can influence the formation of flow structures in wind waves: the wind speed and its variation relative to wave speed, the wind direction, the distance of open water over which the wind blows without significant change in direction (fetch), and the water depth over the wave generation area [22]. When the wind starts to blow, three different physical processes begin: the wind turbulence produces random pressure fluctuations at the sea surface, generating small waves with wavelengths of a few centimetres [23]; the wind continues to blow over the wave, generating pressure differences along the wave profile causing the wave to grow exponentially [24]; the interaction between waves transfers energy from short waves, generated earlier, to longer waves with frequencies slightly lower than the frequency of waves at the peak of the spectrum, leading to waves travelling faster than the wind [25].

Because of the random nature of natural waves, a statistical description of the waves is normally used. The most common variables used to describe general wave characteristics are the vertical distance between a wave crest and the preceding or following wave trough (**wave height**), the horizontal distance between successive wave crests (**wavelength**), the time interval between successive wave crests or troughs (**wave period**) and the wave propagation direction.

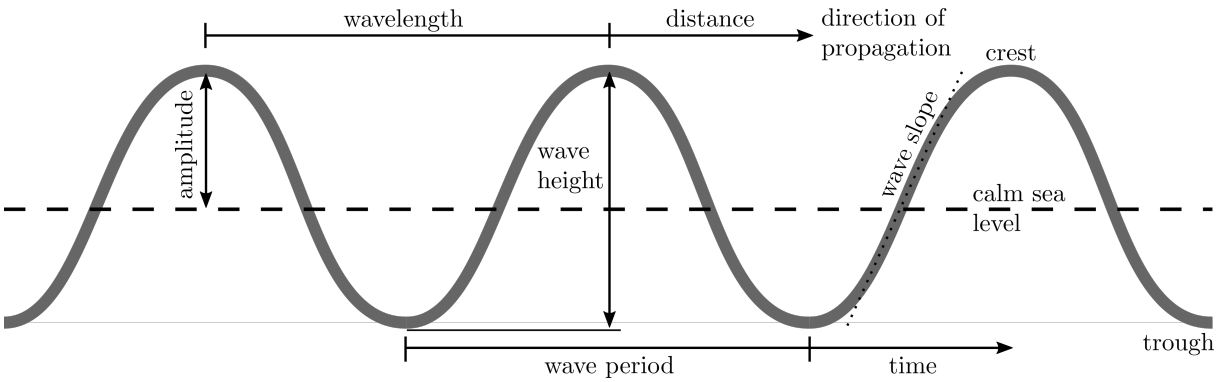

Figure 2.5: Vertical profile of three ideal ocean waves showing their linear dimensions and sinusoidal shape.

Figure 2.5 illustrates a general wave with the usually associated main characteristics. In addition to the parameters represented in the figure, others can be derived and related with those normally used: the slope between wave crest and its adjacent trough (**wave slope**); the ratio of wave height to wavelength (**wave steepness**); the number of full cycles or wavelengths per unit time (**wave frequency**); the number of full cycles per unit distance (**wave number**); the ratio of wave speed to wind speed (**wave age**).

Significant Wave Height

For many wave research applications, it is necessary to choose a single wave height characterizing a particular sea state. Usually, the random wave heights, H, follow the Rayleigh probability distribution through which several statistical wave height parameters can be derived. In physical oceanography, the most common parameter used to measure wave heights, is the significant wave height (SWH, H_s or $H_{1/3}$), corresponding to the average height of the highest one-third of all waves occurring in a particular time period, and it is defined as the *mean of the highest one-third waves* in the wave record [26]:

$$H_{1/3} = \frac{1}{N/3} \sum_{j=1}^{N/3} H_j \tag{2.7}$$

where H is the wave height, N is the number of waves in a wave record, and j is the rank number of the wave, based on the wave height. This unconventional way of defining a wave height emerges from experiments that have shown a close connection between this measure and the visually wave height estimated by an experienced observer [27]. Nowadays, the significant wave height is defined from the variance density spectrum $E(f)$, and it can be determined as an expected value with the zeroth-order moment ($m0$), the area under the spectral curve, of the highest third of the Rayleigh probability distribution of the wave field [26] in the form of:

$$H_{m0} \approx 4\sqrt{m0} \tag{2.8}$$

It is important to highlight that exists a difference in magnitude between the two significant wave height definitions, where H_{m0} is typically 5% - 10% larger than the value of $H_{1/3}$ estimated directly from measured time series. Figure 2.6 shows a typical wave spectrum with the statistical concept used to estimate several parameters of the waves in a specific forecast. The greatest number of waves is indicated by the widest area (light grey) of the spectrum curve, and the highest $1/3^{rd}$ of waves is highlighted in dark grey. The average height of waves in this group has the statistical meaning of the significant wave height (H_s).

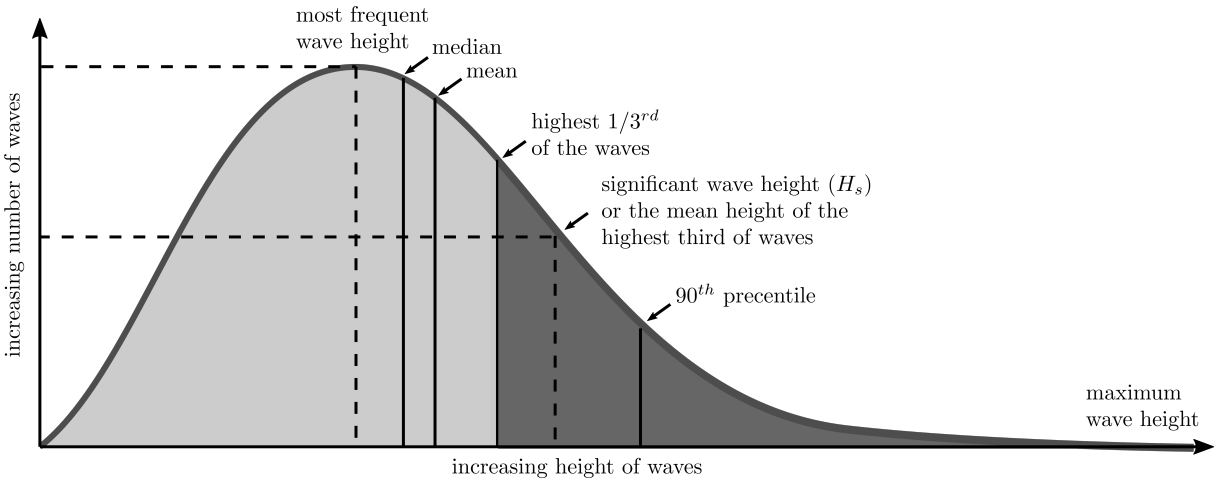

Figure 2.6: Theoretical Rayleigh probability distribution of the wave heights showing the different statistical parameters that can be inferred. (Adapted figure from [28])

Typically, the mean value of H_s is between 2 and 4 m, depending on the region of the globe. Regional seas usually present lower values of H_s due to their limited areas and depth for wave propagation, in contrast with the deeper and larger open ocean areas, which present higher values of H_s. The global distribution of significant wave height displays a zonal structure, with a large band of high waves in the Southern Oceans that reaches its maximum around 50°S. Figure 2.7 shows the spatial distribution of H_s for the 4 seasons of 2017, computed from the ERA-Interim global atmospheric reanalysis model provided by the European Centre for Medium-Range Weather Forecasts (ECMWF).

From the same figure, it is possible to observe that in the Northern Hemisphere, during winter and autumn, the highest waves are located in the mid-latitudes, both in the central North Atlantic and North Pacific Oceans. This prevalence is dissipated during the summer, when the waves become stronger and larger in the Southern band.

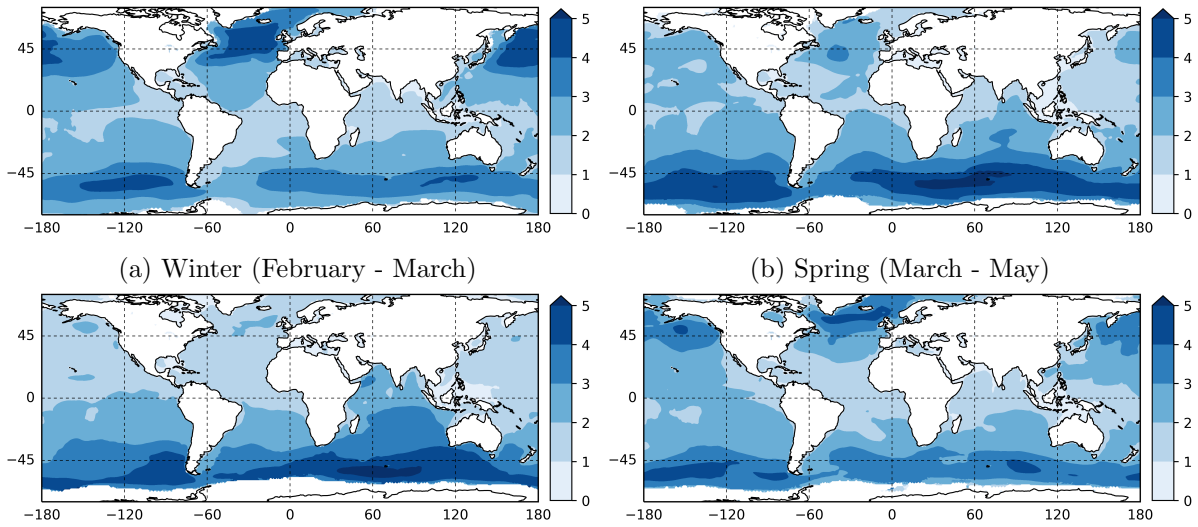

(a) Winter (February - March)

(b) Spring (March - May)

(c) Summer (June - August)

(d) Autumn (October - November)

Figure 2.7: Set of seasonal maps with the global significant wave height (m) derived from ERA-Interim for the year 2017.

Wind Speed

As described earlier, the size of a wind-generated wave depends on the wind speed, wind duration, the distance of open water over which the wind blows, and the water depth where the gusts take place. If the wind duration and wind fetch are long enough, the sea becomes fully developed and reaches a steady state, causing the waves to reach a maximum size for that wind speed. For oceanographic and meteorological purposes, it is common practice to work with the components of the wind. From the magnitude of wind vector ($\|\overrightarrow{V}\|$) and wind direction (θ), it is possible to obtain the component vector wind speeds, U and V, as follows:

$$U = \|\overrightarrow{V}\| \cos(\theta) \quad \text{and} \quad V = \|\overrightarrow{V}\| \sin(\theta) \tag{2.9}$$

The relationship between wind speed and significant wave height can be expressed by the Beaufort wind force scale (table 2.3), which empirically relates the observed conditions at sea with wind speed. The scale is valid only for waves generated within the local weather system, and assumes sufficient time to establish a fully developed sea.

Table 2.3: Modern Beaufort wind force scale relating wind speed to significant wave height.

Number	**Description**	**Wind speed (m/s)**	**H_s (m)**	**Sea-state**
0	Calm	< 0.3	0	Flat
1	Light air	0.3 - 1.5	0.1	Ripples
2	Light breeze	1.5 - 3.3	0.2	Small wavelets
3	Gentle breeze	3.3 - 5.5	0.6	Large wavelets

Number	Description	Wind speed (m/s)	H_s (m)	Sea-state
4	Moderate breeze	5.5 - 8.0	1.0	Small waves
5	Fresh breeze	8.0 - 10.8	2.0	Moderate waves
6	Strong breeze	10.8 - 13.9	3.0	Large waves
7	Moderate gale	13.9 - 17.2	4.0	Sea heaps up
8	Fresh Gale	17.2 - 20.7	5.5	Moderate high waves
9	Strong gale	20.7 - 24.5	7.0	High waves
10	Storm	24.5 - 28.4	9.0	Very high waves
11	Violent storm	28.4 - 32.6	11.5	Massive high waves
12	Hurricane	> 32.6	> 14.0	Huge waves

Figure 2.8 illustrates the seasonal fluctuations of wind speed around the globe for 2017. The data are linked to the U component 10 meters above ground and are also derived from ERA-Interim global atmospheric reanalysis model. From the same figure, is it possible to observe that the largest wind resources are above the oceans, with predominance in the South Pacific regions. As seen for significant wave height, there is a decrease in the Northern Hemisphere during the spring and winter seasons. A bigger prevalence of strong wind gusts in Southern Asia is also noted for these seasons, thus leading to an increase of the significant wave height for the same periods, as it can be seen in figure 2.7. The observation of these two figures, clearly shows the connection between wind formation regions and wave heights, leading to a better understanding of the wind waves origin.

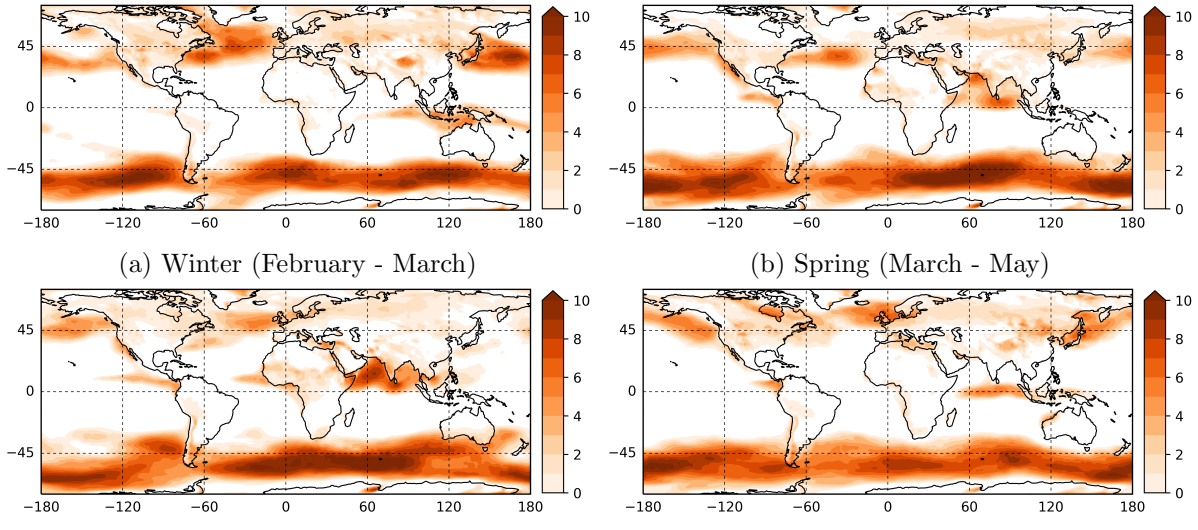

(a) Winter (February - March)

(b) Spring (March - May)

(c) Summer (June - August)

(d) Autumn (October - November)

Figure 2.8: Set of seasonal maps with the global wind speed (m/s) derived from ERA-Interim for the year 2017.

Wave Period

As shown in figure 2.5, the wave period is one of the key parameters used for sea-state characterization. Sea waves follow a harmonic behaviour alternating between crests and troughs during their time of propagation. Together with the wave height, the wave period play an important role for swell identification, since for a given wave height, the larger the period, the more energetic and powerful will be the swell. In analogy with the significant wave height, the *significant wave period* T_s is defined as the mean period of the highest one-third of waves in the form of [26]:

$$T_{1/3} = \frac{1}{N/3} \sum_{j=1}^{N/3} T_{0,j} \tag{2.10}$$

where j is the rank number of the wave based on wave height, and T_0 is the zero-crossing wave period defined as the mean time interval between upward or downward zero crossings on a wave record. But in contrast with $\mathrm{H}_{1/3}$, which has a direct relation with visual observations, $\mathrm{T}_{1/3}$ derived from instrumental measurements, does not agree with the visual estimated significant wave period ($\mathrm{T_v}$).

There are several approaches for describing the mean wave period of random waves based on the n^{th} spectral moments m_n: 1) $T_{01} = m_0/m_1$ defined as the reciprocal number of the mean frequency of energy spectrum; 2) $T_{02} = \sqrt{m_0/m_2}$ as the mean zero-crossing time interval; 3) $T_{24} = \sqrt{m_2/m_4}$ as the mean time interval for the local maxima [29]. Since the values of higher-order moments are rather sensitive to noise in the high-frequency range of the spectrum because, T_{02} and T_{24} are not always the most reliable estimators for mean wave period, whereby T_{01} is usually used due to the less dependency on high-frequency noise. Another common way to identify the representative period of a sea state, is through the *peak wave period* T_p, which corresponds to the period of the most energetic wave component, whereas $T_{01} = T_m$ is related to the mean of all wave periods in a time-series representing a certain sea state. Based on observations and computer simulations, empirical relationships have been performed by [30] in order to link the significant wave period $T_{1/3}$ with T_p for swell and wind sea waves:

$$T_{1/3} \approx T_p \text{ for swell}, \quad \text{and} \quad T_{1/3} \approx 0.95 T_p \text{ for wind sea} \tag{2.11}$$

Figure 2.9 illustrates the global variation of mean wave period $\mathrm{T_m}$ for each season in 2017. Comparing with the previous parameters shown above, it is possible to observe a predominance of high $\mathrm{T_m}$ in open-ocean regions, shifting across seasons. As mentioned earlier, the swell formation is characterized by medium-high wave periods and heights, leading to a fully developed sea. Figure 2.9 shows that during the winter, there is a swell predominance in the Pacific and North-Atlantic oceans, decreasing in the Northern Hemisphere between spring and summer.

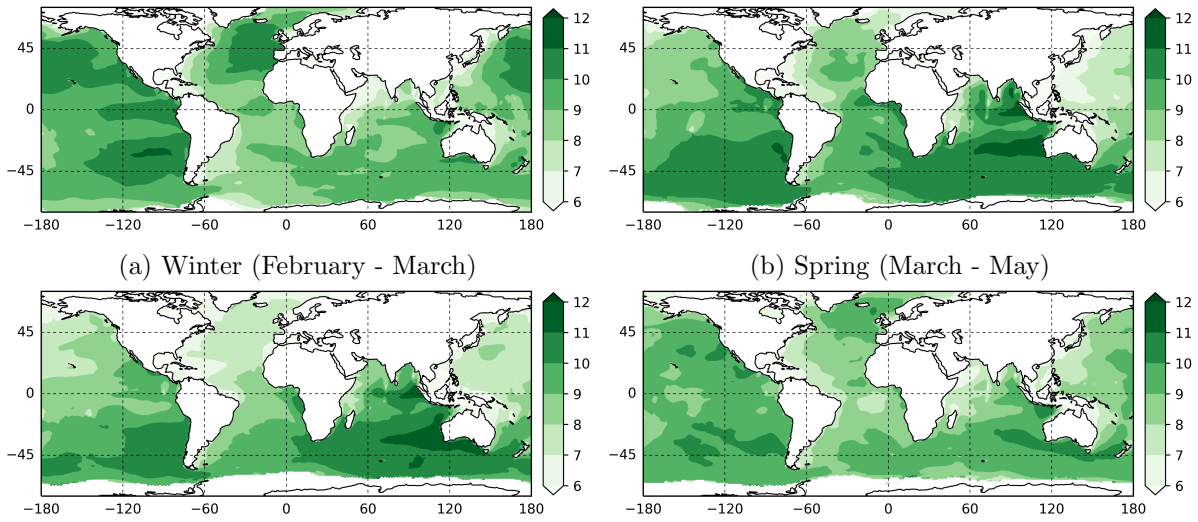

(a) Winter (February - March)

(b) Spring (March - May)

(c) Summer (June - August)

(d) Autumn (October - November)

Figure 2.9: Set of seasonal maps with the global mean wave period (s) derived from ERA-Interim for the year 2017.

Wave Propagation Direction

As in the previous case of wave period, the wave direction is also characterized by its mean, leading to the mean wave direction (θ_m). This parameter represents the mean of all the individual wave directions in a time-series representing a certain sea state. When modelling ocean waves, the directional distribution $D_f(\theta)$ describing the energy of waves at a particular frequency f and angle θ, can be expressed as the following Fourier series:

$$D_f(\theta) = \frac{1}{2\pi}\left[1 + 2\sum_{n=1}^{\infty}\left\{a_n\cos(n\theta) + b_n\sin(n\theta)\right\}\right] \tag{2.12}$$

where $a_n = \int_0^{2\pi} D_f(\theta)\cos(\theta)d\theta$ and $b_n = \int_0^{2\pi} D_f(\theta)\sin(\theta)d\theta$. According to [31], the mean wave direction, θ_0 is given by:

$$\theta_0 = \arctan\left(\frac{b_1}{a_1}\right) \tag{2.13}$$

where b_1 and a_1 are the first order Fourier coefficients, and the wave propagation direction angle, θ_0, uses the meteorological convention, i.e, 0° from North, 90° from East, 180° from South, and 270° from West. Figure 2.10 illustrates the global distribution for mean wave direction during 2017. In the Southern Hemisphere, the dominant winds usually travel from West to East, however, the opposite is verified in the Tropical and Subtropical regions, where the dominant winds generally travel from East during most of the year.

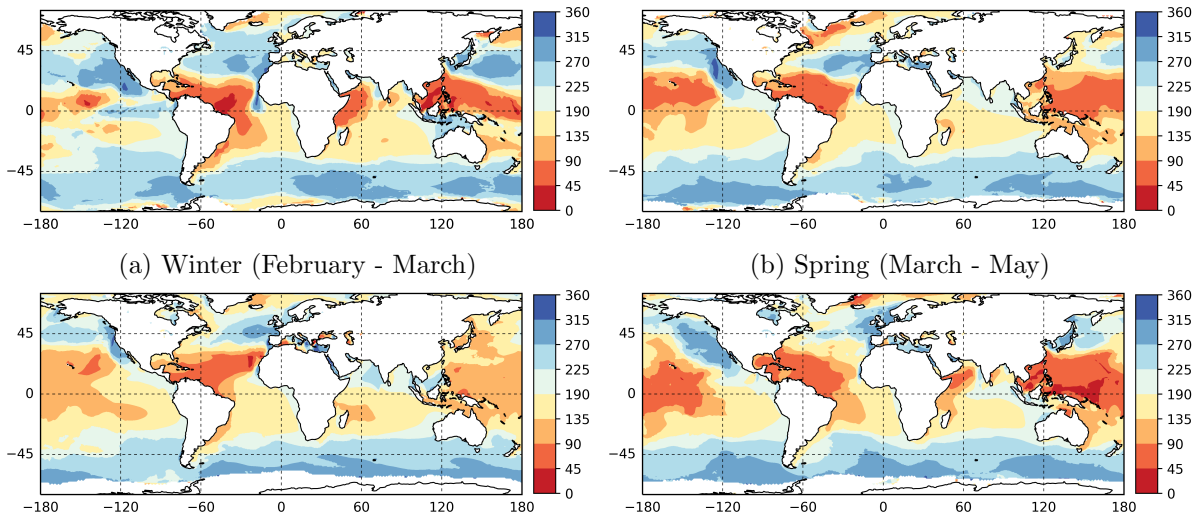

(a) Winter (February - March)

(b) Spring (March - May)

(c) Summer (June - August)

(d) Autumn (October - November)

Figure 2.10: Set of seasonal maps with the global mean wave direction (degrees) derived from ERA-Interim for the year 2017.

2.4 Directional Wave Spectrum

The sea surface in the presence of wind-generated waves can be visualized as an irregular collection of crests and troughs. This water surface irregularity can be decomposed into an infinite number of simple sinusoidal components with different *frequencies* (f) and propagation *directions* (θ). To describe this irregularity and unpredictability, the concept of wave spectrum is usually introduced to characterize the complex and chaotic phenomenon of wind-generated ocean waves in terms of contributions from waves propagating in different directions with different wavelengths (or frequencies). This concept is generally expressed by:

$$E(f,\theta) = E(f)D(f,\theta) \tag{2.14}$$

where the function $E(f)$ is the *variance density spectrum* in its continuous form, and $D(f,\theta)$ is the *directional spreading function* [26] in the form of:

$$E(f) = \lim_{\Delta f \to 0} \frac{1}{\Delta f} E\left\{\frac{1}{2}\underline{a}^2\right\} \tag{2.15}$$

$$D(f,\theta) = \frac{1}{\sigma(f)\sqrt{2\pi}} e^{\frac{(\theta-\theta_0(f))^2}{2\sigma(f)^2}} \tag{2.16}$$

If we assume the surface elevation as a stationary Gaussian process, in a statistical sense, equation 2.15 gives a complete description of this surface elevation caused by ocean waves. The *variance* $E\left\{\frac{1}{2}\underline{a}^2\right\}$ is based on discrete frequencies and needs to be distributed continuously over all range of frequencies when approaching to zero ($\lim_{\Delta f \to 0}$).

Since the variance density spectrum $E(f)$ is one-dimensional, the directional distribution $D(f, \theta)$ (Eq. 2.16) takes the directional spread of waves at frequency f as the standard deviation of the wave directions $\sigma(f)$ and the mean wave direction $(\theta_0(f))$, and gives the normalized distribution of the wave energy density over all directions at one given frequency. Usually, the directional wave spectrum is represented in polar coordinates with an horizontal plane defined by (f, θ). Figure 2.11 shows a theoretical continuous two-dimensional variance density spectrum over all frequencies and directions. However, as seen in the previous sections, ocean surface waves can be generated by *wind seas* immediately related to the local wind field, or by the *swell* related to the waves propagating beyond the zones of their generation. Figure 2.12 illustrates the theoretical directional spectrum when the two wave systems are retrieved over the same region.

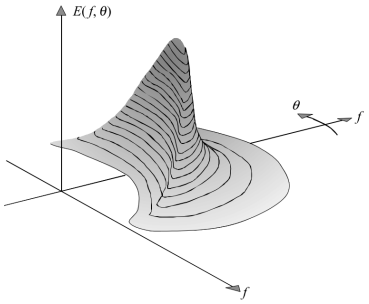

Figure 2.11: Theoretical distribution of wave energy across two-dimensional space (directional spectrum of wind-generated waves). Figure reprinted from [26].

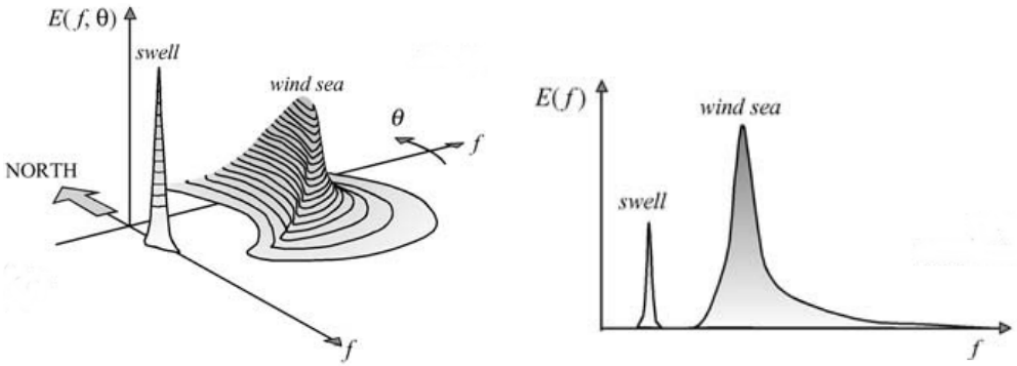

(a) Two-dimensional spectrum

(b) One-dimensional spectrum

Figure 2.12: Theoretical wave spectrum representing two wave systems (swell and wind sea). Figure reprinted from [26].

From figure 2.12 it is possible to observe two spectral signatures, one well defined peak in direction and frequency corresponding to the swell wave system, and a second signature with a broad distribution of the waves around a peak linked to wind sea. Swell is generally of a much lower frequency than a young wind sea, causing in this case two well separated wave systems, both in frequency and direction. Due to its regularity and a long-crested behaviour, the energy of swell propagation is concentrated in a narrow band around the mean wave direction, thus resulting in a narrow spectral signature. In the case of a young wind sea, the spectrum is in general much broader due to its irregular and short-crested characterization, thus generating a signature with higher frequencies in the spectral domain. Usually, swell waves are not steep and therefore do not directly interact very much with each other or with the growing wind sea, thus causing a rather distinctive signatures as shown in figure 2.12. The one-dimensional spectrum

(fig. 2.12b) is obtained by integrating the two-dimensional spectrum over all directions, and in the given example, one can observe the presence of two well-defined peaks, thus separating the two observed wave systems.

The summary wave statistics usually retrieved by parameters such as wave height, wave period and wave direction, are a simple approximation and often insufficient means of characterizing complex wave fields. Parameters such as significant wave height, mean wave period and mean wave direction are only partial descriptors of the full wave energy spectrum and neglect significant spatio-temporal information. In order to study the wave conditions with all wave systems propagating in different directions, integral parameters are computed from the directional wave spectra $E(f, \theta)$ differentiating the wave components in the spectrum as wind sea and swell. Figure 2.13 shows three spectral examples, in a real situation, of wave systems depending on their generation conditions. Using a partition technique, the integration of sea-state parameters is performed over all frequencies and directions or over a spectral sub-domain when the spectrum is split between wind sea and swell, thus making possible to derive different heights, periods and directions related to each wave system contributing to the wave spectrum.

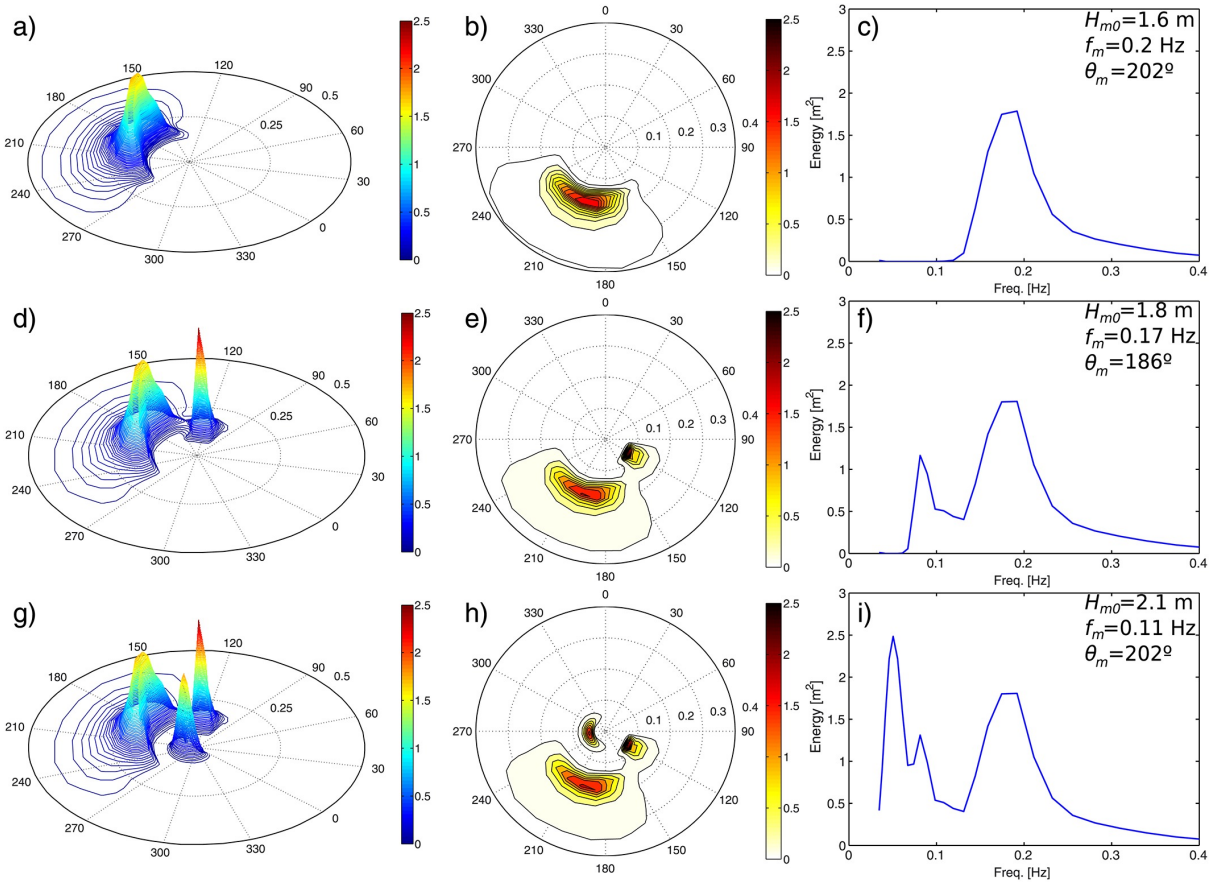

Figure 2.13: Example of one-dimensional and two-dimensional directional spectra of three wave conditions illustrating their different signatures and integrated parameters of wave height, period and direction. Figure reprinted from [32].

Nowadays, directional wave measurements can be retrieved from different sources using a large array of retrieval and analysis techniques applied to in-situ instrumentation, numerical models and simulators, and remote sensing platforms. The classical methods based on spatial arrays and pitch-and-roll buoys, are now complemented by Global Navigation Satellite System (GNSS) buoys, acoustic Doppler current meters or marine radars, and are a valuable source of wave information for calibration and validation of the other techniques. Global coverage retrieval of directional wave information is also possible from synthetic aperture radar (SAR) sensors coupled on aerial platforms, which based on mathematical inversion methods applied to the acquired imagery of the sea surface, can provide directional information on ocean waves. The numerical wave models do not provide direct observations of the sea-state, but after assimilating and combining data from several instrumental and remote sensing sources, can provide a description of the wave spectra, with amplitudes associated to each frequency and propagation direction.

Sentinel-1 Ocean Swell Wave Spectra

Synthetic aperture radar (SAR) provides high resolution two dimensional images of the radar backscatter properties of the sea surface and can thus be used to measure wind fields and estimate the two-dimensional wave spectrum from space. The determination of ocean wave spectra from SAR image spectra is sensitive to various imaging effects due to sea surface features, spatial variation of wind speed, rain, current and motion of the sea surface. Much effort has been devoted for marine applications from SAR over past decades, the methodologies of wave spectra retrieval from SAR needs a good understanding of complicated SAR wave imaging mechanisms and their connection with sea-state. Two different approaches are usually used to estimate wave spectra from SAR, a first one based on full nonlinear inversion techniques which requires external information from numerical wave models to estimate a full wave spectrum using a first guess [33], [34], and a second one based on the quasi-linear inversion method which produces a wave spectrum that cannot fully resolve high-frequency waves [35], [36]. In order to reduce the speckle noise level of SAR images while preserving the spectral shape, [37] proposed the use of image cross spectrum containing the real and imaginary part information on the propagation direction of wind-generated ocean waves.

Following the legacy left by ESA C-band SAR instruments of ERS-1, ERS-2 and EnviSat, Sentinel-1 also carries a single C-band synthetic aperture radar instrument operating in dual polarization (HH+HV, VV+VH). Four acquisition modes are provided: the Stripmap imaging mode (SM) covering in a narrow swath width of 80 km with a 5 x 5 m resolution; the Interferometric Wide Swath mode (IW) combining a large swath width of 250 km with a moderate geometric resolution of 5 x 20 m; the Extra Wide Swath mode (EW) working similarly to the IW mode, but with shorter revisit times and larger coverage with a lower resolution of 20 x 40 m; and a Wave mode (WV) with acquisition images every 100 km along the orbit, composed of stripmap *imagettes* with an approximate satellite footprint of 20 x 20 km. Sentinel-1 alternates

between two incidence angles of 23° (WV1) and 36° (WV2) along its track, whereby imagettes with the same incidence angle are separated by 200 km [38].

Sentinel-1 mission provides several core products based on each level of processing: the SAR Level-0 product with compressed unfocused SAR raw data, Level-1 Single Look Complex (SLC) product with focused SAR georeferenced data in slant-range geometry and preserving the phase information, Level-1 Ground Range Detected (GRD) product with focused SAR data multi-looked and projected to ground range using the Earth ellipsoid model WGS84 without preserving the phase information, and Level-2 Ocean (OCN) product designed to deliver geophysical parameters related to Ocean Swell spectra (OSW), Ocean Wind Fields (OWI) and Surface Radial Velocities (RVL). The OSW component of the OCN product is a two-dimensional ocean surface swell spectrum estimated from a SLC image by inversion of the corresponding image cross-spectra. For Wave mode, one spectrum per imagette is retrieved for ocean areas with the same spatial coverage of Level-1 WV-SLC, i.e, 20 x 20 km. The spectral resolution depends on the sea-state of the illuminated area and direction of wave propagation relative to the satellite azimuth, and is provided on a log-polar grid for the wavenumber and wave direction in units of m^4. The product provides a number of sea-state integrated parameters derived from OCW ocean wave spectra, image statistics retrieved directly from the imagette, including also an estimate of the wind sea significant wave height and other sensor parameters. Table 2.4 lists all the parameters available in the Sentinel-1 OCN OSW product:

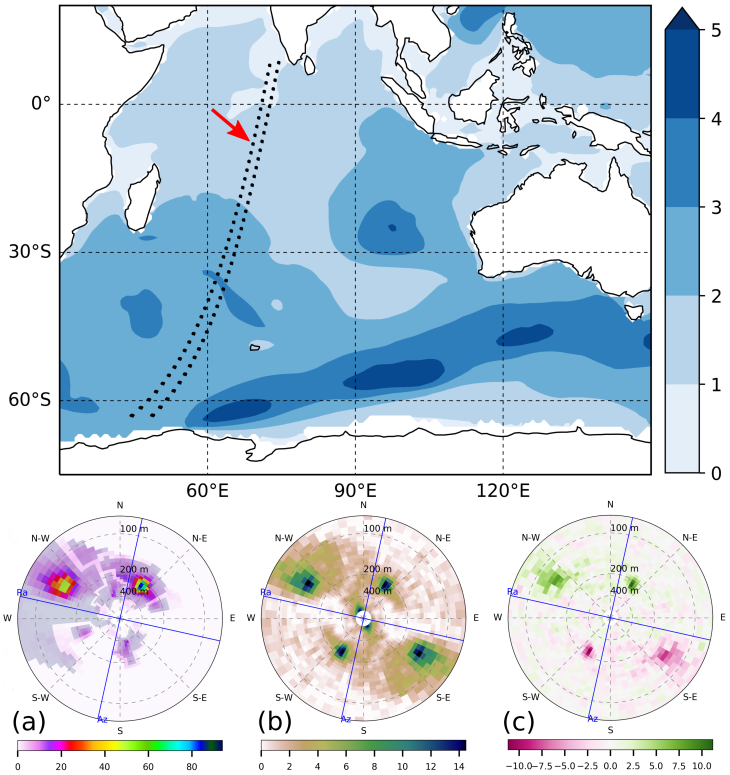

Figure 2.14: Sentinel-1A WM acquisition segment over the Indian Ocean. Top plot shows the 84 imagettes indicated as dots and the background color stands for significant wave height as predicted by ECMWF ERA-Interim. Bottom plots are the (a) estimated swell spectrum, (b) and (c) real and imaginary part of cross spectrum retrieved from imagette 20 signalled with a red arrow.

Table 2.4: Integrated parameters derived from 2-dimensional wave spectrum and image statistics available in the Sentinel-1 Level-2 OCN OSW product.

• Imagette ID num	• Platform heading	• Wavelength (per partition)
• Centroid latitude	• Backscatter	• Wave direction (per partition)
• Centroid longitude	• Wind sea H_s	• Image intensity
• Polarization	• Inverse wave age	• Image skewness
• Wind speed	• Azimuth cut-off wavelength	• Wind speed (ECMWF)
• Wind direction	• Range cut-off wavelength	• % of land coverage
• Incidence angle	• H_s (per partition)	• Water depth

Figure 2.14 shows an example with Sentinel-1A acquisition segment in Wave mode over the Indian Ocean between 00h:57m:31s and 01h:17m:50s on February 1, 2017. The upper plot shows the imagettes footprint captured by the SAR instrument during ≈20 minutes of its descending pass. 84 imagettes were retrieved, 42 for each incidence angle. Signalled with a red arrow is imagette #20, with the estimated swell spectrum and cross spectra represented at the bottom. Crossing the data retrieved by this imagette with the ERA-Interim H_s model available for the same day at 00h:00m:00s, it is possible to observe that the total height of the significant wave (swell height + wind sea height) given by the model is between 1 and 2 m. In this case the estimated H_s by OSW product of imagette #20 is 0.93 m, and from the two-dimensional swell wave spectrum, one can observe two different wave systems composed by two swell partitions, a less pronounced swell system with a broader distribution at $\approx 300°$, wavelength and wave height of 126 m and 0.71 m respectively, and a most energetic swell partition, with a narrower distribution at $\approx 30°$, wavelength of 220 m, and a wave height with 0.47 m. The product also delivers information about wind speed and direction, and for the example shown, at the time the satellite overflew the region, there was a light breeze of 5 m/s coming from East.

In the scope of this thesis, the Sentinel-1 Level-2 OCN OSW product has been used to collect more sea-state information in order to find correlations and interconnections with altimeter data. This study helped in the sense of a better Sea State bias (SSB) characterization, finding its dependencies on swell height, direction and length, and is presented with detail in **article 3** on chapter 5.

2.5 The Sea State Bias origin and description

In section 2.2 is described the effect of surface waves and wind on the altimeter return, and how the different sea-state contributions may alter the radar return. At the error produced in altimetric range measurement due to the presence of waves on the ocean surface, is called sea state bias (SSB), and for conventional pulse-limited altimetry, is usually characterized by the sum of three different contributions, generating a wave-height-dependent range bias in the retrieval of sea surface height (SSH) [2]:

- Electromagnetic bias: is an effect linked to the backscatter in a nadir-viewing geometry, where the portions of the illuminated surface backscattered to the satellite reflects differently from wave troughs and crests. This happens because the curvature radius of wave troughs are larger than wave crests' curvature, thus resulting in a stronger radar backscattered power per unit area, overestimating the measured satellite-to-surface range and causing the erroneous idea that the mean reflecting surface is depressed below mean sea level [3], [39]. The parasitic capillaries formed on wave crests are an additional factor since they scatter energy away from the altimeter and increase this depressed mean reflecting surface.

- Skewness bias: refers to the additional apparent depression, linked to the effect of a non-Gaussian surface distribution. The fact that real ocean waves have flatter troughs and peakier crests than sinusoidal waves, changes the statistical distribution of surface elevation from a Gaussian to a non-Gaussian distribution [40]. This skewed nature of ocean surface waves induces differences between the median sea surface height received by the altimeter echo and the mean height of the sea level of interest.

- Tracker bias: can occur due to instrumental or algorithmic effects derived from the retracking choices made to retreive the geophysical information from the altimeter waveforms. When an imprecise tracker determination is wrongly adapted to the midpoint location of the altimeter return or waveform leading edge, sea-state estimations of SWH and SSH are affected and needs to be addressed [21].

While the electromagnetic and skewness biases are directly linked with the physical characteristics of the sea-state at a given moment, these two components of sea state bias affect all satellite altimeters in the same way, but because the instrumental part of SSB given by tracker bias is unique to each instrument, every altimeter requires a different SSB correction model, and needs to be evaluated separately for each mission.

In a first order approximation, SSB is generally expressed in the following form:

$$SSB = -\epsilon H_s \tag{2.17}$$

with the minus sign indicating that SSB lowers the estimate of the SSH and is linearly proportional to significant wave height H_s. This proportionality represented by ϵ may vary according with several sea-state parameters found at the illuminated footprint when the altimeter overflies a particular region of the ocean. These additional parameters could be any that helps to better describe the sea-state conditions, such as the related wind speed, the backscatter coefficient, a proportion of wave slope or wave period, or others sea-state correlators derived from wave spectrum. With an order of magnitude ranging between 3%-4% of H_s , the SSB is a centimeter-scale measurement bias and remains one of the largest sources of uncertainty linked with the altimetric signal.

Several theoretical studies of SSB have been conducted in the past to model the sum of the electromagnetic bias and skewness bias [40]–[42]. These models are based on the work of [43] for their statistical description of the nonlinear sea surface waves, and relies on computation of the nonlinear moments of the sea surface using a two-dimensional spectrum. Later, [44], [45] proposed a new theory, extending these studies to account for further nonlinear effects with short/long wave interactions. This complex theoretical approach gives a reasonable representation of the measured SSB, considering both long wave nonlinearities and long-short wave interactions for SSB correction, but any of the proposed algorithm have been validated in terms of correction accuracy. [46] did an in-depth study of the two main theoretical approaches proposed by [47] and [45] raising several problems concerning the frequency dependence of SSB and the poorly representation of strong nonlinear effects such as wave breaking. Additionally to this, it has to be taken into account that all theoretical studies of SSB are focused only in the two components directly related with the interaction between the sea-state and altimetric signal, leaving out the tracker bias, which in some cases, may be the dominant cause of SSB. Because of these reasons, SSB estimations still largely relies on empirical approaches.

Empirical models developed from parametric and non-parametric techniques, are usually the most common approach to estimate sea state bias for satellite altimeter missions. In the early days of altimetry, the SSB was generally considered as a simple linear empirical model using a first-order predictor expressed by eq. 2.17 due to the strong dependency of SSB with H_s and was usually considered as a simple fraction of around -3.5% of H_s [11], [48]. After that, SSB estimates started to be computed through fitted empirical models derived from the significant wave height and wind speed information retrieved from altimeter data, evolving into different parametric formulations in linear, polynomial or quadratic forms with a number of coefficients to be estimated [10]. The most recent approaches for SSB modeling, tend to be non-parametric formulations using different statistical techniques and predictors, based on kernel smoothing methods [12], local linear kernel smoothing [13] or smoothing splines [15], [49], [50].

The usual approach when implementing an empirical model for SSB, is to minimize SSH differences against the geophysical parameters retrieved by the altimeter, i.e., significant wave height and wind speed. One of the main difficulties of using this approach, is to estimate a sea-state-related correction from SSH differences, without absorbing oceanic variability and residual errors, leading to incorporate the maximum sea-state information to feed the statistical model. The fact that the altimeter is only capable of measuring directly the H_s and U10, and the recognition that these two parameters alone can not entirely parametrize the SSH variability associated to nonlinear interactions of ocean wind-generated waves propagating in multiple directions, a number of studies tried to design new SSB model approaches with additional sea-state parameters in order to explain more of of the remaining SSH variability. These were either obtained indirectly from altimeter-derived parameters such as Ku-band σ_0 or pseudo wave age [3], [6], [51] or by combining altimeter data with external predictions such as swell height, mean wave period or inverse wave age retrieved from numerical wave models [7], [8].

In the scope this thesis, has been made an in-depth study concerning the development of an SSB model designed with three parameters exclusively derived from altimeter data, where additionally to H_s and U10, has been implemented a third predictor acting as a mediator parameter gathered by the Mean Wave Period (T_z). As a preliminary stage, the proposed technique was tested and evaluated for Jason-1 mission, and proved to have a good performance for a wide range of ocean conditions when compared with the state-of-the-art SSB corrections currently available. This work is presented in detail by **article 1** in chapter 3. In a subsequent phase, a thorough study was made in order to improve the designed model. The development has evolved with new methods and assessment techniques, and it was globally applied to the four altimeter reference missions (TOPEX, Jason-1, Jason-2 and Jason-3). This work is presented in detail by **article 2** in chapter 4.

THIS PAGE IS INTENTIONALLY LEFT BLANK.

Chapter 3

Article 1: A Conceptually Simple Modelling Approach for Jason-1 Sea State Bias based on 3 Parameters Exclusively Derived from Altimetric Information

Nelson Pires [1], M. Joana Fernandes [1], Christine Gommenginger [2] and Remko Scharroo [3]

[1] Department of Geosciences, Environment and Spatial Planning, Faculty of Sciences, University of Porto, Porto 4169-007, Portugal
[2] National Oceanography Centre, Natural Environment Research Council, Southampton SO14 3ZH, UK
[3] European Organisation for the Exploitation of Meteorological Satellites, Darmstadt D-64295, Germany

Academic Editors: Raphael M. Kudela, Xiaofeng Li and Prasad Thenkabail

Received: 29 April 2016 / Accepted: 4 July 2016 / Published: 8 July 2016

Academic Journal: **Remote Sensing**

Remote Sens. **2016**, 8(7), 576; doi:**10.3390/rs8070576**

3.1 Abstract

A conceptually simple formulation is proposed for a new empirical sea state bias (SSB) model using information retrieved entirely from altimetric data. Nonparametric regression techniques are used, based on penalized smoothing splines adjusted to each predictor and then combined by a Generalized Additive Model. In addition to the significant wave height (SWH) and wind speed (U10), a mediator parameter designed by the mean wave period derived from radar altimetry, has proven to improve the model performance in explaining some of the SSB variability, especially in swell ocean regions with medium-high SWH and low U10. A collinear analysis of scaled sea level anomalies (SLA) variance differences shows conformity between the proposed model and the established SSB models. The new formulation aims to be a fast, reliable and flexible SSB model, in line with the well-settled SSB corrections, depending exclusively on altimetric information. The suggested method is computationally efficient and capable of generating a stable model with a small training dataset, a useful feature for forthcoming missions.

Keywords: satellite altimetry; sea state bias; mean wave period; nonparametric estimation; GAM

3.2 Introduction

Sea state bias (SSB) is an altimeter ranging error caused by the influence of sea-state effects in the radar altimeter measurements, since the surface scattering elements do not contribute equally to the radar return. Usually, the SSB is characterized by the sum of three different contributions. An electromagnetic bias (EM) evidenced by the signal-surface interactions, where ocean wave troughs are better radar reflectors than wave crests, thus overestimating the measured satellite-to-surface range. The EM bias perturbs all microwave frequencies with wavelengths of a few centimetres, affecting not only the Ka-, C-, and Ku-bands regularly used for satellite altimetry [1, 2], but also the L-band frequency usually adopted for Global Navigation Satellite Systems Reflectometry (GNSS-R) altimetry [3]. In addition to EM bias, the SSB is also characterized by a skewness bias linked to the effect of a non-Gaussian surface height distribution, inducing an error due to the difference between the determined median sea surface and the true mean sea surface (MSS), and finally, a tracker bias which can occur due to both instrumental and retracking effects. With an order of magnitude ranging between 3% – 4% of the significant wave height (SWH), this centimetre-scale measurement bias remains as one of the largest sources of uncertainty linked with the altimetric signal.

Historically, the parametric SSB models started to be developed as a simple linear empirical model using a first-order predictor expressed in the normalized form as $\alpha = \mathrm{SSB}/\mathrm{SWH}$ due to the strong dependency of SSB with SWH [4]. Later on, SSB estimates were obtained using fitted empirical models derived from two predictors retrieved from the analysis of altimeter data, the altimeter-derived SWH and wind speed (U10), with the latter based on radar backscatter cross-section measurements (σ^0). Since then, different statistical approaches have been considered to

better characterize the SSB, parametric formulations of both SWH and U10 in linear, polynomial or quadratic forms, estimating a number of coefficients [5], and nonparametric techniques using different statistical approaches as the kernel smoothing method [6], local linear kernel smoothing [7] or smoothing splines [8]. Before fitting the models, SSB estimates can be retrieved by sea surface height (SSH) differences at crossover points, along collinear tracks or directly estimated from the residuals between SSH and an MSS over the SWH and U10 domain [9]. More recently, [10] suggested that these methods, solely based on wave and wind information from the altimeter may be improved if additional surface gravity wave field measurements become available from numerical ocean wave model data, leading to an enhanced 3-dimensional (3D) SSB model derived from SWH, U10 and a third predictor characterized by the mean wave period (Tm), retrieved from WAVEWATCH III (WW3) [11]. This improved SSB model achieves positive results in reducing SSH variance both at global and regional scales, but the required external information from WW3 adds a new source of uncertainty which may not be directly related to the altimetric signal.

In another field of study, several models have been proposed [12, 13, 14, 15, 16, 17] to retrieve the wave period information (Tm, Tz) exclusively from the radar altimeter signal, combining both SWH and σ^0. In the scope of this paper, the algorithms proposed by [14, 15] were selected for evaluation, due to their simplicity, ease of implementation and good agreement when compared with buoy measurements. This paper proposes a simple formulation for a new SSB empirical model using three predictors (SWH, U10, Tz) solely derived from altimetric information, fitted with smoothing splines methods embedded in a general framework provided by Generalized Additive Models (GAMs).

The paper is organized as follows. Section 3.3 describes all the methodology used for model design. The approach used to estimate reliable SSB predictions, is explained in section 3.3.1. The considered mean wave period algorithms for this study are exposed in section 3.3.2 and the chosen nonparametric statistical approach is presented in section 3.3.3 . All the obtained results are shown in section 3.4 . Section 3.5 and section 3.6 provide discussion and conclusions.

3.3 Data and Methods

All the satellite altimeter and WW3 data were retrieved from the Radar Altimeter Database System (RADS), a validated and cross-calibrated source of Geophysical Data Records (GDRs) for all altimetric missions, incorporating the most up-to-date altimeter data, the latest instrument and geophysical corrections from several external datasets and models [18, 19]. RADS delivers a consistent altimeter database at 1-Hz, flexible enough to construct the sea level anomaly (SLA) either from a predefined or user-defined criteria. Table 3.1 describes the most relevant parameters and chosen criteria used for querying and retrieving the database information. This work concerns the entire phase A of Jason-1 mission, from cycle 001 to 260. The main reasons for this choice were the fact that we are dealing with one of the longest altimetric missions with

a time span from 15 January 2002 to 26 January 2009 and because the two most used and widely accepted SSB models, the CLS nonparametric sea state bias (SSB CLS) from [7] and the nonparametric sea state bias combined with WW3 (SSB Tran) from [11] are available for this mission, thus allowing an in-depth comparative analysis with the proposed model from this study.

Table 3.1: Description of the various RADS parameters and limits used. For this SSB study the limits of SWH, U10 and σ^0 were chosen in order to use all the available information. Parameters min, max and RADS reference code are presented.

name (units)	**code**	**min**	**max**
sea level anomaly (m)	0	-5	5
latitude (degrees)	201	-60	60
Ku-band significant wave height (m)	1701	0	10
altimeter wind speed (m/s)	1901	0	30
Ku-band backscatter coefficient (dB)	1801	0	16
std dev of Ku-band range (m)	2002	0	0.4
number of valid Ku-band measurements	2101	16	21
surface type	2504	0 = open ocean	
corruption of altimeter measurement	flag7	0 = ok	

3.3.1 Direct estimation of sea state impacts

An empirical determination of the SSB correction from the altimeter measurements is frequently made by extracting the related signal from sea surface height measurements. Before any SSB determination, a careful analysis of the SSH observations is necessary to detect possible instrumental or geophysical errors in order to avoid non-SSB signals which may corrupt the estimates to be modelled afterwards. The SSH measured at one particular location and uncorrected for SSB, contains the geoid signal (h_g), the ocean dynamic topography (η), the SSB effect and all other instrumental and geophysical errors represented by (ω):

$$SSH = h_g + \eta + SSB + \omega \tag{3.1}$$

Usually, the SSB is estimated by differencing the repeated measurements either along collinear tracks [20] or at orbit crossover points [5], but [9] proposed a simpler direct technique where sea height deviations from the marine geoid are binned against altimeter U10 and SWH, becoming an easier method to implement, directly solving for SSB by imposing a constant a priori mean sea level at each altimeter observation location thus eliminating the geoid. The following equation represents this relation:

$$SSB\,(U10, SWH)_{bin} = \langle (SSH - MSS) \rangle_{bin} \tag{3.2}$$

where the left side of equation (3.2) denotes the SSB estimation in U10 and SWH domains, function of the difference between SSH and MSS, bin-averaged for the same domain. Besides the ease of implementation, another big advantage of the direct method is the high resolution of the final estimation, allowing to the determine a more detailed model when compared with other methods. Some disadvantages of this technique should be considered, the presence of some noisy estimates near the domain limits requires a proper treatment, and the impossibility to compute SSB estimations outside the domain range confined by the limits of SWH and U10 [21]. In this work, the direct estimation of sea state impacts was implemented in order to give a reliable SSB prediction, used as an input for the final response which will be modelled.

3.3.2 Mean zero up-crossing period ($\mathbf{T_m}$, $\mathbf{T_z}$)

The wave period parameter is characterized by the interval between successive waves, obtained by averaging all wave periods measured in a time interval divided by the number of waves in this interval. A special case is the mean zero-crossing period $\overline{T_0}$ described by:

$$\overline{T_0} = T_{m_{02}} = T_z = \sqrt{m_0/m_2} \tag{3.3}$$

where m_0 and m_2 are the zeroth- and second-order moments of the variance density spectrum $E(f)$. In the scope of this work, $T_{m_{02}} = T_z$ was the chosen mean wave period parameter, due to its reliability and for a better comparison with the proposed mentioned wave period algorithms by [14] (hereafter G03) and [15] (hereafter Q04). G03 suggested a simple empirical model for wave period retrieval, using the Ku-band radar altimeter backscatter and significant wave height, formulated with an heuristic model based on collocated buoy observations and TOPEX altimeter data $T \sim \left(\sigma_L^0 SWH^2\right)^{0.25}$. The model was built by performing a linear regression in the *log* domain of wave period from T against with the altimeter σ^0 expressed in its linear (non-dB) form:

$$log_{10}\left(T_z\right) = 0.361 + 0.967 * log_{10}\left(\sigma_L^0 SWH^2\right)^{0.25} \tag{3.4}$$

A regional assessment of the model was also performed by the authors, concluding that G03 is better suited to wind-dominated seas than to regions with swell. Additionally to this, [22] compared the G03 model with National Data Buoy Center (NDBC) buoys and the European Centre for Medium-Range Weather Forecasts (ECMWF) ERA-40 dataset, and suggested that altimeter-derived mean wave period is reliable even in swell conditions for moderate to high winds (above 4 m/s), in contrast to previous studies which limited its validity just to wind-dominated seas. Based on the fact that σ^0 is related with the ocean surface wave mean square slope statistics, Q04 proposed two algorithms to estimate an altimeter-derived mean wave period using methods based on neural networks. A first method based solely on the altimeter Ku-band measurements, and an alternative method T_{nn}^2, the one that has been used in this work, which gathers information from both C and Ku band radar cross sections together with wind speed

(U10) for a better constraint of the wind sea contribution. T_{nn}^2 operates with the dual-frequency capability of altimeters, thus allowing a better retrieval of the local environmental conditions and showing a good agreement with the mean wave period observations from NDBC buoys.

$$\begin{aligned} T_{nn}^2 &= \exp(5.7474 - 1.4688a + 1.7943b), \\ a &= \frac{\sigma_{Ku}^{0.3082}}{\sigma_C^{0.2352} SWH^{0.0981}} \exp(1.5068b), \\ b &= \frac{2}{1 + \exp(-1.8612 - 0.08U10)} - 1 \end{aligned} \tag{3.5}$$

There is some discussion about the σ^0 upper limit that should be used, Q04 mention an upper threshold of 16 dB for Ku-band and 20 dB for C-band, considering that the measurements beyond these thresholds correspond to surface slicks for which there are no surface waves. On the other hand, [16] applied a threshold of 13 dB stating that above this value, σ^0 is no longer related to the wave period. For this work, a threshold of 16 dB for Ku-band σ^0 was applied, leaving the C-band free and the resulting mean wave period T_z with a valid range between 1 s and 16 s, since outside this range there might be some inefficiency of the applied models.

3.3.3 Smoothing splines with GAMs

The chosen approach for SSB modelling was based on smoothing spline methods embedded in a general framework provided by Generalized Additive Models (GAMs) [23, 24]. The first thing that must be given attention to, is how to find a smooth curve that fits the observed data well, minimizing the residual sum of squares $RSS = \sum_{i=1}^{n} (y_i - g(x_i))^2$. Such a function has to be chosen carefully, otherwise it will be too flexible, overfitting the data. To accomplish this task, it is necessary to add a penalty term, penalizing steep slopes and variability of f:

$$\sum_{i=1}^{n} (y_i - f(x_i))^2 + \lambda \int f''(t)^2 \, dt \tag{3.6}$$

the fitting procedure takes the new form of a *loss+penalty* function where λ is a nonnegative *tuning parameter* for roughness control and can be chosen manually, based on data variability analysis or by cross-validation techniques. The smoothing spline function $f(x)$ that minimizes (3.6) is a piecewise cubic polynomial with a number of knots, smoothed by a continuous first and second derivatives. The SSB model was designed using a generalized additive model (GAM) thus extending the range of a multiple linear regression model and allowing nonlinear relationships between each predictor and the response:

$$Y_i = \beta_0 + f_1(x_{i1}) + f_2(x_{i2}) + \ldots + f_p(x_{ip}) + \epsilon_i \tag{3.7}$$

where a separate cubic regression spline f_j with λ=6 was applied to each predictor x_{ij} and added together in the final framework. The additive properties of the model allows an individual contribution analysis of each x_{ij} on Y_i while holding all the other variables fixed, providing this way a useful compromise between linear and fully nonparametric models. For this work, the goal was to design a SSB model using three predictors $(X_{i1}, X_{i2}, X_{i3}) = (SWH_i, U10_i, T_zG03)$, evaluating the impact of the third predictor in the final response, the goodness of fit, simplicity and smoothness, without data overfitting.

3.4 Results

The flowchart presented in figure 3.1 attempts to clarify the main steps involved in the proposed SSB modelling and how they relate. After retrieving the satellite altimeter information from RADS, a careful selection criteria had to be applied, conditioning some parameters limits. The entire range of SWH and U10 up to the limits of 10 m and 30 m/s respectively, were considered. A bin-averaged procedure for the SWH-U10 domain has been applied, producing a preliminary training dataset which had to be supervised by subsetting and weighting strategies before feeding the model. A screening method for outliers detection has been implemented before the model testing phase.

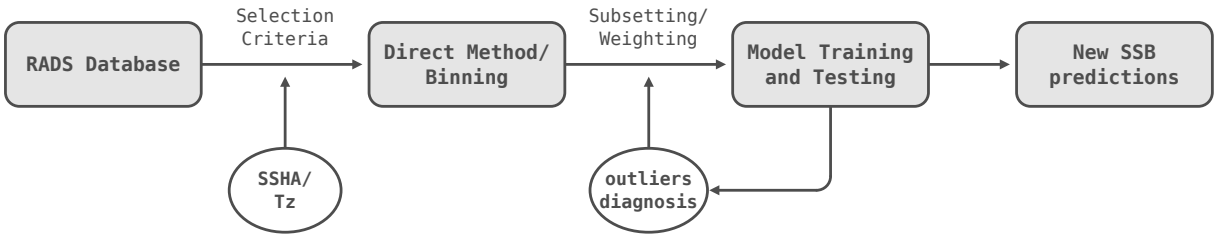

Figure 3.1: Flowchart diagram with the main steps of the model design. Starting on the left side, with altimetric data input, new parameters computation and selection criteria for binning procedure, and finishing on the right with strategies used for SSB modulation and predictions.

3.4.1 Mean Wave Period assessment

Aiming at selecting an appropriate algorithm to determine the mean wave period from altimetric data, a thorough assessment was performed for the first 50 cycles of Jason-1, comparing G03, Q04 and the mean wave period $T_z = \sqrt{m_0/m_2}$, where m_0 and m_2 are the wave spectral moments of the wave model WW3 obtained from RADS. Three histograms are presented in figure 3.2 showing that about 20 million measurements were considered valid.

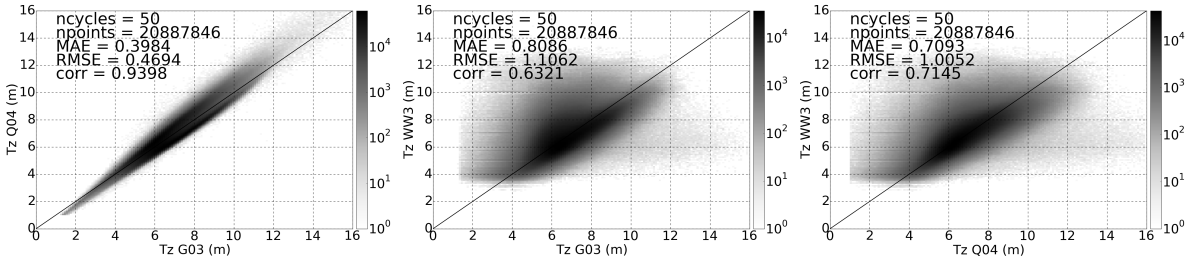

Figure 3.2: Statistical analysis of mean wave period algorithms G03, Q04 and the Tz derived from numerical wave model WW3 (from left to right), for the first 50 cycles of Jason-1. All plots displaying the number of validated measurements, mean absolute error (MAE), root mean square error (RMSE) and correlation between measurements.

As expected, the algorithms from G03 and Q04 have large correlations, higher than 0.9, and relatively low mean absolute and root mean square differences, pointing up that both models are coherent with each other for the considered data span. The right plot shows how G03 relates with the mean wave period derived from WW3. Despite the slightly worse results, with higher mean absolute and root mean square differences, the correlation between both datasets remains above 0.6. Similar results were obtained for Q04 (middle plot) revealing an identical behaviour with G03 when compared with Tz from WW3. To overcome the systematic underestimation of the swell in WW3 pointed by Q04 and the suggested evidence that G03 is better suited for wind-dominated seas than to swell regions, [22] defined a swell ratio (SR) characterized by the ratio between the swell wave height directly retrieved from the numerical wave model, and the SWH obtained from the model zeroth-order moment of the variance density spectrum with $4\sqrt{m_0}$. Taking advantage of the fact that RADS provides the swell wave height of WW3, it was possible to define a SR < 0.9, applied to the initial dataset, thus filtering out measurements from swell-dominated sea states. Figure 3.3 shows a new set of two-dimensional histograms and associated statistics when SR is activated.

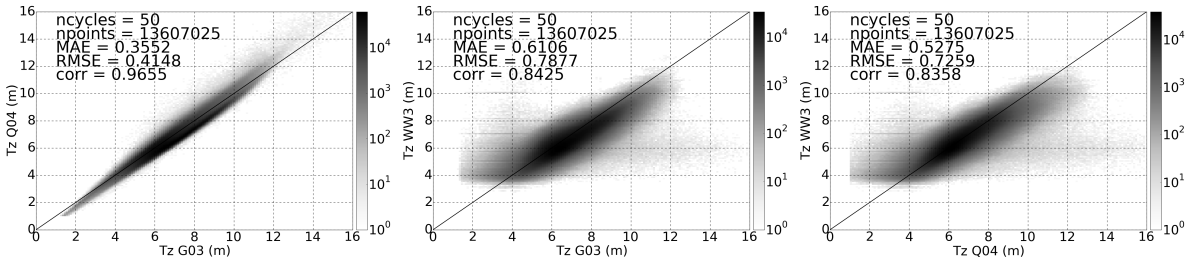

Figure 3.3: Statistical analysis of mean wave period algorithms G03, Q04 and the Tz derived from numerical wave model WW3 (from left to right), for the first 50 cycles of Jason-1 with *swell ratio* < 0.9 activated.

As shown in figure 3.3, when the SR limit is activated, the number of measurements decreases by about 30%. The correlation between G03 and Q04 algorithms is still extremely high, but unlike the previous scenario, here the correlation between G03 algorithm and WW3 model increases considerably to values higher than 0.8, suggesting that G03 is better related with

the part of the wave spectrum that is under direct influence of the wind, particularly wind seas directly generated and affected by local winds. Again, a similar behaviour is obtained for Q04 when compared with WW3, highlighting the similarities between the two considered algorithms. Despite the better results, SR was not considered for the development design of SSB model in this study, since the swell wave height is a parameter exclusively retrieved from numerical wave models and not from altimeter data. To complement this assessment, a global spatial analysis covering the first 50 cycles of Jason-1 was performed, correlating G03 and Q04 with the mean wave period derived from WW3, shown in figure 3.4. It is clear to observe a latitude dependency with an increase of correlation for higher latitudes, but overall, there is a good statistical relationship between both algorithms when related with WW3.

After a careful analysis of the two mean wave period algorithms and how they relate with the same parameter derived from the numerical wave model, it is safe to assume that both G03 and Q04 algorithms produce similar estimates when compared against WW3 model retrieved from RADS. Due to a simpler approach and ease of implementation, G03 was the chosen algorithm to be the third predictor of SSB modelling, mediating the relationship between SWH and U10 retrieved from the altimeter.

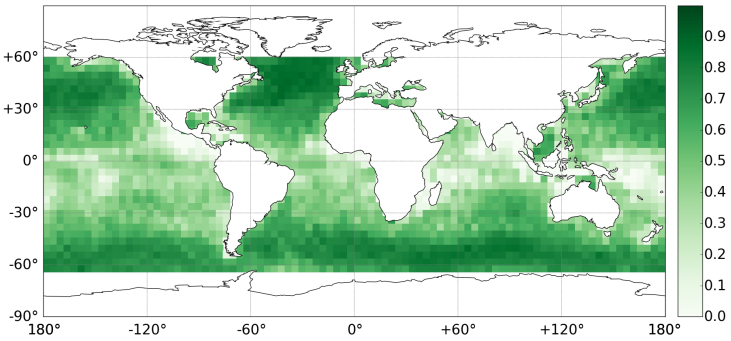

Figure 3.4: Global correlation between T_zG03 and T_zWW3. Data were binned in lat-lon squares of 4° by 4° with SR deactivated. Largest correlations are found at high latitudes, predominantly in swell ocean regions.

3.4.2 SSB Modeling procedures and design

The direct method of sea state impacts was implemented in order to give a reliable SSB estimation input for the final model. The method is characterized by the computation of the SSH uncorrected for SSB and binned afterwards against altimeter U10 and SWH, by imposing a constant a priori mean sea level at each altimeter observation location, thus producing a Sea Surface Height Anomaly (SSHA) uncorrected for SSB. For this work, the global high resolution mean sea surface DTU13 from DTU Space [25], available in RADS, was adopted. The direct method was implemented with a bin width of 0.25 m/s in U10 and 0.25 m in SWH, following the same procedure described by [9]. Instead of a bin-averaged computation, a more robust parameter of central tendency like the median was chosen, thus allowing lower discrepancies in the extremes of SSHA domain.

A training dataset estimated for the first 3 years of Jason-1 (first 112 cycles) produced a raw SSHA output with 3821 bins, which had to be subjected to a preliminary assessment in order to improve the bins quality for subsequent application. After evaluation, it was decided to discard all bins with less than 300 measurements, thus reducing the initial output to 2332 bins, i.e., 60% of the initial number. Table 3.2 shows important information about the model predictors (SWH, U10, TzG03) and the response that will be modelled, the median of SSHA. The summary statistics does not reflect the real differences between the median and the mean of SSHA, but a preliminary assessment showed that the median is less affected by the points with extremely low values of SWH. Also from the table below, it is already possible to have a better idea of the final SSB that will be modelled looking at the SSHA median with a range between -0.32 m and -0.01 m.

Table 3.2: Binning summary statistics with all parameters and metrics considered per bin. 2332 bins were validated to estimate a training dataset considering the first 3 years of Jason-1 mission. Bins with less than 300 measurements were discarded.

name (statistic)(units)	**n**	**mean**	**std**	**median**	**min**	**max**
SWH (median) (m)	2332	4.88	2.39	4.87	0.40	9.88
U10 (median) (m/s)	2332	11.96	5.73	11.88	1.22	22.62
SSHA (mean) (m)	2332	-0.17	0.08	-0.18	-0.32	0.00
SSHA (median) (m)	2332	-0.17	0.07	-0.18	-0.32	-0.01
SSHA (std) (m)	2332	0.12	0.01	0.12	0.09	0.21
SSHA (mad) (m)	2332	0.09	0.01	0.09	0.06	0.12
SSHA (npoints)	2332	n.a.	n.a.	n.a.	300	673359
Tz G03 (median) (s)	2332	8.25	1.95	8.59	2.77	11.73

After analysing the behaviour of each predictor with the response, it was necessary to control the weight of each bin in the model design. This weighting procedure uses the number of points and the standard deviation associated to each bin and applies an increasing and decreasing ramp function ($1 - e^{-x}$ and e^{-x}) based on natural exponential functions. Diagnostic tests based on histograms, residual plots and fitted values vs their response, had to be performed for convergence analysis of the smoothness selection optimization and to study the impacts of the fitting procedure on the results. After this step, a robust method to identify and eliminate existing outliers based on residuals analysis was applied, where the predicted values with associated residuals larger than 2 standard deviations (2σ), were considered outliers and removed accordingly. After this procedure, the initial dataset of 2332 bins decreased to 2174 bins, i.e., a reduction sample of 7%. It was observed a good agreement between the fitted values and response, with an extremely low dispersion for the entire analysed domain and a normal distribution without skewness, indicating also a good agreement between the fitted values and the response.

In order to evaluate the third predictor impact in the final response, two approaches were considered for the checking assessment and to choose the best candidate of SSB model design.

1. $\text{SSB}_{2P} = \beta_0 + f_1\,(SWH) + f_2\,(U10)$
2. $\text{SSB}_{3P} = \beta_0 + f_1\,(SWH) + f_2\,(U10) + f_3\,(T_zG03)$

where f_1, f_2 and f_3 are the smooth functions indicating the individual impact of each predictor. To accomplish this selection, the methodology for choosing the best model performance was based in a number of statistical parameters presented in table 3.3: Akaike Information Criterion (AIC), Generalized Cross Validation (GCV), coefficient of determination (R^2) and Analysis of Variance (ANOVA). Comparing the performance of the two tested models, SSB_{3P} appears to be the one that fits better the response with lower AIC and GCV, and higher deviances explained by R^2. The ANOVA test results show low P values between the models, which indicates that we can reject the null hypothesis and consider statistical significant incorporating more nonlinear effects for model improvement.

Table 3.3: Overall statistical performance of the two tested approaches. A verified reduction of Akaike Information Criterion (AIC) and Generalized Cross Validation (GCV) from SSB_{3P} relative to SSB_{2P}, indicating a more optimized model performance when a third predictor is considered. Coefficient of determination (R^2) and Analysis of Variance (ANOVA) reinforce the same assumption.

model	**AIC**	**GCV**	$\boldsymbol{R^2}$	**ANOVA Pr(>Chi)**
1. SSB_{2P}	-13470	$18.1\text{x}10^{-5}$	0.9668	—
2. SSB_{3P}	-17067	$38.8\text{x}10^{-6}$	0.9929	$2.2\text{x}10^{-16}$

Due to the interdependencies between predictors, where U10 = $f(\sigma^0)$ and TzG03 = $f(SWH, \sigma^0)$, both SSB_{2P} and SSB_{3P} are established using only two satellite derived products (SWH and σ^0), but the addition of TzG03 can be considered as a mediator term, thus adding more information to the model on how SWH and σ^0 correlate. The impact of TzG03 is evaluated in terms of how this predictor explains the variability of the model response traduced by the SSB estimation.

Figure 3.5 shows a comparative analysis, for the same training dataset, between the SSHA after evaluation, the established SSB models (SSB CLS and SSB Tran), a simple linear empirical model using a first order predictor, and the two fitted models designed with two and three predictors (SSB_UPT_2P and SSB_UPT_3P).

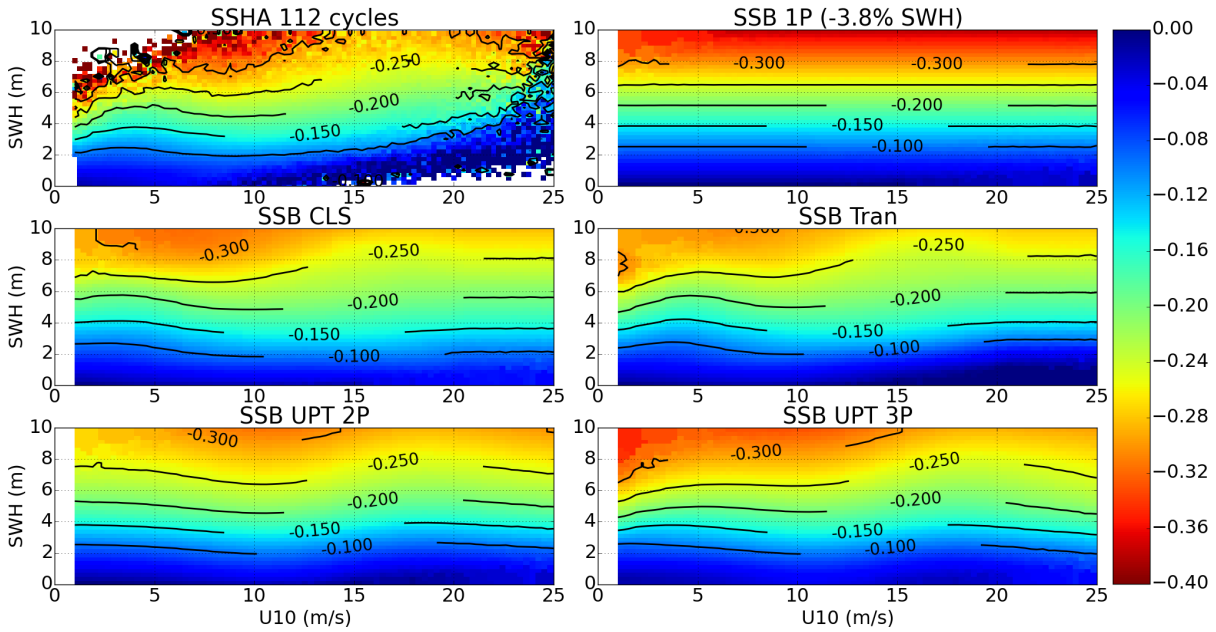

Figure 3.5: Training dataset of SSHA (top left) and different SSB models outputs for SWH-U10 domain considering the same dataset. A linear empirical model using only one predictor computed by -3.8% of SWH (top right), the two established SSB models (SSB CLS and SSB Tran on middle left and right, respectively) currently available in Jason-1 mission, and the two SSB models designed on this study (bottom left and right).

In figure 3.5, it is possible to observe some noise in the fringes of SSHA for ocean swell regions (high SWH and low U10) and young seas regions (low SWH and high U10) that had to be smoothed by the final model. A first order SSB parametrization computed by -3.8% of SWH shows what should be the SSB linear behaviour in the domain considered and its strong dependence with respect to wave height. The two predictor model SSB_UPT_2P shows a clear agreement with SSB CLS, even in those regions characterized with high wave heights and wind speeds, indicating an appropriate choice of the procedures taken for model design and strategies adopted. A good agreement can also be observed between SSB_UPT_3P and the 3-dimensional model SSB Tran, showing the contribution of TzG03 in explaining the SSB variability for regions with U10 $<$ 5m/s, clearly demonstrating the impact of this third predictor when compared with SSB_UPT_2P.

3.4.3 Model testing with new SSB predictions

In order to better evaluate SSB_UPT_3P performance, new predictions were produced for a testing dataset, giving a new set of values not used to train the model and ranging between cycles 150-260 of Jason-1. Figure 3.5 shows that similar results were obtained for SSB_UPT_3P when computed for a testing dataset, revealing a well trained procedure with 3 year data from the first 112 cycles. There is a slight overestimation when compared with SSB Tran, especially in the region where SWH $>$ 6m and 5m/s $<$ U10 $<$ 10m/s, but not verified when compared

with SSB CLS. The impact of TzG03 is again verified and traduced by the isolines shrinkage observed in low wind regions with SSB predictions varying almost 15 cm for 2m < SWH < 7m which is consistent again with the SSB Tran model.

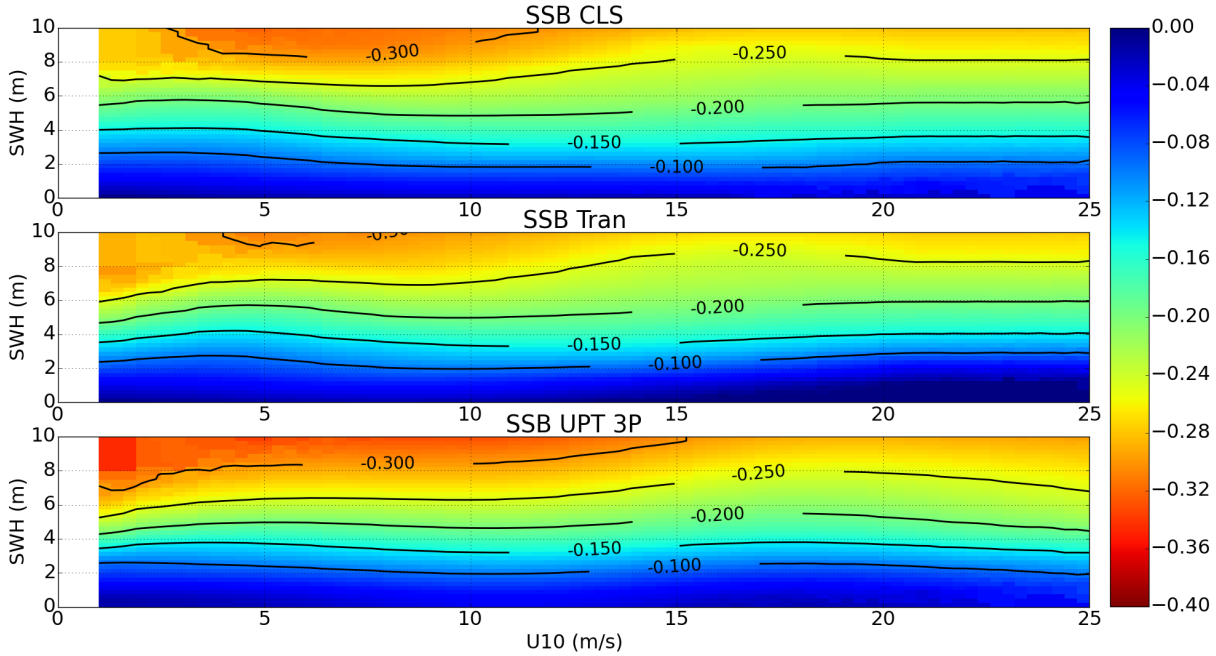

Figure 3.6: SSB performances for a testing dataset ranging between Jason-1 cycles 150-260 in SWH-U10 domain. From top to bottom, SSB CLS approach using the two classic predictors (SWH and U10), SSB Tran modulation using the same previous predictors, but adding the extra mean wave period information derived from WW3, and the proposed model design SSB_UPT_3P with TzG03 acting as a mediator parameter, interacting with SWH and U10.

A spatial statistic assessment was performed with scaled Sea Level Anomalies (SLA) variance differences based on collinear analysis, where the satellite data were binned in lat-lon squares of 4° by 4°. The scaled SLA variance differences are shown to better illustrate the impact of different SLAs relative to the region variability, and are determined by $S = [(var(SLA_1) - var(SLA_2))/var(SLA_1)] * 100$. Figure 3.7 represents a global assessment of the scaled SLA differences for SLAs computed with SSB_UPT_3P and SSB Tran for the entire phase A of Jason-1 mission, thus showing better performances of SSB_UPT_3P (blue) in the swell regions of Pacific and Atlantic oceans, but a poorer behaviour espe-

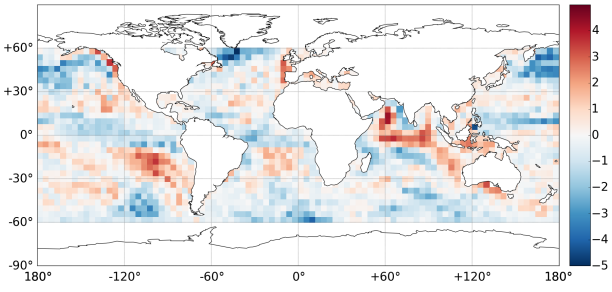

Figure 3.7: % of scaled sea level anomalies (SLA) variance differences between SLAs computed with SSB_UPT_3P and SSB Tran. Blue squares represent regions with a decrease in SLA variance computed with the proposed SSB model with respect to SSB Tran. Red squares indicate regions where an increase in SLA variance from SSB_UPT_3P relative to the SLA variance computed with SSB Tran is observed.

cially in the North Indian ocean, Indonesia region and west side of South America. This result could be explained due to a verified underestimation of TzG03 for some seasons in these regions when compared with WW3.

Table 3.4 resumes the statistical parameters of the different SSB models for the whole phase A mission of Jason-1 with the corresponding performance in SLA variance reduction. The last column presents each SSB correction impact on SLA variance reduction with respect to the scenario when no SSB correction is applied. The measure of central tendency shows conformity between the standard models and the proposed one. All three approaches have equivalent SSB standard deviations in explaining the response variability, which is consistent with the estimated variance reduction of SLA verified in some geographical regions with the SLA computed with SSB_UPT_3P.

Table 3.4: Summary statistics of the SLA computed with different SSB models for the whole phase A of Jason-1 mission, where conformity between the proposed model SSB_UPT_3P and the established SSB approaches is verified. Last column shows each SSB correction impact on SLA variance reduction. All values in cm with exception to varSLA which is in cm^2.

model	**mean**	**std**	**min**	**max**	**varSLA** $\downarrow$
SSB 1P	-9.96	5.04	-38.0	0.0	24.397
SSB CLS	-11.15	4.74	-32.1	-0.4	25.101
SSB Tran	-10.69	4.67	-30.9	3.7	25.117
SSB UPT 3P	-10.87	5.10	-34.8	-1.2	25.265

Even though the favorable performance of SSB_UPT_3P in estimating a correction in line with the standard SSB models, some differences are still verified specially in the edges of SWH-U10 domain. The results shown in figure 3.7 and table 3.4 could not be only explained by the fact that SSB_UPT_3P is using a third predictor not implemented in SSB Tran and SSB CLS, but instead by the different statistical techniques used. Standard models use the same local-linear kernel smoothing approach, which can produce different impacts on model predictions, specially at the edges of SWH-U10 domain with more variability. However, the smoothing splines technique, being a direct basis expansion of the original data, is flexible enough by choosing the number and locations of the knots used in those regions that could change rapidly.

3.5 Discussion

The presented work shows a new approach for SSB modelling based on three predictors derived only by altimetric information. A preliminary assessment was made to evaluate the performance of two different mean wave period algorithms when compared with WW3 numerical wave model, leading to the selection of the proposed algorithm by [14] due to its simplicity, ease of implementation, and efficiency in estimating the mean wave period for different ocean regimes and seasons.

The direct estimation method proposed by [9] was implemented to obtain a reliable SSHA input for modelling. Despite the good results, the method produces some noisy estimations in the fringes of SWH-U10 domain, needing to be tweaked by weighting techniques and bins cleaning procedures before use.

The method shows a good estimating performance with fewer cycles as input, suggesting that is possible to estimate a reliable SSB correction with a smaller training dataset, an important feature for the computation of SSB models for future missions, during the initial period of the mission.

The adopted SSB modelling approach with penalized spline smoothing embedded in a general framework provided by GAMs, reveals to be a straightforward modelling tool with a good compromise between flexibility, reduced computational requirements and accuracy of results. This technique is also expandable to accommodate interactions between explanatory variables, providing a deeper knowledge on how different predictors correlate together.

Two SSB models designs (SSB_UPT_2P, SSB_UPT_3P) were tested and subjected to a careful assessment of quality checking and residual analysis. SSB_UPT_3P exhibits a good performance when compared with the established SSB models (SSB CLS, SSB Tran), with predictions in line with [11] 3-dimensional model, especially for swell ocean regions. Although there is a total SLA variance reduction of almost 15 mm^2 for all the phase A of Jason-1, a spatial mixed performance in SLA variance was also verified, with ranges between 3-4% of SLA variance reduction and a 2-3% of SLA variance increase when compared with SSB Tran model.

3.6 Conclusion

This new technique aims to be a fast and reliable approach for SSB computation, combining three nonlinear predictors in a model design provided by an effectively modelling approach as the smoothing splines integrated with Generalized Additive Models. The third predictor represented by the selected mean wave period algorithm TzG03, has a low impact on SSB when compared with SWH and U10, but has the role of a mediator parameter influencing the model input with the interaction between SWH and U10. The achieved results show a clear improvement when the model gathers this extra information about the sea state conditions. The proposed approach was designed with simplicity and reliability in mind, despite some detected deficiencies of the used mean wave period algorithm when compared with WW3, it has been proven that it has a good performance for a wide range of ocean conditions, providing the best compromise between simplicity and reasonable results. While the simplest approach was privileged, this choice does not eliminate the possibility of implementing alternative algorithms in the future.

As a final note, it should be emphasized that it is not the aim of the proposed method to be better than the established SSB models, but instead, to provide an alternative procedure for a reliable model, in line with the best current models, easy to handle and control, flexible enough to be adapted for other altimetric missions, in particular for forthcoming missions.

Acknowledgments

This work was funded by the European Space Agency (ESA) Support to Science Element (STSE) Program, in the scope of project SCOOP - SAR Altimetry Coastal & Open Ocean - Performance Exploitation and Roadmap Study.

Author Contributions

Nelson Pires and M. Joana Fernandes conceived the experiments; Nelson Pires designed and performed the experiments; All authors analyzed the data and reviewed the study; Nelson Pires wrote the paper.

References

1. Melville, W.K.; Stewart, R.H.; Keller, W.C.; Kong, J.A.; Arnold, D.V.; Jessup, A.T.; Loewen, M.R.; Slinn, A.M. Measurements of electromagnetic bias in radar altimetry. J. Geophys. Res. 1991, 96, 4915–4924.
2. Chelton, D.B.; Ries, J.C.; Haines, B.J.; Fu, L.L.; Callahan, P.S. Satellite altimetry, in Satellite Altimetry and Earth Sciences edited by L. Fu and A. Cazenave. Int. Geophys. Ser. 2001, 69, 1–31.
3. Ghavidel, A.; Schiavulli, D.; Camps, A. Numerical Computation of the Electromagnetic Bias in GNSS-R Altimetry. IEEE T. Geosci. Remote 2006, 54, 489–498.
4. Born, G.H.; Richards, M.A.; Rosborough, G.W. An empirical determination of the effects of sea state bias on SEASAT altimetry. J. Geophys. Res. 1982, 87, 3221–3226.
5. Gaspar, P.; Le Traon, P.; Zanife, O. Estimating the sea state bias of the TOPEX and POSEIDON altimeteres from crossover differences. J. Geophys. Res. 1994, 99, 24981–24994.
6. Gaspar, P.; Florens, J. Estimation of the sea state bias in radar altimeter measurements of sea level: Results from a new nonparametric method. J. Geophys. Res. 1998, 103, 803–814.
7. Gaspar, P.; Labroue, S.; Ogor, F. Improving Nonparametric Estimates of the Sea State Bias in Radar Altimeter Measurements of Sea Level. J. Atmos. Ocean. Technol. 2002, 19, 1690–1707.
8. Feng, H.; Yao, S.; Li, L.; Tran, N.; Vandemark, D.; Labroue, S. Spline-Based Nonparametric Estimation of the Altimeter Sea-State Bias Correction. IEEE Geosci. Remote Sens. Lett. 2010, 7, 577–581.
9. Vandemark, D.; Tran, N.; Beckley, B.; Chapron, B.; Gaspar, P. Direct estimation of sea state impacts on radar altimeter sea level measurements. Geophys. Res. Lett. 2002, 29, 2148.
10. Tran, N.; Vandemark, D.; Chapron, B.; Labroue, S.; Feng, H.; Beckley, B.; Vincent, P. New models for satellite altimeter sea state bias correction developed using global wave model data. J. Geophys. Res. 2006, 111.
11. Tran, N.; Vandemark, D.; Labroue, S.; Feng, H.; Chapron, B.; Tolman, H.L.; Lambin, J.; Picot, N. Sea state bias in altimeter sea level estimates determined by combining wave model and satellite data. J. Geophys. Res. 2010, 115, 1–7.

12. Davies, C.G.; Challenor, P.G.; Cotton, P.D. Measurement of wave period from radar altimeters. Ocean wave measurement and analysis. Am. Soc. Civ. Eng. 1997, 819–826.

13. Hwang, P.; Teague, W.; Jacobs, G.; Wang, D. A statistical comparison of wind speed, wave height, and wave period derived from satellite altimeters and ocean buoys in the Gulf of Mexico region. J. Geophys. Res. 1998, 103, 10451.

14. Gommenginger, C.P.; Srokosz, M.; Challenor, P.; Cotton, D. Measuring ocean wave period with satellite altimeters: A simple empirical model. Geophys. Res. Lett. 2003, 30, 2150.

15. Quilfen, Y.; Chapron, B.; Collard, F.; Serre, M. Calibration/Validation of an Altimeter Wave Period Model and Application to TOPEX/Poseidon and Jason-1 Altimeters. Mar. Geod. 2004, 27, 535–549.

16. Mackay, E.; Retzler, C.H.; Challenor, P.; Gommenginger, C.P. A parametric model for ocean wave period from Ku band altimeter data. J. Geophys. Res. 2008, 113, 1–16.

17. Govindan, R.; Kumar, R.; Basu, S.; Sarkar, A. Altimeter-derived ocean wave period using genetic algorithm. IEEE Geosci. Remote Sens. Lett. 2011, 8, 354–358.

18. Scharroo, R. RADS Version 3.1 User Manual and Format Specification; 2012.

19. Scharroo, R. RADS Version 4.2.4 User Manual; 2016.

20. Chelton, D. The sea state bias in altimeter estimates of sea level from collinear analysis of TOPEX data. J. Geophys. Res. 1994, 99, 24995–25008.

21. Scharroo, R.; Lillibridge, J. Non-Parametric Sea-state Bias Models and Their Relevance to Sea Level Change Studies. In Proceedings of the ENVISAT/ERS Symposium, Salzburg, Austria, 6–10 September 2004.

22. Caires, S.; Sterl, A.; Gommenginger, C.P. Global ocean mean wave period data: Validation and description. J. Geophys. Res. 2005, 110, 1–12.

23. James, G.; Witten, D.; Hastie, T.; Tibshirani, R. An Introduction to Statistical Learning with Applications in R; Springer Texts in Statistics; Springer: New York, NY, USA, 2014.

24. Wood, S. Generalized Additive Models: An introduction with R; Chapman & Hall/CRC Texts in Statistical Science; CRC Press: Florida, FL, USA, 2006; Volume 62.

25. Andersen, O.; Knudsen, P.; Stenseng, L. The DTU13 MSS (Mean Sea Surface) and MDT (Mean Dynamic Topography) from 20 Years of Satellite Altimetry; Springer: Berlin, Germany, 2015.

Chapter 4

Article 2: Improved Sea State Bias Estimation for Altimeter Reference Missions with Altimeter-only Three-parameter Models

Nelson Pires [1], M. Joana Fernandes [1], Christine Gommenginger [2] and Remko Scharroo [3]

[1] Department of Geosciences, Environment and Spatial Planning, Faculty of Sciences, University of Porto, Porto 4169-007, Portugal
[2] National Oceanography Centre, Natural Environment Research Council, Southampton SO14 3ZH, UK
[3] European Organisation for the Exploitation of Meteorological Satellites, Darmstadt D-64295, Germany

Academic Editors: Simon Yueh and Daniel Henson

Received: 22 September 2017 / Accepted: 16 July 2018 / Published: 14 September 2018

Academic Journal: **IEEE Transactions on Geoscience and Remote Sensing**

IEEE TGRS **2018**; doi:**10.1109/TGRS.2018.2866773**

4.1 Abstract

This paper presents an in-depth study concerning the development of a Sea State Bias (SSB) model designed with three parameters exclusively derived from altimeter data and globally applied to all reference altimeter missions. The proposed technique, first tested for the Jason-1 mission, proves to have good performance for a wide range of ocean conditions when compared with the state-of-the-art SSB corrections currently in use. Additionally to Significant Wave Height (H_s) and Wind Speed (U_{10}), a third predictor acting as a mediator parameter gathered by the Mean Wave Period (T_z) has been used.

Two different empirical algorithms for altimeter ocean wave period have been tested and implemented, improving the SSB model performance in some ocean regions. The methodology relies on non-parametric modulation and statistical techniques based on smoothing splines embedded in a generalized additive model. This SSB modeling approach shows good performance when applied to all reference missions, in particular to TOPEX and Jason-2 missions, slightly reducing the explained variance of sea level anomaly when compared with the established SSB models. The approach is computationally efficient, capable of generating a stable SSB model using a small training dataset when little information is available, as is the case with the recent Jason-3 mission. Model performance is assessed by comparison with existing SSB corrections for each reference mission, inter-comparisons during the period of the tandem phases and by sea level anomaly variance analysis, providing a consistent set of SSB corrections for the four reference missions.

Keywords: radar altimetry; sea state bias; mean wave period; non-parametric estimation

4.2 Introduction

Radar altimetry is undoubtedly one of the most useful tools for ocean monitoring and dynamic sea surface height observations. The efficiency of this technique is entirely dependent on the accuracy of the measured altimeter range, satellite orbit, and on the correction models accounting for the errors from different origins (instrument, range and geophysical) that affect the altimeter observations. One of these inherent errors is the so-called sea state bias (SSB), which is an altimeter range error caused by the influence of ocean surface waves on the radar altimeter measurements.

SSB is mainly generated by wind-driven ocean gravity waves, and specifically by their weak non-linearity, which means they do not have a sinusoidal shape, but instead, present peaked crests and flatter troughs [1]. Usually, the SSB is characterized by the sum of three different contributions, generating a wave-height-dependent range bias in the retrieval of sea surface height. The first is the electromagnetic (EM) bias, which arises from an apparent depression of the mean sea level produced by signal-surface interactions [2]. It occurs because the wave troughs are better reflectors than the crests, thus overestimating the measured satellite-to-surface range

and causing the erroneous idea that the mean reflecting surface is depressed below mean sea level. The parasitic capillaries formed on wave crests are an additional factor since they scatter energy away from the altimeter and increase this depressed mean reflecting surface. The second contribution to SSB is the skewness bias. It refers to the additional apparent surface depression, linked to the effect of a non-Gaussian surface height distribution, inducing an error due to the difference between the determined median sea surface and the true mean sea surface (MSS). The third contribution, tracker bias, can occur due to retracking effects and an imprecise tracker determination of the midpoint location of the altimeter return or waveform leading edge [3].

While the EM bias arises from the physical characteristics of the sea state at a given moment, the tracker bias is unique to each instrument, so the SSB must be computed for each mission. To first order, the EM bias is linearly proportional to significant wave height (H_s), where this proportionality varies with the related wind speed (U_{10}) found at the illuminated altimeter footprint. With an order of magnitude ranging between 3%-4% of H_s, the SSB is a centimeter-scale measurement bias and remains one of the largest sources of uncertainty linked with the altimetric signal.

Several studies have been conducted to investigate the EM bias (embedded in SSB) with theoretical models [4]. Regardless of attempts of using geometrical optics [5,6,7] or physical optics theories [8,9], where the contributions from short waves is taken into account as well as the radar frequency dependencies, a full understanding of the physical phenomena associated with SSB has not yet been reached. Thus the current SSB models are mostly based on empirical approaches.

One of the main difficulties of using empirical methods to estimate a sea-state-related correction, from sea surface height (SSH) without absorbing oceanic variability and residual errors, has to do with the estimation methods that will feed the prediction models. Because of this, the SSB estimation process is usually performed by retrieving the SSH differences at crossover points with time differences less than the period corresponding to 1 repeat cycle [10,11] or along repeated satellite ground tracks by collinear analysis [12]. Alternatively, a more recent approach, and the one selected for this study, directly estimates the SSB from the residuals between SSH and a mean sea surface accurate enough to eliminate residual geoid signals [13].

Each method has its advantages and disadvantages, as presented in a recent study [14] and previous assessments [15]. Although it has to be used with care to minimize the introduction of spurious values in the estimated SSB, which may induce some possible correlation between the SSB estimation and oceanic signal [16,17], the direct approach has proved to be reliable and able to produce more detailed higher resolution SSB estimates when compared with the other methods. The study by [14] also shows that good performance with less input data is achievable with the direct method, thereby allowing reliable SSB corrections to be estimated with smaller training datasets. With other methods, typically, the shorter the time span of data available for model training, the less reliable are the produced SSB estimates. This subject will be one of the topics covered by this work.

Empirical SSB models are usually developed with parametric [10] or non-parametric [18,19] [SSB_{cls}] techniques based on two geophysical predictors, the altimeter-derived H_s and the wind speed (U_{10}) derived from the altimeter backscatter cross-section measurements (σ_0). While this approach can produce reasonable SSB model results, without dependency on external data sources, it is recognized that these two parameters alone are not sufficient to explain some of the SSH variability associated with ocean waves propagating in varying directions and interacting nonlinearly [20,21].

Several studies have tried, with more or less success, to explain more of the remaining SSH variability by using additional sea-state parameters. These were either obtained indirectly from altimeter-derived parameters such as Ku-band σ_0 or pseudo wave age [2,15,22] or by combining altimeter data with external predictions such as swell height, mean wave period or inverse wave age retrieved from numerical wave models WAVEWATCH III [23,24,25][SSB_{tran}] and WAM [11]. Despite the considerable number of additional parameters proposed in the literature to add extra information in the explanatory modeling of SSB, there is no consensus on the best approach. This is due to the insufficient information on the nonlinear characteristics of the oceanic surface, namely on the wind-waves physical proprieties involved in the SSB range effect in the altimeter signal.

SSB estimation also benefited from the development of more advanced statistical modeling approaches, leading to the operational SSB models undergoing significant improvements. Starting from simple parametric formulations in functional forms expressed as linear, polynomial or quadratic functions of H_s and U_{10} [10], they evolved to more complex statistical formulations using a variety of non-parametric techniques. Examples of such techniques are the kernel smoothing methods [18], local linear kernel smoothing [19,24] or smoothing splines embedded in a framework provided by Generalized Additive Models (GAM) [14,26].

Among the possible SSB correlatives that could be used to address some of the limitations found in SSB models based only on H_s and U_{10}, the mean wave period (T_z) seems to be the one gathering more consensus as a useful third SSB predictor, due to positive results in reducing the explained variance of the sea level anomaly (SLA) both at global and regional scales [11,24,26]. Numerical wave models such as WW3 [27] and WAM [28] are now capable of providing full two-dimensional gravity wave spectra, globally, and estimates of the mean wave period, which can be used as the third SSB model predictor. However, some studies indicate that it is also possible to indirectly retrieve the wave period information exclusively from the radar altimeter signal.

A number of expressions for altimeter wave period exist in the literature, combining both H_s and σ_0 using parametric formulations [29,30,31,32,33]. Previous work from [14] compared two different mean wave period algorithms proposed by G_{03} [30] and Q_{04} [31] with wave field statistics generated from the WW3, and developed new SSB estimates based on altimeter H_s, U_{10} and the altimeter wave period estimated with G_{03}. They concluded that, even though the altimeter mean wave period has a low direct impact on SSB when compared with H_s and U_{10}, it

still plays an important role as a mediator parameter, influencing the SSB model through more complex interactions between H_s and σ_0, leading to a clear improvement in SSB estimation when the model gathers this extra information from the sea state conditions. The same study reveals that this SSB model design provides good estimating performances from fewer cycles of altimeter data as input, suggesting that it is possible to estimate a reliable SSB correction with relatively small training datasets.

This paper is an extension of the SSB modeling approach first presented in [14], now applying it to all reference missions (TOPEX, Jason-1, Jason-2 and Jason-3), and improving the statistical modeling techniques with a more refined parameterization. The paper also presents an assessment of the model ability to predict reliable SSB values with limited altimetric data.

The paper is arranged as follows. In section 4.3 the data and methodology used for the proposed SSB model are described. Some of the conclusions reached in the previous study are recalled in order to choose the better mean wave period algorithm to be incorporated as the third model predictor. Preliminary results of SSB estimations computed with the direct technique are presented for all the reference missions as well as the decisions taken concerning the non-parametric statistical approach used for model generation and evaluation. Section 4.4 is dedicated to a thorough assessment of the different approaches for SSB modeling designs and training datasets for Jason-2. Section 4.5 describes the same procedure applied to TOPEX, Jason-1 and Jason-3. The tandem phases between the various altimetric missions were used in section 4.6 to evaluate the model robustness and coherency, making it possible to evaluate the instrumental errors inherent to each mission in the SSB correction. Finally, section 4.7 depicts the main conclusions of this study.

4.3 Data and Methods

4.3.1 Altimeter Measurements and Datasets

The TOPEX/Poseidon (TP) satellite mission launched in 1992, Jason-1 (J1) launched in 2001 and the currently operating missions OSTM/Jason-2 (J2) launched in 2008 and Jason-3 (J3) launched in 2016 contribute to the Integrated Multi-Mission Ocean Altimeter Data for Climate Research [34] dataset. This earth observation program has the commitment to deliver a coherent and consistent time series of SSH for the last 25 years from multi-mission altimeter data, meeting the most rigorous accuracy requirements. All these altimetric missions are in an approximately 10-day exact repeat orbit with 254 passes per cycle, collecting data between +/- 66 degrees at 1336km altitude. They possess a dual frequency radar altimeter using C-band (5.3 GHz) and Ku-band (13.6 GHz).

With consistency in mind, the data used for this work have been retrieved from the Radar Altimeter Database System (RADS), a validated and cross-calibrated source of Geophysical Data Records (GDRs) with 1-Hz sampling for all altimetric missions. RADS incorporates the most up-to-date altimeter data, the latest instrument and geophysical corrections from several

external datasets and models [35,36]. The data used in this study are those available in RADS for the 4 missions considered. All altimeter data are currently enhanced with the new DTU15 global high resolution MSS model developed by the Danish Technical University (DTU) [37], an important tool for SSB estimations from the most accurate residual sea surface heights, free from annual, semi-annual, seasonal, and spurious SSH signals.

4.3.2 Ocean Wave Period from Altimeter Data

In the radar altimeter processing, H_s and the backscatter coefficient, σ_0, routinely used to estimate near-surface wind speed, are retrieved by analyzing the shape and intensity of the altimeter radar echo reflected from the sea surface. Both the H_s and U_{10} parameters are well established and produce reliable measurements with accuracies of 0.5 m and 1.5 m/s respectively [38,39] when compared with in-situ buoys.

Previous studies showed that wave period information can be indirectly retrieved by relating altimeter H_s and σ_0 using empirical approaches. G_{03} [30] suggested a simple empirical model for wave period retrieval using the TOPEX Ku-band radar altimeter σ_0 and H_s, consisting of an heuristic model tuned with TOPEX altimeter data, collocated with National Data Buoy Center (NDBC) buoy observations in the form of $T \sim \left(\sigma_L^0 SWH^2\right)^{0.25}$. The algorithm was built by performing a linear regression in the log domain of wave period from buoy T_z against the altimeter Hs and σ^0 expressed in its linear (non-dB) form, σ_L^0, as:

$$log_{10}\left(T_z\right) = 0.361 + 0.967 * log_{10}\left(\sigma_L^0 {H_s}^2\right)^{0.25} \tag{4.1}$$

Subsequently, Q_{04} [31] proposed an altimeter-derived wave period algorithm for TP and J1 missions, based on neural network techniques, establishing a relationship between altimeter-derived H_s, σ_0 and T_z information, also retrieved from NDBC buoy measurements. The algorithm gathers information from both C- and Ku-band radar cross sections, together with U_{10}, for a better constraint of the wind sea contribution and operates with the dual-frequency capability of most altimeters. This approach allows a better retrieval of the local environmental conditions, showing a good agreement with the mean wave period observations from NDBC buoys. According to Q_{04}, the mean wave period formulation using both C- and Ku-band backscatter is given as:

$$\begin{aligned} T_z &= \exp(5.7474 - 1.4688a + 1.7943b), \\ a &= \frac{\sigma_{Ku}^{0.3082}}{\sigma_C^{0.2352} H_s^{0.0981}} \exp(1.5068b), \\ b &= \frac{2}{1 + \exp(-1.8612 - 0.08U_{10})} - 1 \end{aligned} \tag{4.2}$$

where T_z is the mean wave period in seconds and σ^0_C and σ^0_{Ku} are the backscatter coefficients in Ku and C bands respectively in decibels. Aiming at selecting the most appropriate algorithm to determine T_z, [14] performed an assessment of both algorithms for the first 50 cycles of J1 ($\sim$ 200 million measurements), comparing both G_{03} and Q_{04} with the zero-crossing wave period $T_z = \sqrt{m_0/m_2}$ computed from WW3 wave spectral moments obtained from RADS (Figure 4.1).

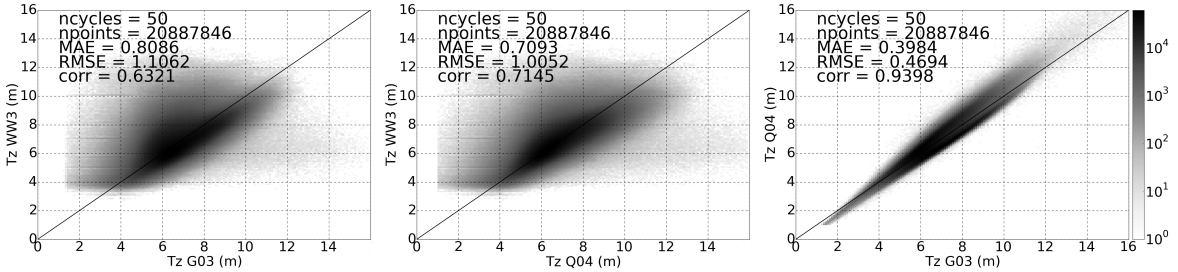

Figure 4.1: Statistical analysis of mean wave period algorithms G_{03}, Q_{04} and the zero crossing period T_z derived from numerical wave model WW3, for the first 50 cycles of J1 (from [14]).

This assessment showed a strong statistical relationship between G_{03} and Q_{04}, with a correlation of 0.94 and a root-mean-square error of 0.47 m, suggesting similarity between both algorithms for most oceanic conditions. Results also indicated better performance of Q_{04} relative to G_{03}, when compared with T_z from WW3, with 8% increase in correlation and 10% reduction in root mean square (RMS) and medium absolute error (MAE). The global spatial analysis (not shown) of both algorithms showed a correlative latitude dependency, with an increase in correlation for higher latitudes. This assessment highlighted the better performance of Q_{04} over G_{03} when compared with WW3, predominantly in high latitude ocean regions with full developed seas, where large wave period values were verified. For these reasons, the next section will mainly focus on Q_{04} as the chosen algorithm to estimate mean wave period for SSB model input for all the considered altimetric missions.

4.3.3 Direct SSB Estimations for all Reference Missions

For the reasons described in the previous section, knowing that SSB is instrument dependent, it is necessary to design a mission specific modeling approach by supervising the SSHA input dataset used as the first estimations, which in turn will train the SSB correction algorithm. To guarantee uniformity, only the missions A-phases were used, i.e. the periods when the satellites are in the so-called "reference orbit".

The 3-dimensional SSB estimation used as predictors for model design the following parameters: the altimeter-measured H_s, altimeter-derived U_{10} (computed from Ku-band sigma0 and Hs) and altimeter-derived Tz (computed from Ku-, C-bands σ_0 and H_s). Moreover, the residual sea surface height anomaly (SSHA) data, uncorrected for SSB, constitute the training dataset that will feed the response to be fitted by the selected model.

The residual SSHA have been computed by subtracting the altimeter-range measurements

from the orbital altitude with all required range, geophysical and instrumental corrections applied, and the mean SSH characterized by DTU15 mean sea surface (MSS). This procedure follows the direct technique proposed by [13] where sea surface height deviations from the marine geoid (here represented by the DTU15 MSS) are binned against altimeter U_{10} and H_s. In this way, a 2-parameter direct SSB estimation has been computed for each mission (TP, J1, J2 and J3) with a bin width of 0.25 m/s in U_{10} and 0.25 m in H_s, for bins containing at least 300 samples.

A bin pre-processing routine, following the procedure described in [14], has been applied, to quality-control the predictors and the SSHA that will feed the model input. According to [14], the median parameter of central tendency was chosen to measure SSHA deviations per bin, thus allowing lower discrepancies in the edges of the [H_s, U_{10}] space. A weighting procedure was also applied, associating bins sample number and standard deviation with increasing/decreasing ramp functions ($1 - e^{-x}$ and e^{-x}) based on natural exponential functions. Figure 4.2 shows SSHA bins estimations of the 4 reference missions (TP, J1, J2 and J3) obtained from the 2-parameters direct technique, after applying the described bin pre-processing routines. From the SSHA estimations showed in Figure 4.2, it is possible to obtain a preliminary appreciation of the SSB behavior over the (H_s, U_{10}) domain for the considered missions, thus giving a better knowledge of the variability between missions and of the suitability of each parameters for different model designs.

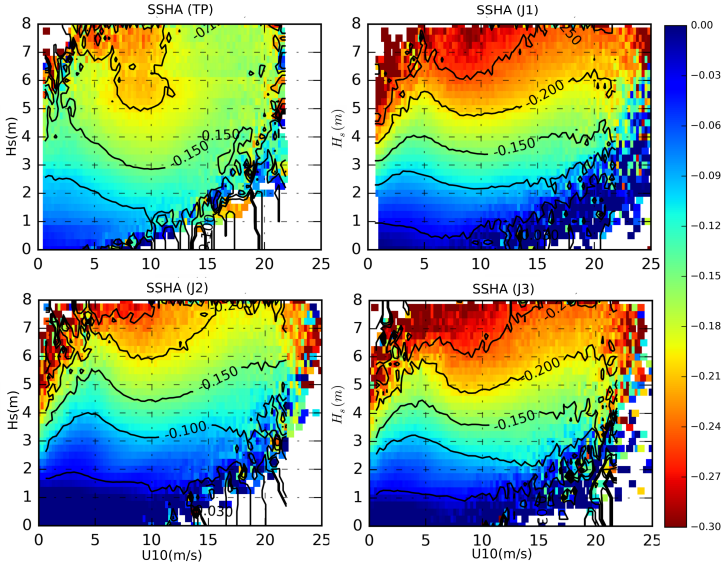

Figure 4.2: Direct method output of SSHA bins estimations, after pre-processing, for TOPEX (TP), Jason-1 (J1), Jason-2 (J2) and Jason-3 (J3).

4.3.4 Non-parametric Approach for SSB Estimation

Generally, the non-parametric (NP) SSB can be assumed as the relationship between a quantitative response Y and p different predictors, $x = (x_1, x_2, ...x_p)$, and can be written in the form of $Y = f(x) + \epsilon$ where $f(x)$ is the unknown NP SSB function of the different predictors to be estimated by relating x with the response variable Y, ϵ is a random error term comprising different error components (geophysical/instrumental corrections, interpolation errors, etc...) which is independent of x and has zero mean.

In this study, the predictors are H_s, U_{10} and T_z and the response Y is the sea surface height anomalies (SSHA) determined using the direct method. NP SSB will be formulated as a non-linear relation for estimating f, based on smoothing spline methods embedded in a general framework provided by a Generalized Additive Model (GAM) [40,41].

Smoothing splines result from minimizing a residual sum of squares (RSS), subject to a smoothness penalty in the form of *loss+penalty* where the term $RSS = \sum_{i=1}^{n}(y_i - g(x_i))^2$ is a loss function without constraints adjusted to an arbitrary $g(x_i)$ function in order to fit each observed predictor y_i well, and $\lambda \int g''(t)^2 dt$ is a penalty term that penalizes the variability in g to eliminate the possibility of overfitting. The tunning parameter λ controls the roughness of the smoothing spline, hence the effective degrees of freedom, and can be chosen based on data variability analysis, taking into account the function flexibility for over-fitting control, or by cross-validation techniques, by making RSS as small as possible for the available vector acting as predictor. In this case, the penalty term is a measure of the total change in the function $g'(t)$, over its entire range. If g is very smooth, then $g'(t)$ will be close to a constant and $\int g''(t)^2 dt$ will assume a small value. In the case of a large variability of g, the function will vary significantly and the integral will result in a large value. Therefore, the penalty term encourages g to be smooth. The larger the value of λ, the smoother g will be.

The SSB model was designed using a GAM statistical approach, allowing to produce a model with additive properties between non-linear functions expressed by smoothing splines of each variable, while maintaining additive properties. In this work, several different SSB modeling designs have been tested, $SSB_i = \beta_0 + \sum_{j=1}^{p} f_j(x_{ij}) + \epsilon_i$ with 2 and 3 predictors from $(x_{i1}, x_{i2}, x_{i3}) = (H_s, U_{10}, T_z)$, to evaluate the impact of the third predictor T_z in the final SSB response, and with different tuning parameters $\lambda = (4, 5, 6)$ for smoothness control without data overfitting.

4.4 SSB Model Design for Jason-2 mission

4.4.1 Model Sensitivity to Predictors and Smoothing Parameter

Jason-2 Phase-A was the chosen mission to perform a thorough assessment of the different SSB modeling design and its sensitivity to the training datasets. The mission phase-A lasted more than eight years, the period when the satellite was on the nominal reference orbit ground tracks, producing 303 cycles of altimeter data dedicated to ocean studies. Five SSB model designs have been tested for Jason-2 and compared with the established SSB models, CLS [16,19] and Tran [42] models. SSB_{cls} was originally generated from 100 cycles of TOPEX-A altimetric measurements obtained between 4 April 1993 and 15 April 1996, and then re-evaluated for Jason-1 and Jason-2 [43], while SSB_{tran} consists of two models generated from two different datasets: a model derived for Jason-1, adjusted with 111 cycles of the same mission, and a second model applied to Jason-2 and Jason-3 originally generated from ∼36 of the first three years of the Jason-2 mission. Both models are available in RADS for the entire J2 mission period, and the derived

outputs are computed in the form of a regular grid in a two-dimensional (H_s, U_{10}) domain. A simple empirical SSB model, using a first order predictor in the form of $-3.8\%H_s$, represents the low limit benchmark and will serve to assess the performance of different testing model designs, based on the number of used predictors (2- and 3-dimensions), the type of algorithm adopted for the mean wave period $T_z(G_{03}, Q_{04})$ and the smoothness parameter λ applied to each predictor. The following five configurations of the University of Porto SSB model, SSB_{upt}, have been tested:

1. $SSB1_{upt} = f_1(H_s) + f_2(U_{10})(\lambda = 5)$
2. $SSB2_{upt} = f_1(H_s) + f_2(U_{10}) + f_3(G_{03})(\lambda = 5)$
3. $SSB3_{upt} = f_1(H_s) + f_2(U_{10}) + f_3(Q_{04})(\lambda = 4)$
4. $SSB4_{upt} = f_1(H_s) + f_2(U_{10}) + f_3(Q_{04})(\lambda = 5)$
5. $SSB5_{upt} = f_1(H_s) + f_2(U_{10}) + f_3(Q_{04})(\lambda = 6)$

The model selection is based on predictive accuracy, estimated with *Akaike Information Criterion* (AIC), *adjusted*–R^2, to measure the goodness-of-fit and identifying the percentage of variance in the target field that is explained by the input, and cross-validation techniques consisting on reserving a particular sample of a data set for model training [40]. To cross validate the different model designs, the dataset of 303 J2 cycles has been divided into training and testing sets, quantifying the average of the square deviations from mean square errors (MSE). In addition, the impact on SSB estimation of the size of the available dataset was also examined.

Since SSB is a correction derived empirically from data, its computation is done according to the data available at a given moment and should be repeated regularly during the lifespan of the mission, as more observations are available.

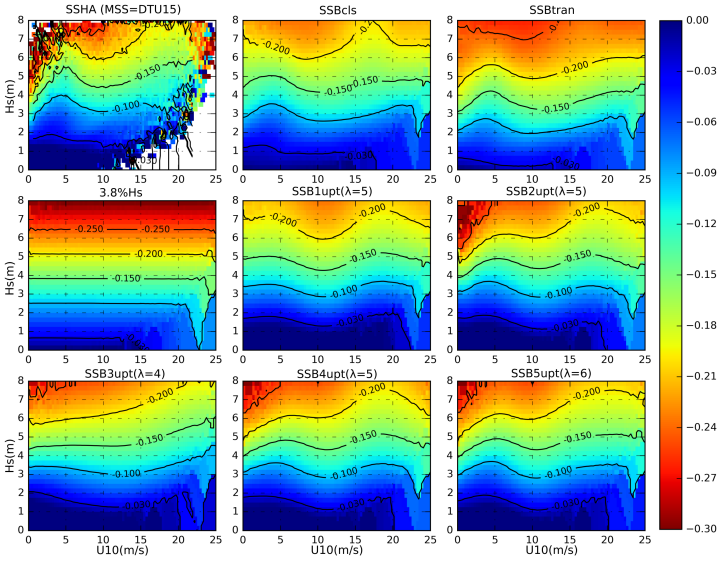

Figure 4.3: SSB predictions (in meters) for a test dataset (cycle 80-150), result of fitting the models for a training dataset with the first 120 cycles of Jason-2 over the (H_s, U_{10}) domain. From left to right, up to down: direct output of the bin-medianed SSHA uncorrected for SSB; SSB_{cls} correction for the test dataset; SSB_{tran} correction; first order predictor acting as the low limit benchmark in the form of $-3.8\%H_s$; $SSB1_{upt}$ computed with 2 predictors (H_s, U_{10}) and a tunning parameter $\lambda = 5$; $SSB2_{upt}$ with (H_s, U_{10}, G_{03}) and $\lambda = 5$; $SSB4_{upt}$ with (H_s, U_{10}, Q_{04}) and $\lambda = 5$; $SSB3_{upt}$ with (H_s, U_{10}, Q_{04}) and $\lambda = 4$; $SSB5_{upt}$ with (H_s, U_{10}, Q_{04}) and $\lambda = 6$.

For recent missions, as in the case of J3, there is a need to derive an SSB correction rapidly with little available data, but reliable enough to be quickly applied to the altimetric range. To cross validate the proposed models and assess the accuracy of SSB predictions computed for the entire mission, training datasets with different lengths (for the first 10, 20, 50 and 120 cycles) were tested to fit the proposed five configurations. For a training dataset of 120 cycles, corresponding approximately to the first 3 years of observations of the J2 mission (between July 12, 2008 and October 14, 2011), the SSHA has been computed with the direct technique in order to produce SSB estimations with the five proposed model designs. Figure 4.3 shows the output of each model configuration for a test dataset of 70 cycles (between cycle 80 and 150), side-by-side with the established models SSB_{cls} and SSB_{tran}.

The bin-medianed SSHA estimations of sea height residuals, submitted to the pre-processing routines of minimum sample limits, weighting procedures and diagnostic tests, produced an initial response vector with n=1934 bins. A method to identify and eliminate existing outliers, based on a 2σ rejection criterion (residuals larger than 2σ are eliminated) decreased n to 1839, leading to a sample reduction of 5%. Some noise on the fringes of SSHA is observed for ocean swell regions (high H_s, low U_{10}), which is expected for this SSB estimation technique. The sensitivity of the SSB_{upt} in medium-low H_s and U_{10} conditions is well in line with SSB_{cls} and SSB_{tran} models, clearly demonstrating a good agreement of SSHA with both models in these ocean domain regions. The low limit benchmark of $-3.8\%H_s$ seems to produce some overestimation, but will serve as an indicator for SSB model performance, based on the variance reduction of sea level anomalies as explained in the next section.

Figure 4.3 also shows the outcome of the University of Porto (UPT) SSB models for the five proposed designs $SSS[1\text{-}5]_{upt}$. Several conclusions can be drawn from the comparison between the various UPT models and the SSB_{cls} and SSB_{tran} models. The use of a third predictor as represented by the mean wave period T_z adds more information to the model compared to the equivalent two-parameter model ($SSB1_{upt}$). It produces better response fittings, especially over the low U_{10} domain, where a bunching-up of contour lines for SSB values seen between -0.10 m and -0.20 m, reproducing well the greater sensitivity of the predicted SSB variability in this region.

The use of Q_{04} T_z leads to a slightly better performance than G_{03}, especially for ocean regions with high H_s, where it is less affected by the noisy values of SSHA, and produces a better controlled model in these domains. These differences may be related to the fact that G_{03} was developed for TP Ku-band, and Q_{04} for TP and J1. By applying these approaches to J2 and J3, a small error may be introduced, since the (H_s, U_{10}) variations for this satellite may differ from those used in the computation of the T_z models. The model design using 3 predictors and a tuning parameter $\lambda = 4$ produces excessive smoothness, being less sensitive to SSB variations for the whole domain. The models with $\lambda = 5$ and 6 produce similar outputs, suggesting that above 5 there is no need to increase the model degrees of freedom.

Table 4.1 summarizes, for the considered test dataset, the output statistics of each SSB_{upt} model design, the standard CLS and Tran models and the $-3.8\%H_s$ uni-dimensional benchmark.

Table 4.1: Summary statistics of the SSB resulting from the various fitting models for a test dataset of 70 cycles of J2 (cycle 80-150) trained with the first 120 cycles (cm).

	mean	σ	**min**	**max**
-3.8%H_s	-10.03	4.80	-30.40	0.00
SSB_{cls}	-08.33	4.34	-23.74	0.32
SSB_{tran}	-10.89	4.56	-26.37	0.02
$SSB1_{upt}$	-06.71	5.31	-23.57	0.07
$SSB2_{upt}$	-06.58	5.35	-33.53	0.11
$SSB3_{upt}$	-06.76	5.16	-29.10	0.14
$SSB4_{upt}$	-06.64	5.30	-31.43	0.10
$SSB5_{upt}$	-06.61	5.37	-30.86	0.10

The comparison with the CLS and Tran models shows that $SSB[1\text{-}5]_{upt}$ predict lower statistical mean SSB but larger standard deviations. This model elasticity is associated with the direct method of SSHA estimations, which preserves more sea-state information compared with e.g. the crossover method, given that higher resolution can be achieved due to smaller bin sizes of input sea height residuals. The assessment of the 5 model designs in Table 4.1 makes it possible to choose $SSB4_{upt}$ as the one to use for the subsequent analyses, which consider the impact of fitting training datasets with fewer observations. The ability to design an SSB model capable of producing reliable estimates with little input data (small training data sets), is of great interest to satellite altimetry, where it is important to make the SSB corrections available to users as quickly as possible, after new missions are launched. For this purpose, $SSB4_{upt}$, from now onwards just referred as SSB_{upt} or simply UPT-model , has been fitted with different size training datasets, i.e. SSHA estimations with the first 50, 20 and 10 cycles of Jason-2.

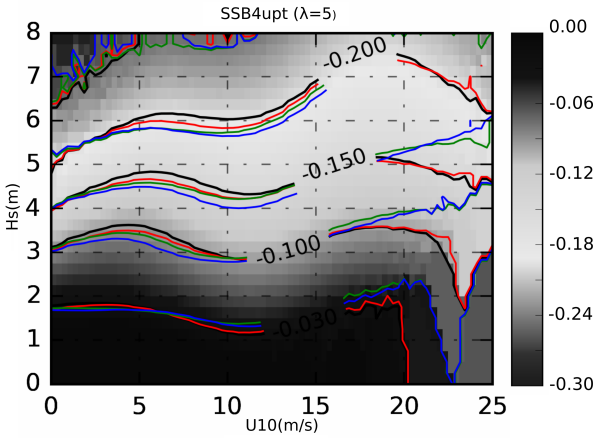

Figure 4.4: $SSB4_{upt}$ (in m) for a test dataset (cycle 80-150) produced from different training datasets. Contour line colors represent (in cycles): t=120 (black), t=50 (red), t=20 (green), t=10 (blue).

Figure 4.4 on page 59 shows the SSB output obtained for the same test dataset of 70 cycles (from cycle 80-150) resulting from fitting $SSB4_{upt}$ with different size training datasets. From this figure, a small increase in the magnitude of the SSB can be observed, as the model input

data is reduced. Apart from that, the reduced-size models show good performance in retaining information about the nonlinear relationships between predictors, giving confidence in their ability to produce a coherent set of SSB values for future test datasets.

Table 4.2: Summary statistics of the SSB predictions for a test dataset of 70 cycles of Jason-2 (cycle 80-150) from models trained with different datasets of 50, 20 and 10 cycles (cm).

	mean	σ	**min**	**max**
$SSB4_{upt}$ (train 50)	-6.77	5.39	-30.06	0.09
$SSB4_{upt}$ (train 20)	-6.84	5.51	-29.54	0.12
$SSB4_{upt}$ (train 10)	-7.07	5.70	-28.51	0.08

Table 4.2 shows a slight increase in the magnitude of the statistical mean SSB and of the standard deviation σ when less information is available for model training, but even with 20 cycles of observations, corresponding approximately to 7 months of data, is still possible to obtain a reliable and controlled SSB model. The results for 10 cycles used as a training dataset, suggests that it is also possible to establish an approximate correction for the most of the cases, but some instability is verified, especially in those cases where the correction variability increases.

Figure 4.5 shows a global overview of the mean SSB values in lat-lon squares of $4° \times 4°$ for the SSB_{upt} model trained with 120 cycles and predicted for all observations of Jason-2 Phase A mission. When applied to J2 observations, SSB_{upt} shows high SSB values up to -0.16 m in the Southern Ocean, which is dominated by persistent westerly winds and high sea states with long fully-developed wind seas. The use of a third predictor T_z is extremely important in these regions where the SSB correction has a large impact on altimeter SSH data.

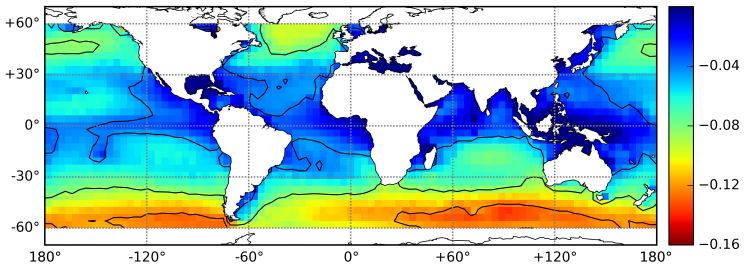

Figure 4.5: Mean values (in m) of the J2 SSB_{upt} predictions produced from a training dataset with 120 cycles.

4.4.2 Jason-2 SLA Analysis

One of the metrics used to measure the accuracy of SSB estimates is the sea level anomaly variance explained by the correction when applied globally. It is known that a strong correlation exists between the SSB and the oceanic variability, due to the inherent dependence of the correction on sea-state descriptors responsible for the variability.

In SSB studies, since no ground truth exists for validation purposes, it is common practice to perform SLA variance analysis. Next, various statistical analyses of the sea level anomaly ($SLA = SSH - MSS$) are performed using the SSH corrected for all instrumental, range and

geophysical effects, but using different SSB corrections. A spatial statistic assessment metric, the SLA scaled variance difference index (SVDI), was estimated from the scaled difference of SLA variances, computed along collinear tracks, further divided by the variance, based on their time of passage at the Equator:

$$SVDI(\%) = \frac{\sigma^2(SLA_1) - \sigma^2(SLA_2)}{\sigma^2(SLA_1)} \times 100 \tag{4.3}$$

For this SLA scaled analysis, the reference SLA_1 dataset was computed using SSB_{upt}. This SLA_1 dataset was then compared with other 3 SLA datasets (SLA_2) computed with different SSB models ($-3.8\%Hs$, SSB_{cls}, SSB_{tran}). When comparing the performance of two different SSB corrections, the produced scaled SLA variance differences are shown in relative percentages. In this way, a reduction in the scaled SLA variance is an indicator of a model improvement.

Figure 4.6 shows the SSB_{upt} performance in terms of SVDI variance differences, when compared with the low limit benchmark of $-3.8\%Hs$, SSB_{cls} and SSB_{tran}. Regarding the first one, SSB_{upt} shows a significant improvement, reaching the 10% of SLA variance reduction for some regions in the Pacific and Atlantic oceans (dark blue). These results were expected due to the two additional sea-state predictors used by the SSB_{upt} model, but serves as a first indicator when analyzing the distinct performances of different SSB models. When compared with SSB_{cls} and SSB_{tran}, SSB_{upt} achieves similar results, except in some regions in the north of Indian Ocean and the Indonesian through flow (dark red) where SLA SVDI reaches up to +/- 15%. The intriguing performance of SSB_{upt} in these areas, where simultaneously better and worst performances of SSB_{upt} are verified, could be explained by large oceanic variability causing modeling adapting difficulties and requires further

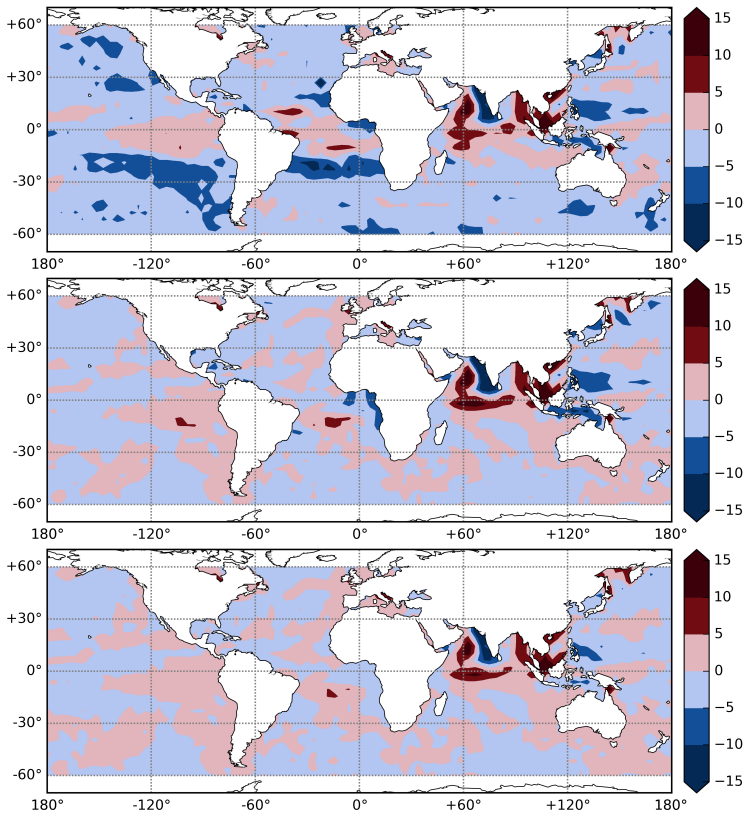

Figure 4.6: SLA scaled variance difference index (SLA SVDI) in % for three SLAs computed with different SSB models: (top) $-3.8\%Hs$, (middle) SSB_{cls}, and (bottom) SSB_{tran}, estimated for all observations in Jason-2 Phase A and with SLA_1 computed from SSB_{upt} trained with 120 cycles. (lat-lon squares of 4°).

attention. As described in the next section, these results are not confirmed for TP, J1 and J3, where SSB_{upt} performance is in line with the standard SSB models for these regions, in which values between -5% and 5%, can be considered residual and meaningless in what concerns the differences between models under comparison. Figure 4.7 on page 62 extends the SVDI comparative analysis for variance differences between SSB_{upt} fitted with 3 different SSHA training datasets for the first 50, 20 and 10 cycles of J2 and SSB_{tran}.

Figure 4.7 shows that similar performances are achieved when SSB_{upt} is fitted with training datasets of 50 cycles rather than 120 cycles (Fig 4.6). But, as expected, decreasing the information used for training, means the model becomes more unstable, resulting in an increase of SLA variances in some equatorial regions. Statistical results from tables 4.1 and 4.2 reinforce this conclusion with low discrepancies on central tendencies and low amount of estimated variation between both models. With a training dataset of only 20 cycles, SSB_{upt} model can still produce reliable corrections for the entire mission.

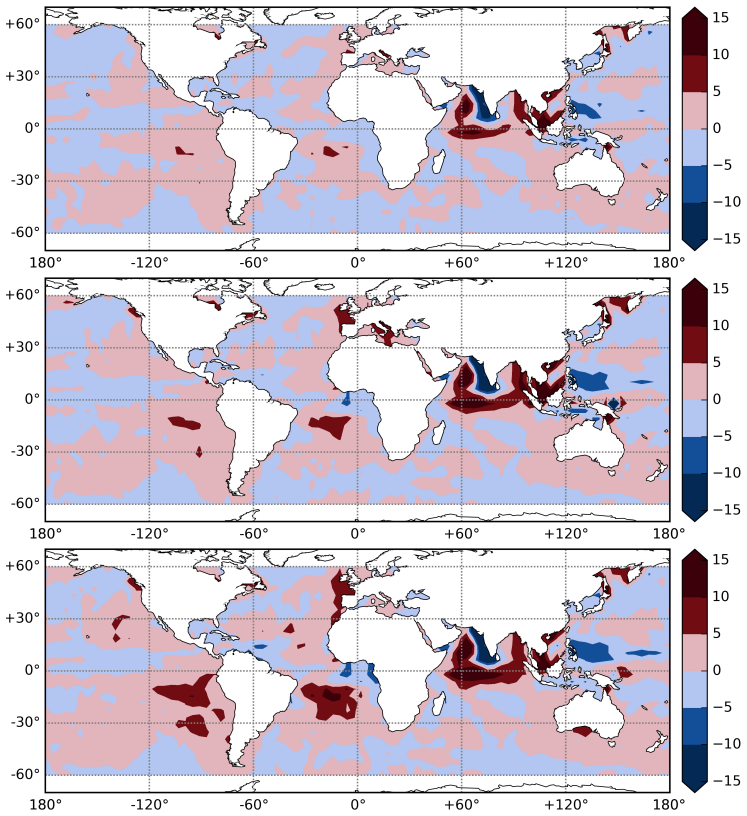

Figure 4.7: SLAscaled variance differences (in %) for all J2 Phase A observations, between SLA computed with SSB_{upt} for different training datasets with 50 (top), 20 (middle) and 10 cycles (bottom) and SSB_{tran}.

In order to better understand the performance of the various models on a temporal scale, SLA_{scaled} have been computed with all proposed SSB models for each cycle of the J2 mission to examine its temporal evolution (Fig 4.8 on page 63). Each model is evaluated through variance differences from the low limit benchmark $-3.8\%Hs$, which in this case assumes the role of ground reference opposed to each SSB model. Figure 4.8 confirms the previous results, with similar performances achieved for training datasets of 120 and 50 cycles. Both models reduce the SLA variance for almost the entire mission, reaching a variance reduction of more than 2.0% in some periods. The model consistency is verified by the comparable behavior it displays with respect to SSB_{tran} and the clear improvement with respect to SSB_{cls}. The best performances revealed by SSB_{tran} and SSB_{upt} models when compared to the SSB_{cls} may be explained by different reasons, the fact that SSB_{tran} is using predictors fitted with a different retracker algorithm (MLE4) and is modeled with a dataset covering 36 cycles divided

over a period of 3 years, while SSB_{upt}, using a 3-dimensional approach, is adding more sea-state information from the third predictor, T_z. Figure 4.8 also reveals some inconsistencies when less information is given to train SSB_{upt}, where some instabilities appear in some cycles. In spite of that, a model fitted with SSHA estimations from the mission first 20 cycles can still predict a reliable and relatively stable SSB model for a long distance period of observations, in this case, the entire J2 mission.

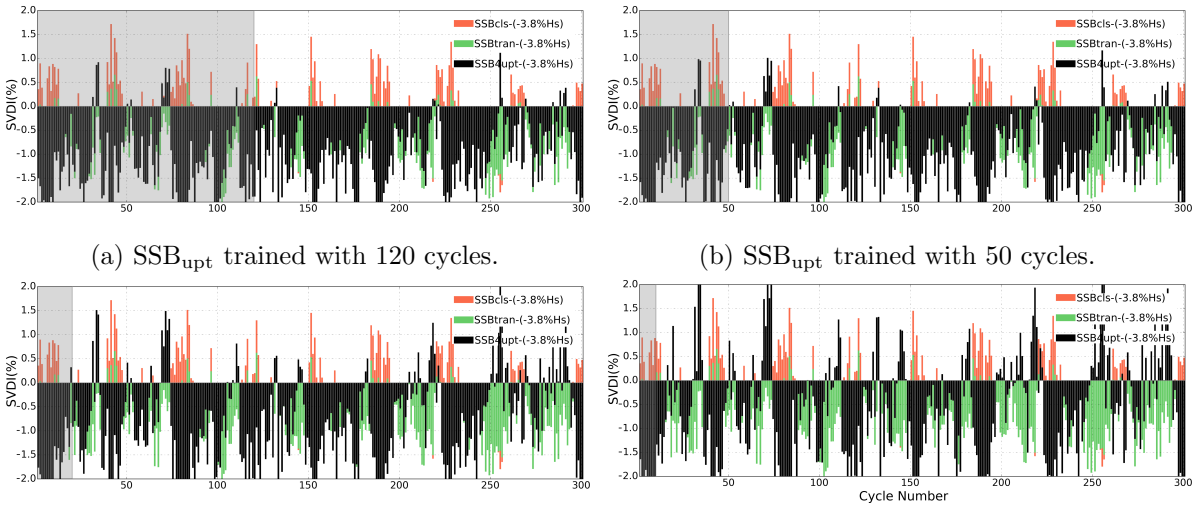

(a) SSB_{upt} trained with 120 cycles.

(b) SSB_{upt} trained with 50 cycles.

(c) SSB_{upt} trained with 20 cycles.

(d) SSB_{upt} trained with 10 cycles.

Figure 4.8: Temporal evolution of SLA_{scaled} (SVDI) variance differences for all SSB models (red: SSB_{cls}, green: SSB_{tran} and black: SSB_{upt}) against the unidimensional benchmark of $-3.8\%Hs$. Grey areas represent the number of cycles used to train SSB_{upt} starting with 120 cycles (from top left) and ending with 10 cycles (bottom right). Note: Y axis has been saturated at 2% and -2%, as very few values are outside these limits.

Figure 4.9 illustrates the absolute SLA variances computed for each SSB model, giving an overview of the reduction of the explained variance over the full J2 mission. The figure shows that the smallest SLA variances are achieved with the SSB_{upt} models trained with 120 and 50 cycles, for which a SLA reduction of 1.1 cm^2 relative to the unidimensional SSB is reached. As expected from the previous analyses, the variance increases with shorter training datasets. It can also be observed that the SLA variance for a model trained with only 20 cycles, is comparable in performance with the variance obtained with SSB_{tran}. This suggests that it is possible to develop a SSB model with a reduced amount of altimeter data, from a continuous period such as the first cycles of a mission, being of direct application in the most recent missions. The case cor-

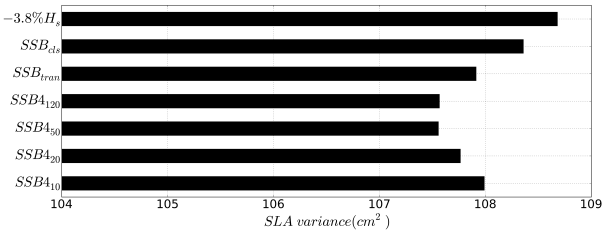

Figure 4.9: Absolute SLA variance (cm^2) when computed for each SSB model (SSB_{cls}, SSB_{tran} and for training datasets of 120, 50, 20 and 10 cycles respectively fitted in SSB_{upt}).

responding to the model trained with only 10 cycles leads to a slight increase in variance of 0.1 cm^2 with respect to the Tran model, but still better than the 2-parameter CLS model.

4.5 SSB UPT for all Reference Missions

From the assessment of the different model configurations made on previous section, it was concluded that the design adopted in SSB_{upt}, trained with 50 cycles, reaches the best compromise between accuracy of predictions and computation time. This model design is able to capture most of the SSHA signal estimated from the direct technique, retrieving a reliable SSB correction at spatial and temporal scales.

Aiming to extend this approach to all reference altimeter missions, (TOPEX, Jason-1 and Jason-3), SSB_{upt} models have been derived for these missions using the same methodological principles and SLA metrics for performance evaluation as done for J2 in the previous section.

4.5.1 TOPEX-A and -B Instruments

During the phase A of the TOPEX mission, the satellite operated with two different altimeters: TOPEX-A (TP-A) from cycles 1-235 and TOPEX-B (TP-B) from cycles 236-364. Due to the instrument dependency of the SSB correction, it was necessary to train one SSB model for each of the two mission periods corresponding to the different instruments. Therefore, the SSB_{upt} model for TP was trained with two datasets, each with 50 cycles of data: cycles 1-50 for TP-A and cycles 236-286 for TP-B, thus producing two different models for each instrument.

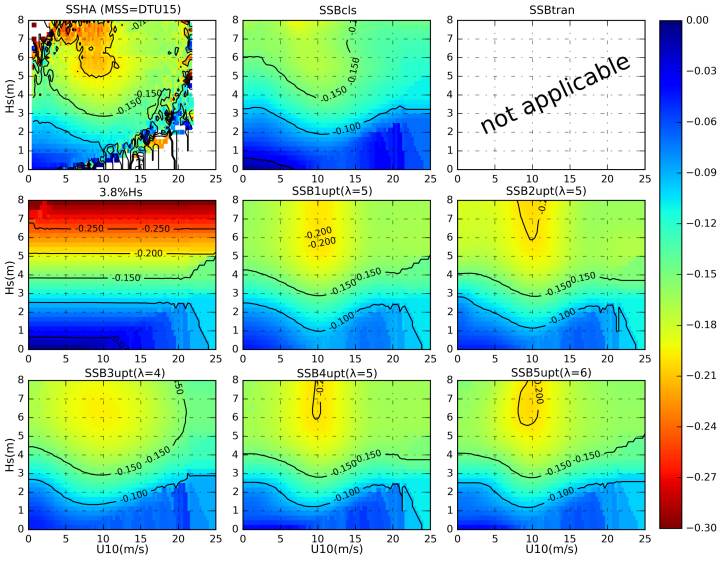

Figure 4.10: TOPEX-A SSB predictions for a test dataset (cycle 80-150) with a fitting training dataset of the mission first 50 cycles over the (H_s,U_{10}) domain. The plots displaying order follows the same of figure 4.3 on page 57. Note that SSB_{tran} is not available for TOPEX mission.

Figure 4.10 shows the SSB predictions obtained with all model designs discussed in section 3, when applied to a test dataset of 70 cycles (80-150) of TP-A. Figure 4.10 and table 4.3 show that SSB_{upt} performs well in retrieving the SSHA signal by modeling higher SSB corrections for U_{10}< 12 m/s and H_s>4 m, producing a measure of central tendency greater than SSB_{cls} and less amount of variation over the considered domain. Similar performance were obtained for SSB_{upt} developed for TP-B (not shown).

Table 4.3: Summary statistics of the different SSB models approaches for a test dataset with 70 cycles of TX-A (cycle 80-150) (cm).

	mean	σ	**min**	**max**
-3.8%H_s	-10.05	4.87	-30.40	0.00
SSB_{cls}	-09.97	3.37	-19.70	0.00
SSB_{upt}	-12.28	3.56	-20.31	-0.02

Figure 4.11 on page 65 shows the global overview of SSB_{upt} for TP-A, trained with the first 50 cycles of TP-A (left panel) and the corresponding model for TP-B (right panel), when each model is applied to the full datasets retrieved by each instrument.

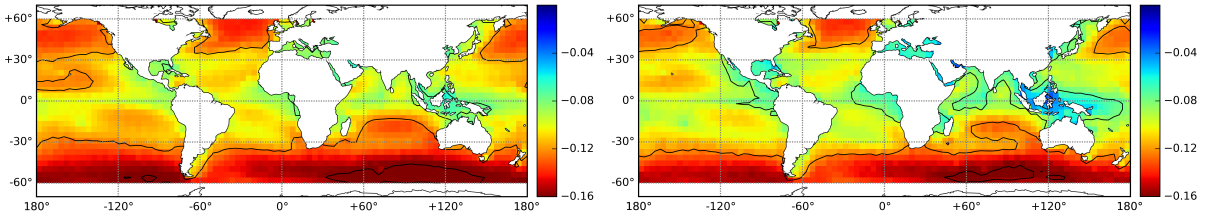

Figure 4.11: Global overview of the mean values of SSB_{upt} for the full TP-A (left) and TP-B (right) periods during Phase A, with SSB_{upt} produced from two training datasets corresponding to the first 50 cycles retrieved by each instrument (in meters).

The evaluation made by SVDI analysis against SSB_{cls} in Figure 4.12 shows that SSB_{upt} is consistent with SSB_{cls}, with pointwise enhancements in some regions close to land. Figure 4.13a on page 66 illustrates this slight improvement of SSB_{upt} relative to SSB_{cls} at temporal scales. The absolute SLA variances computed for each SSB model show a strong variance reduction when compared to the low limit benchmark of $-3.8\%Hs$, emphasizing that both models (SSB_{cls} and SSB_{upt}) are capable of producing reliable SSB corrections. Moreover, figure 4.13b on page 66 shows that SSB_{upt} reduces the SLA variance relative to SSB_{cls} by a further 0.5 cm^2, mostly due to a better performance in some regions near land. Note that for TOPEX, no SSB_{tran} model is available for comparison.

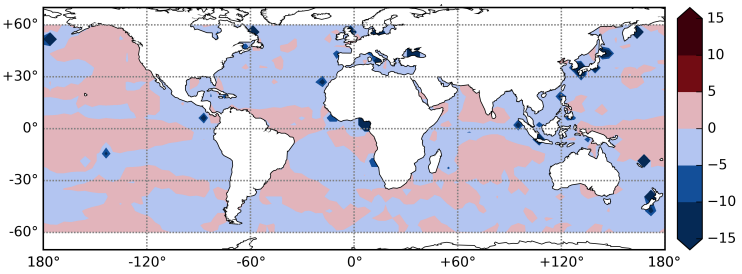

Figure 4.12: Collinear analysis of SLA_{scaled} variance differences, for all observations of TOPEX Phase A mission, between SLA computed from SSB_{upt} trained with 50 cycles of each TOPEX instrument, and SLA computed from SSB_{cls}.

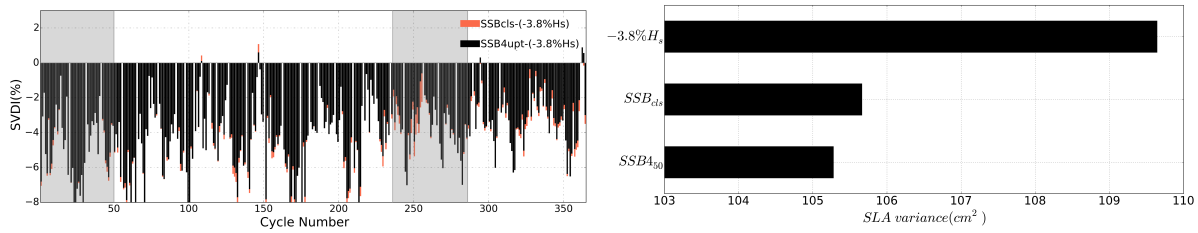

(a) Temporal evolution of SLA_{scaled} variance differences for SSB_{cls} and SSB_{upt} opposed to the unidimensional benchmark of -3.8%H_s.

(b) TOPEX absolute SLA variance (cm^2) when computed for each SSB model (SSB_{cls} and SSB_{upt}) trained with 50 cycles of each instrument.

Figure 4.13: Temporal evolution and absolute TOPEX SLA variances computed for each SSB model. On left plot, grey areas represent different periods of TP-A and TP-B used to train SSB_{upt} model. Note: Y axis has been saturated at 2% and -2%, as very few values are outside these limits.

4.5.2 Jason-1 Mission

Jason-1 Phase A produced 260 cycles of altimeter measurements and was the mission used in [14] to establish the first empirical formulation of an SSB model based on information retrieved entirely from altimetric data. Following the same methodological approach as described above, SSB_{upt} has been trained with the mission first 50 cycles and predictions for a test dataset of 70 cycles (80-150) have been computed. Figure 4.14 shows the SSB predictions produced by the different model configurations where it is possible to observe some noise in the fringes of SSHA for ocean swell regions (high H_s and low U_{10}) and young seas regions (low H_s and high U_{10}), but smoothed by the final $SSB4_{upt}$ model. Table 4.4 on page 67 describes the statistics of all SSB models for the test dataset. Consistency of SSB_{upt} is verified across the whole data span, with close measures of central tendency and data variability between models when compared with SSHA output. Comparing with the results presented in [14], it is possible to observe that both $SSB2_{upt}$ (with G_{03}) and $SSB4_{upt}$ (with Q_{04}) perform well on capturing the strong SSB gradient seen at low winds, but $SSB4_{upt}$ shows less shrinkage on these regions, similar with the

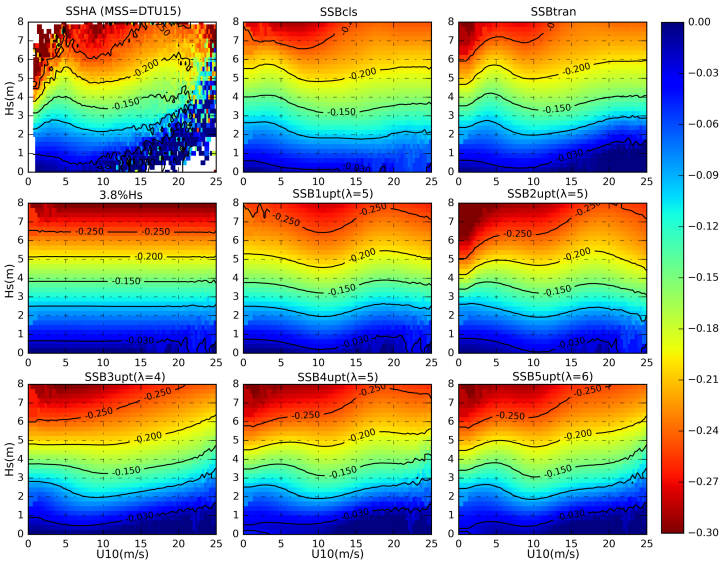

Figure 4.14: Jason-1 SSB predictions (in meters) for a test dataset (cycle 80-150) with a fitting training dataset of mission first 50 cycles over the (H_s, U_{10}) domain. The plots displaying order follows the same of figure 4.3 on page 57.

standard models behavior. Considering the previous results for TP and J2 SSHA outputs, it is also possible to verify a peak around 5 m/s in U_{10} retrieved by the 3-dimensional designs, but not captured by any of the 2-parameter models.

Table 4.4: Summary statistics of the different SSB models for a test dataset with 70 cycles of J1 (cycle 80-150) (cm).

	mean	σ	**min**	**max**
-3.8%H_s	-09.85	4.90	-30.40	0.00
SSB_{cls}	-11.05	4.68	-29.20	-0.41
SSB_{tran}	-10.60	4.61	-29.88	3.74
$SSB4_{upt}$	-10.80	5.05	-31.02	-0.16

Figure 4.15 shows the mean SSB_{upt} values, in meters, for the entire J1 mission, trained with the first 50 cycles of data. SVDI analysis against SSB_{tran} in Figure 4.16 confirms the SSB_{upt} stability when applied to J1. The results allow to conclude that both models perform closely for all sea-state regimes, not exceeding 5% of variance differences.

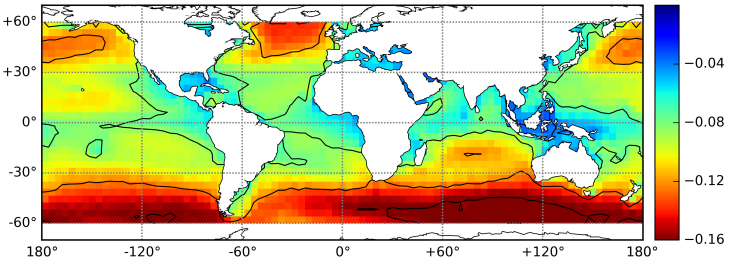

Figure 4.15: Mean values of SSB_{upt} predictions, in meters, for the whole J1 mission, fitted with a training dataset from the first 50 cycles of data.

However, from the temporal evolution of the SVDI in figure 4.17a of page 68 it is possible to observe that, in some cycles , SSB_{cls} and SSB_{tran} produce an increase of SLA variance when opposed to the low limit benchmark of $-3.8\%Hs$, while the same is not true for SSB_{upt}, thus showing an improved stability in predicting corrections for the entire mission.

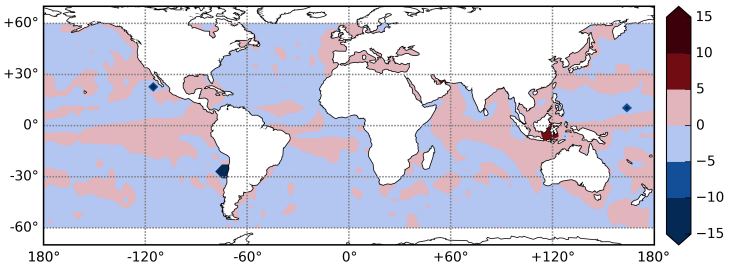

Figure 4.16: Collinear analysis of SLA_{scaled} variance differences for all observations of J1 Phase A mission, between SLA computed from SSB_{upt} trained with 50 cycles and SLA computed from SSB_{tran}.

Overall, the absolute SLA variances computed for each SSB model show similar values for all SSB models. A slight improvement of 0.1 % can be noted for SSB_{upt}, but negligible when considering all mission observations (Figure 4.17b on page 68). It should be recalled that SSB_{upt} has been trained with a continuous set of 50 cycles while SSB_{tran} model has been trained with ∼36 cycles but spanning 3 different years, while the solutions from SSB_{cls} are based on data from the first 111 cycles [43].

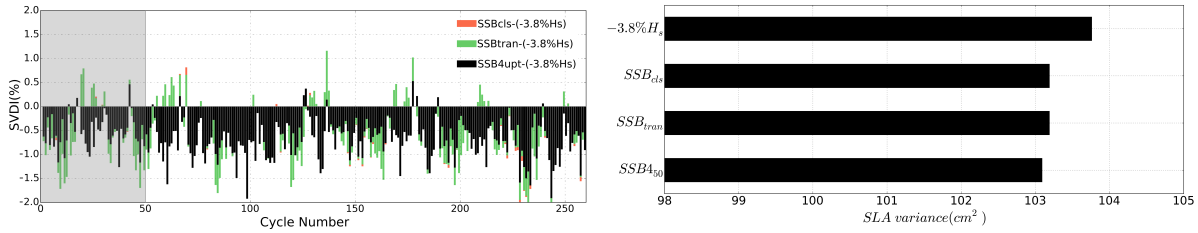

(a) Temporal evolution of SLA_{scaled} variance differences for SSB_{cls}, SSB_{tran} and SSB_{upt} opposed to the unidimensional benchmark of -3.8%H_s.

(b) Absolute SLA variance (cm^2) when computed for each SSB model (SSB_{cls}, SSB_{tran} and SSB_{upt}) trained with 50 cycles) over the full J1 mission.

Figure 4.17: Temporal evolution and absolute Jason-1 SLA variances computed for each SSB model. On left plot, grey area represents the used period to train SSB_{upt} model.

4.5.3 Jason-3 Mission

The assessment made for Jason-2 in section 4.4.2 (page 60) made it possible to conclude that SSB_{upt} can provide reliable predictions from a training dataset of only 20 cycles. At the time of this study, the RADS database had available only the first 40 cycles of the J3 mission, so that SSB corrections were developed using the first 20 cycles for SSB_{upt} fitting. Figure 4.18 shows the predicted SSB for the different model designs.

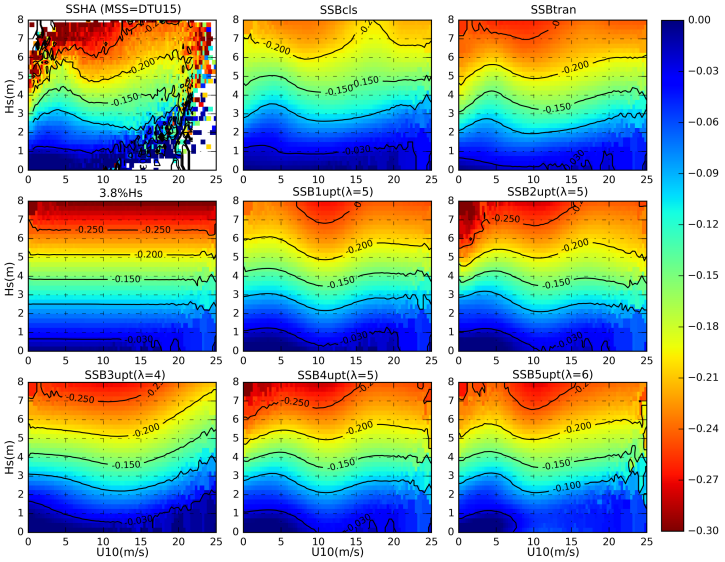

Figure 4.18: Jason-3 SSB predictions with a fitting training dataset of the mission first 20 cycles over the (H_s, U_{10}) domain. The plots displaying order follows the same of figure 4.3 on page 57.

Table 4.5 describes the statistics for the SSB_{upt}, SSB_{cls} and SSB_{tran} models when applied to the full J3 test dataset. It can be observed that, as it happened for the previous missions, SSB_{upt} is consistent with the established models, producing a reliable SSB model with a short training dataset. Figure 4.19 on page 69 illustrates the mean values, in meters, of SSB_{upt} computed for the 40 Jason-3 cycles available in this study.

Table 4.5: Summary statistics of the different SSB models for a test dataset with first 20 cycles of J3 (cm).

	mean	σ	**min**	**max**
-3.8%H_s	-10.07	5.23	-30.40	0.00
SSB_{cls}	-08.30	4.66	-23.73	1.43
SSB_{tran}	-10.85	4.90	-26.36	0.00
$SSB4_{upt}$	-09.35	5.65	-32.25	1.02

Comparing SVDI between SSB_{upt} and SSB_{tran}, it is possible to observe some improvements in a few Pacific Ocean regions where SSB_{upt} reduces the SLA variance by approximately 5% compared to SSB_{tran}. Figure 4.21a emphasizes these results when the assessment considers the temporal evolution of the SLA variance difference.

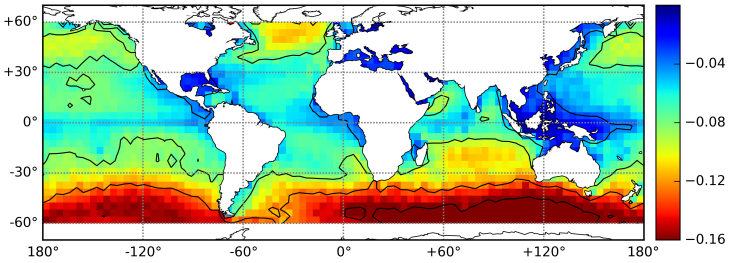

Figure 4.19: Mean values (in meters) of SSB_{upt} for the full J3 mission, fitted with a training dataset spanning the first 20 J3 cycles.

Relative to the low limit benchmark of $-3.8\%Hs$, SSB_{cls} is the model with the worst performance, increasing the SLA variance for some cycles by up to 1%. In contrast, SSB_{tran} and SSB_{upt} achieve similar results for the whole analyzed period. In figure 4.21b on page 70, the absolute SLA variances of the SSB models computed over the whole dataset confirm the previous results. The figure shows that SSB_{upt} reduces the global SLA variance by about 0.3% and 0.7% relative to SSB_{tran} and SSB_{cls} respectively, showing the possibility to design a stable SSB model for newly-launched altimeter missions, even when few data are available.

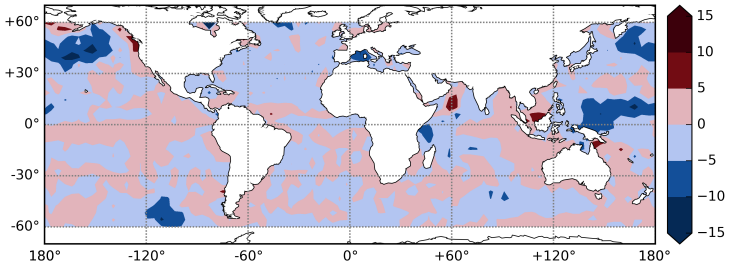

Figure 4.20: Collinear analysis of SLA_{scaled} variance differences from all observations of Jason-3 mission, between SLA computed from SSB_{upt} trained with 20 cycles, and SLA computed from SSB_{tran}.

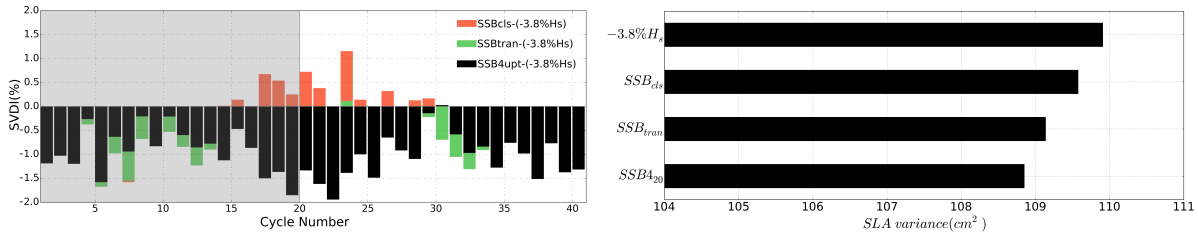

(a) Temporal evolution of SLA_{scaled} variance differences for SSB_{cls}, SSB_{tran} and SSB_{upt} opposed to the unidimensional benchmark of -3.8%H_s for J3.

(b) Jason-3 absolute SLA variance (cm^2) when computed for each SSB model (SSB_{cls}, SSB_{tran} and SSB_{upt}).

Figure 4.21: Temporal evolution and absolute Jason-3 SLA variances computed for each SSB model. On left plot, grey area represents the used period to train SSB_{upt} model.

4.6 Tandem Phases SSB Analysis

TOPEX/Poseidon was launched in August 1992 in the so-called reference orbit, and was successively replaced by Jason-1 (from December 2001), OSTM/Jason-2 (from June 2008) and Jason-3 (from January 2016). When a new satellite is launched, it begins the cross-calibration phase during which it shares the same reference orbit with the previous mission for approximately 200 days (∼20 cycles). This stage is called the tandem phase, where both satellites are on the same track, separated by ∼70 seconds, collecting data in the same ocean conditions. During these periods it is possible to inter-calibrate the instruments of the new mission with respect to the old ones. At the end of this phase, the older instrument is shifted to a new interleaved orbit, with tracks located midway of the reference ground tracks. Due to the short time separation between the two missions in the tandem phases, it is assumed that they sense the same sea-state conditions. Thus, in the absence of measurement errors, it can be assumed that the same SSH should be measured by both sensors.

Since the SSB correction comprises geophysical and instrumental effects, the analysis of the data in the tandem phases gives an opportunity to discard geophysical effects (e.g. the electromagnetic bias), strictly dependent on sea state, to allow a better characterization of the skewness+tracker bias contributions for the correction.

Three tandem phases were considered in this study: T1 (TP/J1) matching TP cycles 344-364 with J1 001-021, T2(J1/J2) matching J1 240-260 with J2 001-021, and T3 (J2/J3) matching J2 281-301 with J3 001-021. For each tandem phase, a spatial statistical assessment has been performed for SSB_{cls}, SSB_{tran} and SSB_{upt} computed along collinear tracks based on their time with respect to passage at the Equator.
Figures 4.22, 4.23 and 4.24 show the global distribution of the mean differences in SSB between two successive instruments in T1, T2 and T3 respectively for various SSB models.

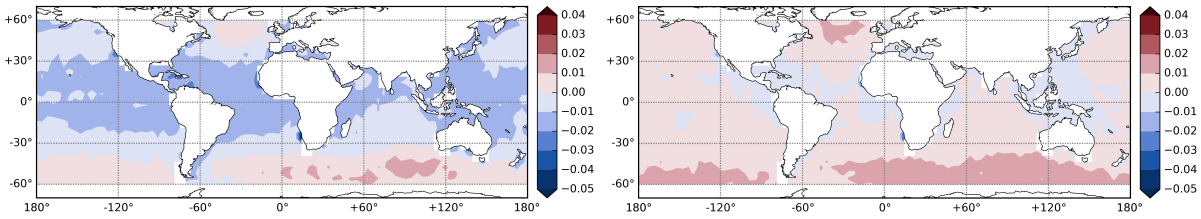

Figure 4.22: T1 (TP/J1): Collinear mean SSB differences between TOPEX and Jason-1 during the TP/J1 tandem phase for SSB_{upt} (left) and SSB_{cls} (right) (units: m).

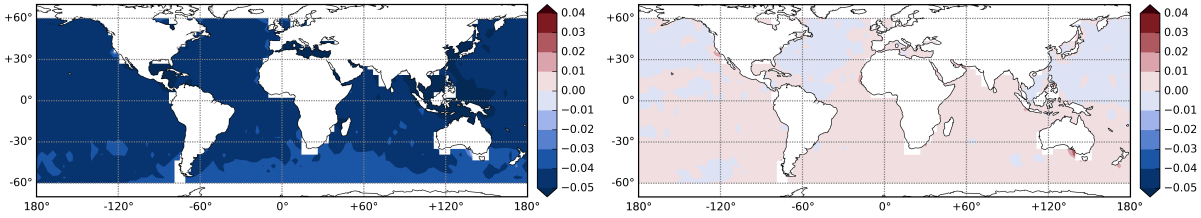

Figure 4.23: T2 (J1/J2): Collinear mean differences between Jason-1 and Jason-2 SSB during the J1/J2 tandem phase for SSB_{upt} (left) and SSB_{tran} (right) (units: m).

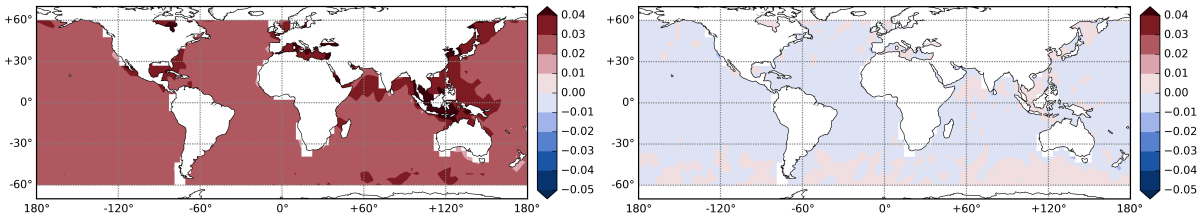

Figure 4.24: T3 (J2/J3): Collinear mean differences of SSB_{upt} (left) and SSB_{tran} (right) during the tandem phase of Jason-2 and Jason-3 (units: m).

The spatial differences in SSB seen in figures 4.22, 4.23 and 4.24 reveal SSB residuals associated with the different instrument behavior of each mission. Jason-1, -2 and -3 share the same Poseidon-type dual frequency altimeters (Poseidon-2, -3 and -3b, respectively). TOPEX/Poseidon flew two on-board altimeters (NRA and Poseidon) sharing the same antenna, being NRA the primary instrument aboard the spacecraft. For T1 (TOPEX/Jason-1), mean differences obtained with SSB_{upt} reveal a latitude dependency, producing mean SSB residuals of around 2 cm in the tropical zones, that decrease to values close to zero at higher latitudes. This regional dependency is not observed for the tandem phases T2 and T3, where SSB_{upt} mean differences are uniform over all the lat-lon domain, with residuals of $\approx \pm$ 3 cm. It can also be verified by the analysis of the figures that SSB_{tran} produces hardly any residuals at tandem phases T2 and T3, thus indicating that a specific SSB model parameterization was not designed for each mission. Table 4.6 shows the statistics of the differences in the main sea state descriptors and SSB estimates between the two altimeters in each tandem phase.

Table 4.6: Statistical results of mean differences and standard deviations for each SSB model and sea-state descriptors when computed for the three tandem phases T1 (TOPEX/ Jason-1), T2 (Jason-1/Jason-2) and T3 (Jason-2/Jason-3). (all results are presented in cm, except for U_{10} and T_z Q_{04}, in m/s and s, respectively).

		$\mathbf{H_s}$	$\mathbf{U_{10}}$ **(m/s)**	$\mathbf{T_z\ Q_{04}}$	**-3.8%** $\mathbf{H_s}$	$\mathbf{SSB_{cls}}$	$\mathbf{SSB_{tran}}$	$\mathbf{SSB_{upt}}$
T1	mean	2.49	-0.01	15.37	-0.09	0.32	-	-0.61
	std	7.38	0.25	18.88	0.28	0.61	-	0.83
T2	mean	-2.09	0.13	-26.65	0.07	-2.80	0.15	-4.44
	std	8.83	0.21	14.97	0.33	0.42	0.33	0.67
T3	mean	0.11	0.25	-03.14	0.00	-0.08	-0.08	2.76
	std	6.94	0.25	13.17	0.26	0.22	0.25	0.52

As expected, when computing the mean differences for the altimeter retrieved sea-state descriptors (H_s, U_{10}) and the derived (T_z Q_{04}) during the tandem phase, the residuals are close to zero. This is due to the short time separation between the missions in the tandem phase, meaning that each altimeter in the tandem retrieves the same sea-state conditions. The low limit benchmark of $-3.8\%Hs$, which depends only on altimetric significant wave height, can be considered null for the mean differences on the tandem phases. Compared with SSB_{cls} and SSB_{tran}, SSB_{upt} presents higher SSB residuals of -4.44 cm in T2 and +2.76 cm in T3. This could be attributed to the use of SSB model parameterizations that are customized for each altimeter mission, which means that this can be considered exclusively related to the instrumental contribution to the SSB. Since this tandem phases analysis reveals only relative and not absolute differences, it is only possible to infer that this contribution is larger for J2 than for J1 and J3, but without a true reference, one cannot determine the magnitude of the total SSB effect of instrumental origin.

4.7 Conclusion

This paper presented a thorough study of the design, development and assessment of SSB models based on 3 sea state predictors retrieved only from altimeter data and its application to the four altimeter reference missions (TOPEX, Jason1-3). In addition to the conventional sea-state predictors H_s and U_{10}, this work proposes the use of the altimeter derived wave period parameter T_z from the Q_{04} algorithm as a third predictor. This plays the role of mediator parameter, influencing the complexity of the relationship between H_s and U_{10} inputs.

Jason-2 was selected to inspect five different model designs and the impact of using training datasets with 120, 50, 20 and 10 cycles of data. From this assessment, the so-called "SSB_{upt} model", based on smoothing splines applied to each predictor using a tuning parameter of λ=5, was identified as the optimal model configuration. This model was subsequently used to evaluate the outputs obtained with four training datasets of different lengths. Systematic

comparisons were made between the various approaches and the established SSB_{cls} and SSB_{tran} models [19,42], using collinear analyses and temporal evolutions of SLA variance differences.

Results showed that the ideal dataset length (in the sense of the best compromise between data length and model performance) for model training is 50 cycles. Moreover, it was shown that this method makes it possible to derive a reliable SSB model with only 20 cycles of data, making this an interesting option to rapidly estimate SSB for newly-launched missions.

When applied to TOPEX, Jason-1 and Jason-3 missions, the performance of SSB_{upt}, both relative to the low limit benchmark of $-3.8\%Hs$ and to the SSB_{cls} and SSB_{tran} models, is globally positive, with a reduction of the global SLA variance for all missions compared to other SSB solutions.

The instrumental component of the SSB (tracker/skewness) was assessed by comparing the various SSB models during the tandem phases of the various missions. Due to the fact that SSB_{upt} models have been computed separately for each altimetric mission, the SSB_{upt} models exhibit global SSB residuals of -0.61 cm, -4.44 cm and +2.76 cm for the TP/J1, J1/J2 and J2/J3 tandem phases respectively. This suggests that the instrumental contribution to SSB is larger for Jason-2 than for the other missions.

The proposed SSB_{upt} model offers a simple and reliable way to estimate a correction for altimeter missions, even the recently-launched missions for which few data are available to estimate a robust empirical SSB model.

Acknowledgments

This work was funded by the European Space Agency (ESA) Scientific Exploitation of Operational Missions (SEOM) Programme Element, in the scope of project SCOOP - SAR Altimetry Coastal & Open Ocean - Performance Exploitation and Roadmap Study.

Author Contributions

Nelson Pires and M. Joana Fernandes conceived the experiments; Nelson Pires designed and performed the experiments; All authors analyzed the data and reviewed the study; Nelson Pires wrote the paper.

References

1. M. Srokosz and M. S. Longuet-Higgins, "On the skewness of sea-surface elevation," Journal of Fluid Mechanics, vol. 164, no. -1, p. 487, apr 1985.

2. W. K. Melville, R. H. Stewart, W. C. Keller, J. A. Kong, D. V. Arnold, a. T. Jessup, M. R. Loewen, and a. M. Slinn, "Measurements of electromagnetic bias in radar altimetry," Journal of Geophysical Research, vol. 96, no. C3, p. 4915, 1991.

3. D. Chelton, E. J. Walsh, and J. MacArthur, "Pulse Compression and Sea Level Tracking in Satellite Altimetry," Journal of Atmospheric and Oceanic Technology, vol. 6, pp. 407–438, 1989.

4. C. P. Gommenginger, M. Srokosz, J. Wolf, and P. Janssen, "An investigation of altimeter sea state bias theories," Journal of Geophysical Research, vol. 108, pp. 1–13, 2003.

5. B. Yaplee, A. Shapiro, D. Hammond, B. Au, and E. Uliana, "Nanosecond radar observations of the ocean surface from a stable platform," IEEE Transactions on Geoscience Electronics, vol. 9, no. 3, p. 170174, 1971.

6. D. E. Barrick and B. J. Lipa, "Chapter 3 analysis and interpretation of altimeter sea echo," Advances in Geophysics Satellite Oceanic Remote Sensing, p. 61100, 1985.

7. M. Srokosz, "On the joint distribution of surface elevation and slopes for a nonlinear random sea, with an application to radar altimetry,"Journal of Geophysical Research, vol. 91, no. C1, p. 995, 1986.

8. F. W. Millet, K. F. Warnick, and D. V. Arnold, "Electromagnetic Bias at Off-nadir Incidence Angles," Journal of Geophysical Research, vol. 110, no. C9, 2005.

9. F. W. Millet, K. F. Warnick, J. R. Nagel, and D. V. Arnold, "Physical optics-based electromagnetic bias theory with surface height-slope cross-correlation and hydrodynamic modulation," IEEE Transactions on Geoscience and Remote Sensing, vol. 44, no. 6, pp. 1470–1483, jun 2006.

10. P. Gaspar, P. Le Traon, and O. Zanife, "Estimating the sea state bias of the TOPEX and POSEIDON altimeteres from crossover differences,"Journal of Geophysical Research, vol. 99, no. 12, pp. 24 981–24 994, 1994.

11. M. Jiang, K. Xu, Y. Liu, and L. Wang, "Estimating the Sea State Bias of Jason-2 Altimeter From Crossover Differences by Using a Three-Dimensional Nonparametric Model," IEEE Journal Of Selected Topics In Applied Earth Observations And Remote Sensing, vol. 9, no. 11, pp. 5023–5043, 2016.

12. D. Chelton, "The sea state bias in altimeter estimates of sea level from collinear analysis of TOPEX data," Journal of Geophysical Research, vol. 99, pp. 24 995–25 008, 1994.

13. D. Vandemark, N. Tran, B. Beckley, B. Chapron, and P. Gaspar, "Direct estimation of sea state impacts on radar altimeter sea level measurements," Geophysical Research Letters, vol. 29, no. 24, p. 2148, 2002.

14. N. Pires, M. J. Fernandes, C. Gommenginger, and R. Scharroo, "A Conceptually Simple Modeling Approach for Jason-1 Sea State Bias Correction Based on 3 Parameters Exclusively Derived from Altimetric Information," Remote Sensing, vol. 8, no. 576, pp. 1–13, 2016.

15. R. Scharroo and J. Lillibridge, "Non-Parametric Sea-State Bias models and their relevance to sea level change studies," in Proceedings of the 2004 Envisat & ERS Symposium, vol. 2004, no. April, 2005.

16. S. Labroue, P. Gaspar, J. Dorandeu, O. Zanifé, F. Mertz, P. Vincent, and D. Choquet, "Nonparametric Estimates of the Sea State Bias for the Jason-1 Radar Altimeter," Marine Geodesy, vol. 27, pp. 453–481, 2004.

17. J. Hausman and V. Zlotnicki, "Sea State Bias in Radar Altimetry Revisited," Marine Geodesy, vol. 33, pp. 336–347, 2010.

18. P. Gaspar and J. Florens, "Estimation of the sea state bias in radar altimeter measurements of sea level: Results from a new nonparametric method," Journal of Geophysical Research, vol. 103, no. 98, pp. 803–814, 1998.

19. P. Gaspar, S. Labroue, and F. Ogor, "Improving Nonparametric Estimates of the Sea State Bias in Radar Altimeter Measurements of Sea Level," Journal of Atmospheric and Oceanic Technology, vol. 19, pp. 1690–1707, 2002.

20. R. E. Glazman, A. Greysukh, and V. Zlotnicki, "Evaluating models of sea state bias in satellite altimetry," Journal of Geophysical Research, vol. 99, no. C6, pp. 12 581–12 591, 1994.

21. R. Kumar, D. Stammer, W. K. Melville, and P. Janssen, "Electromagnetic bias estimates based on TOPEX, buoy, and wave model data," Journal of Geophysical Research, vol. 108, no. C11, p. 3351, 2003.

22. R. Glazman, A. Fabrikant, and M. Srokosz, "Numerical Analysis of the Sea State Bias for Satellite Altimetry," Journal of Geophysical Research, vol. 101, no. C2, pp. 3789–3799, 1996.

23. N. Tran, D. Vandemark, B. Chapron, S. Labroue, H. Feng, B. Beckley, and P. Vincent, "New models for satellite altimeter sea state bias correction developed using global wave model data," Journal of Geophysical Research, vol. 111, no. C09009, 2006.

24. N. Tran, D. Vandemark, S. Labroue, H. Feng, B. Chapron, H. L. Tolman, J. Lambin, and N. Picot, "Sea state bias in altimeter sea level estimates determined by combining wave model and satellite data," Journal of Geophysical Research, vol. 115, no. C03020, pp. 1–7, 2010.

25. W. K. Melville, F. Felizardo, and P. Matusov, "Wave slope and wave age effects in measurements of electromagnetic bias," Journal of Geophysical Research, vol. 109, no. C7, p. C07018, 2004.

26. H. Feng, S. Yao, L. Li, N. Tran, D. Vandemark, and S. Labroue, "Spline-Based Nonparametric Estimation of the Altimeter Sea-State Bias Correction," IEEE Geoscience and Remote Sensing Letters, vol. 7, no. 3, pp. 577–581, 2010.

27. H. Tolman, User manual and system documentation of WAVEWATCH III version 4.18, 2014, no. 316.

28. T. W. Group, "The WAM Model - A Third Generation Ocean Wave Prediction Model," Tech. Rep., 1988.

29. P. Hwang, W. Teague, G. Jacobs, and D. Wang, "A statistical comparison of wind speed, wave height, and wave period derived from satellite altimeters and ocean buoys in the Gulf of Mexico region," Journal of Geophysical Research, vol. 103, no. C5, pp. 10 451–10 468, 1998.

30. C. P. Gommenginger, M. Srokosz, P. Challenor, and D. Cotton, "Measuring ocean wave period with satellite altimeters: A simple empirical model," Geophysical Research Letters, vol. 30, no. 22, p. 2150, 2003.

31. Y. Quilfen, B. Chapron, F. Collard, and M. Serre, "Calibration/Validation of an Altimeter Wave Period Model and Application to TOPEX/Poseidon and Jason-1 Altimeters," Marine Geodesy, vol. 27, pp. 535–549, 2004.

32. S. Caires, A. Sterl, and C. P. Gommenginger, "Global ocean mean wave period data: Validation and description," Journal of Geophysical Research, vol. 110, no. C02003, pp. 1–12, 2005.

33. E. Mackay, C. H. Retzler, P. Challenor, and C. P. Gommenginger, "A parametric model for ocean wave period from Ku band altimeter data," Journal of Geophysical Research, vol. C03029, no. December 2007, pp. 1–16, 2008.

34. B. Beckley, N. Zelensky, S. A. Holmes, F. Lemoine, R. D. Ray, G. T. Mitchum, S. D. Desai, and S. T. Brown, "Assessment of the jason2 extension to the topex/poseidon, jason1 sea-surface height time series for global mean sea level monitoring," Marine Geodesy, vol. 33, pp. 447–471, 08 2010.

35. R. Scharroo, "RADS version 3.1 User Manual and Format Specification," 2012.

36. R. Scharroo, "RADS Version 4.2.4 User Manual" 2016.

37. O. B. Andersen, L. Stenseng, G. Piccioni, and P. Knudsen, "The dtu15 mss (mean sea surface) and dtu15lat (lowest astronomical tide) reference surface," Abstract from ESA Living Planet Symposium 2016, Prague, Czech Republic, 2016.

38. P. G. Challenor and P. D. Cotton, "The joint calibration of altimeter and in situ wave heights," Doc. WMO/TD-1081, JCOMM Tech. Rep. 13, World Meteorol. Org., Geneva, 2002.

39. C. P. Gommenginger, M. Srokosz, P. Challenor, and D. Cotton, "Development and validation of altimeter wind speed algorithms using an extended collocated Buoy/Topex dataset," IEEE Transactions on Geoscience and Remote Sensing, vol. 40, no. 2, pp. 251–260, 2002.

40. G. James, D. Witten, T. Hastie, and R. Tibshirani, An Introduction to Statistical Learning, 4th ed., Springer, Ed., 2014.

41. S. Wood, Generalized Additive Models: an introduction with R, 2006, vol. 62, no. 4.

42. N. Tran, S. Philipps, J-C. Poisson, E. Bronner, and N. Picot, "Impact of GDR-D standards on SSB corrections Jason-1 SSB comparison," Ocean Science Topography Science Team Meeting, Venice, Italy, 2012.

43. N. Tran, S. Labroue, S. Philipps, E. Bronner, and N. Picot, "Overview and Update of the Sea State Bias Correction for the Jason-2, Jason-1 and TOPEX Missions," Marine Geodesy, vol. 33, pp. 348–362, 2010.

Chapter 5

Article 3: Perspectives on Jason-3 and Sentinel-3 sea state bias by combining SAR Sentinel-1 Ocean Wave parameters

Nelson Pires [1], M. Joana Fernandes [1], Christine Gommenginger [2] and Remko Scharroo [3]

[1] Department of Geosciences, Environment and Spatial Planning, Faculty of Sciences, University of Porto, Porto 4169-007, Portugal
[2] National Oceanography Centre, Natural Environment Research Council, Southampton SO14 3ZH, UK
[3] European Organisation for the Exploitation of Meteorological Satellites, Darmstadt D-64295, Germany

Manuscript submitted

Target Academic Journal: **Earth and Space Science**

5.1 Abstract

This paper presents a synergetic study using the two-dimensional ocean surface wave spectra information delivered by Sentinel-1 Level-2 Ocean Swell Wave component in order to inspect the possible impact of surface wave propagation direction and length on Jason-3 and Sentinel-3 altimeter retrievals, as well as the consequences it may have for the altimeter sea state bias (SSB) correction and new SSB modelling approaches. A collocation procedure of the observations has been performed for the year 2017, thus allowing to cross distinct information of wave systems propagating over the globe into different sea-state regimes. The altimeter significant wave height (H_s) and backscatter cross-section measurements (σ_0), as well as the associated standard deviation of the residuals of 1-Hz averages, have been related with dominant swell wave direction and wavelength, showing linear dependencies between longer waves and the altimeter retrievals of Sentinel-3 operating into SAR mode. Similar results have been achieved for the pseudo lower resolution mode, indicating some discrepancies when compared with the conventional low resolution mode instrument onboard Jason-3. Sea surface height variance analysis show higher values for the domain regions where the 1^{st} and 2^{nd} dominant swell wavelength contribute equally to H_s, revealing a correlation with altimeter observations and the related residuals, thus opening new perspectives for the use of Sentinel-1 swell wave information on dedicated sea state bias models applied to both Jason-3 and Sentinel-3.

Keywords: satellite altimetry; two-dimensional spectra; wave direction; wavelength; ssb

5.2 Introduction

Satellite altimetry is nowadays a well established remote sensing technique for ocean monitoring, retrieving geophysical measurements such as the sea surface height (SSH), significant wave height (H_s) and the near-surface wind speed (U_{10}) derived from the altimeter backscatter cross section measurements (σ_0). One of the major contribution for inaccurate observations, is the so-called sea state bias (SSB), an altimeter ranging error mostly caused by the sea-state effects on the satellite footprint [1]. The modelling approaches normally adopted for SSB estimation, are usually developed empirically from parametric or non-parametric techniques based on two geophysical predictors, the altimeter-derived H_s, and the U_{10} inferred from σ_0 [2, 3], but it is known that only these two retrievals are not enough to accurately characterize the different wave systems found on the ocean surface with distinct non-linear interactions and propagation directions. In order to address this difficulty, some approaches for SSB modelling make use of an additional third predictor characterized by the mean wave period (T_z) which can be retrieved from numerical wave models [4, 5, 6] or altimetric-derived from indirect empirical approaches [7, 8]. Although some improvements have been achieved in the use of T_z for SSB characterization, it is also recognized that this additional information is not sufficient to explain some of the SSH variability and to understand some of the physical phenomena behind the relationship between SSB modulation and environmental conditions.

The ocean sea surface is usually characterized by wind sea systems, generated by local winds, and swell ocean waves, caused by distant weather systems. Although the former are not large enough to disturb the altimetric signal, the swell systems, with larger dominant heights and wavelengths, may play an important role on how they might affect the H_s and U_{10} measures retrieved by radar altimetry, depending on the dominant swell direction and length when the altimeter overflies distinct oceanic regions [9, 10]. With the launch of CryoSat-2 (C-2) SIRAL altimeter in 2010, it became possible to monitor the ocean with a closed-burst Synthetic Aperture Radar (SAR) instrument, which helped to achieve significant improvements on reducing the noise of measurements and on spectral information content when compared to previous pulse-limited instruments using conventional low resolution modes (LRM) [11]. The success in the exploitation of the C-2 measurements, acquired in SAR mode (SARM) only over specific regions defined by the instrument mode mask (the remaining regions being acquired in LRM and SAR-Interferometric modes [12]), led to the implementation of an altimeter continuously operating in SAR mode on Sentinel-3 mission.

Taking advantage of the higher along-track resolution of 300 m delivered by C-2, two major studies [13, 14] were performed in order to find possible effects of swell wave systems on SAR waveforms and on SSH measurements. Different approaches were used, and the reached conclusion are distinct. While [13] carried out experimental investigations with collocated data of C-2 SAR mode acquisitions over Envisat ASAR swell data, concluding that no statistically effects of swell were found for waveforms shapes and SSH biases, [14] analysed the impact of long ocean waves using the C-2 SAR mode measurements and simulated data, showing some swell effects through the noisier altimeter waveforms under long-wave conditions. Due to the geographic limits of C-2 SAR acquisition mode, just confined to some ocean basins and coastal zones, both studies agree in the need for extending the analysis for larger ocean areas and number of observations.

The present study follows this line of investigation in order to find better correlations between different swell systems and the altimetric retrievals used as predictors for SSB estimations. To accomplish this goal, a synergistic approach using Jason-3 (J-3), Sentinel-3 (S-3) and Sentinel-1 (S-1) has been conducted for the year 2017, where the different data sources were collocated and analysed in the sense of using swell information (height, wavelength and direction) retrieved from S-1 L2 products and measure the possible impact of these sea state correlators on SSB estimations. An in-depth study is also carried out to determine how the Sentinel-3 SAR measures Hs and U_{10} differ from the corresponding pseudo-LRM (PLRM) measures in order to evaluate their impact on SSB models.

The paper is arranged as follows. In section 5.3 the datasets available and used for the study are described. A short explanation about the origin of Sentinel-1 Ocean (OCN) products and the Ocean swell spectra (OSW) is provided, as well as the various wave retrievals derived from the two-dimensional ocean surface wave spectra. The different altimeter acquisition modes of Jason-3 and Sentinel are also introduced. Section 5.4 describes the collocation procedure for S-1/J-3 and S-1/S-3, the inherent technical difficulties due to orbital constraints between missions,

and statistical analyses of geophysical parameters to evaluate the dataset quality. Section 5.5 is dedicated to the discussion of the achieved results after the chosen methodologies for the combination of S-1 swell wave parameters with the altimeter-derived retrievals of J-3 and S-3. Statistical analyses are provided for dominant swell wave propagation direction and wavelength. The repercussions of different wave characteristics on standard SSB models and SSH anomalies (SSHA) are evaluated in section 5.6. Finally, section 5.7 depicts the main conclusions of this study.

5.3 Available Datasets

The study has been performed for the entire year of 2017, using altimeter data of Jason-3 and Sentinel-3A retrieved from the Radar Altimeter Database System (RADS) [15]. RADS delivers an up-to-date and consistent altimeter database at 1-Hz, with the latest instrument and geophysical corrections for sea level anomaly (SLA) construction, and is expanded with additional data and external corrections adjusted for each altimetric measurement. In continuity with the previous reference missions, Jason-3 operates in the conventional low-resolution mode (LRM), transmitting pulses and incoherently processing the surface reflections pulse-by-pulse. On the other hand, Sentinel-3 has on board a SAR altimeter operating in the closed-burst mode, similar to that used on CryoSat-2, where the signal is transmitted and received in correlated bursts of 64 pulses [11]. Closed-burst SAR waveforms used on Sentinel-3 can be transformed into pseudo-LRM waveforms (PLRM) similar to LRM, thus being retracked with the same retrackers used for conventional altimetry.

This study takes advantage of the fact that RADS has both SAR and PLRM measurements available for Sentinel-3, thus making possible to evaluate the impact of swell systems on these two datasets. Sentinel-1 Level-2 Ocean (OCN) products operating in the nominal acquisition Wave mode (WV) for wave applications, can provide the Ocean Swell spectra (OSW) component in the form of *imagettes* with an approximate satellite footprint of 20 × 20 km and a nominal spatial resolution of 4 m for both VV and HH polarization. The mission operates in the C-band (5.3 GHz), alternating between two incidence angles

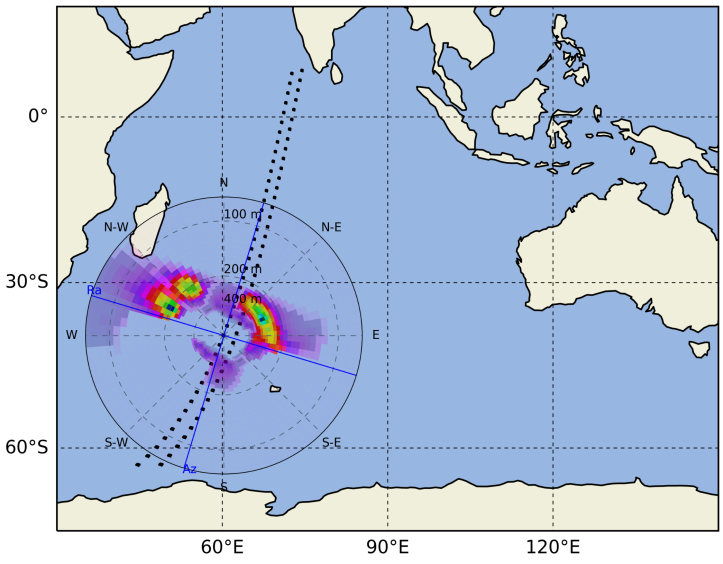

Figure 5.1: Sentinel-1A acquisition segment in Wave Mode over the Indian Ocean with the black squares representing the 84 retrieved imagettes. The polar plot represents the estimated swell spectrum for imagette #56.

23° (WV1) and 36° (WV2), and acquiring imagettes with the same incidence angle separated by 200 km. The OSW component provides the two-dimensional ocean surface wave spectra retrieved by inversion of the corresponding image cross-spectra of a Sentinel-1 Level 1 Single-Look Complex (SLC) SAR image, as well as integrated wave parameters derived from the ocean wave spectra, and additional image statistics derived directly from the imagette [16].

Figure 5.1 illustrates an example of Sentinel-1A acquisition segment in Wave mode with the imagettes footprint over the Indian Ocean between 00h:57m:31s and 01h:17m:50s on February 1, 2017. This descending pass produced 84 imagettes, 42 for each incidence angle, being the two-dimensional swell wave spectrum of imagette #56 also shown in the figure. For this case, the imagette acquisition date is 01h:10m:57s, and its centroid coordinates are $(\varphi, \lambda) \rightarrow (-39.556°, 60.186°)$. The wave spectrum shows two dominant wave systems with the following derived integrated parameters (direction, height, length): (294°, 1.49 m, 190 m)$_1$ and (64°, 1.46 m, 268 m)$_2$, and the platform heading angle is 196.75°. Because OCN products are derived from Level-1 Single Look Complex (SLC) images in the slant range by azimuth imaging plane, for synergetic studies with satellite altimetry data, it must be taken into account that the spectral resolution provided by OSW component depends on the sea-state of the illuminated area and the direction of wave propagation relative to the satellite azimuth.

5.4 Collocation Procedure

Due to the different orbital characteristics, all datasets need to be collocated in order to guarantee the best compatibility between time and space scales. Sentinel-1 has a sun-synchronous orbit with an altitude of 693 km, inclination of 98.18°, orbital period of 98.6 min, and a Local Time Ascending Node (LTAN) at 18:00 hours. To allow time series continuation with its predecessors, Sentinel-3 follow a sun-synchronous orbit as well, with a mean altitude of 815 km, inclination of 98.6° and LTAN at 22:00 hours. On the other hand, Jason-3 flies on a non-sun-synchronous orbit with a mean altitude of 1336 km, inclination of 66.04° and 112 min per revolution. Because Sentinel-1 and Sentinel-3 orbits are both sun-synchronous with a LTAN difference of 240 min, it becomes impossible to find spatial collocated observations with a lower temporal separation (apart from locations at extreme northern and southern latitudes), but due to its non-sun-synchronous orbit, this is not the case for Jason-3.

For the period considered in this study, 23,349 Sentinel-1 OCN products were available from January 1, 2017 to December 31, 2017, roughly corresponding to 1,242,556 imagettes for both WV1 and WV2 incidence angles. Due to all orbital constraints described above, the chosen time separation between collocated observations was $\leqslant$ 100 min for S-1/J-3, and $\leqslant$ 300 min for S-1/S-3. With respect to the spatial separation between altimeter points and imagette centroid, the chosen values were $\leqslant$ 100 km for S-1/J-3, and $\leqslant$ 200 km for S-1/S-3. Since the 1-Hz altimeter measurements are collected every second along the satellite ground track with a space separation of around 7 km, the adopted procedure for collocation produced a raw number of

628,827 matchups for S-1/J-3, and 4,674,652 for S-1/S-3. Figure 5.2 shows the global distribution of match points achieved with the chosen collocation criteria. Both datasets cover the Northern and Southern Hemispheres, including information of open ocean for all sea-state regimes. It should be noted the absence of matchups in some regions of North and South Atlantic, due to the lack of Sentinel-1 Level-2 OCN products in those regions for the period considered in this study.

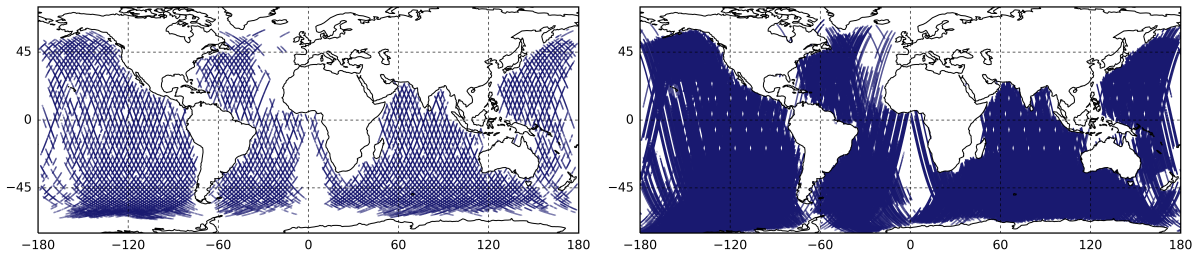

(a) Collocated measurements for S-1/J-3. (b) Collocated measurements for S-1/S-3.

Figure 5.2: Global distribution of Sentinel-1 imagettes collocated with Jason-3 and Sentinel-3 measurements for the chosen time and space criteria.

In order to evaluate the results from the described collocation procedure, a first assessment was carried out using the altimeter retrievals H_s and U_{10}, against the sum of significant wave heights of the 1st and 2nd dominant swell heights found for the partitioned wave spectra, and the estimated wind speed available in the OSW component. Figure 5.3 shows the comparison results of Jason-3 and Sentinel-3 H_s observations with the swell height derived from Sentinel-1 OCN products. The bi-dimensional histograms of samples are filled with the metrics of frequency of unique values, arithmetic mean along the datasets, Mean Absolute Error (MAE), Root Mean Squared Error (RMSE), and the Pearson correlation coefficient between datasets.

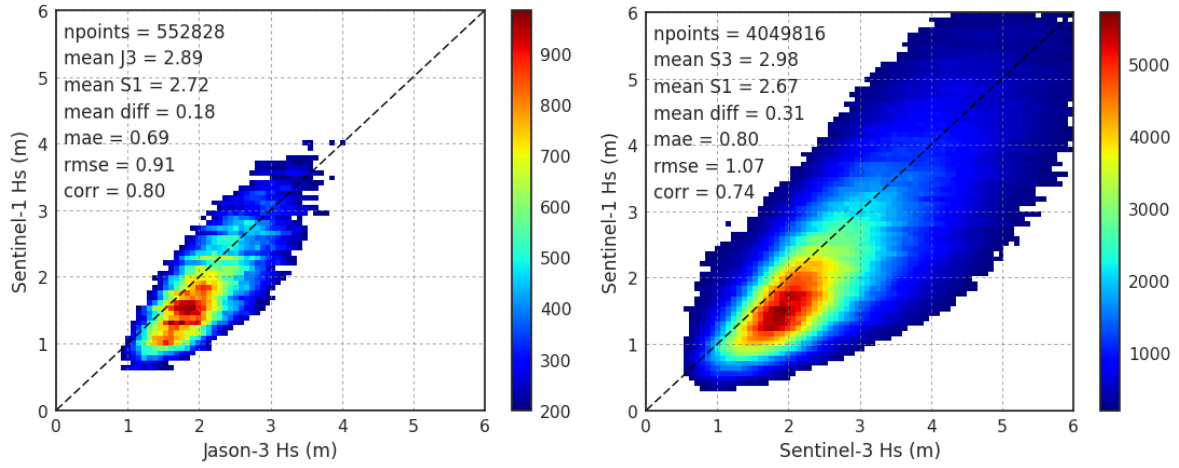

(a) Bi-dimensional histogram for S-1/J-3 H_s. (b) Bi-dimensional histogram for S-1/S-3 H_s.

Figure 5.3: Scatter diagrams of Jason-3 and Sentinel-3 H_s altimeter observations against the derived H_s from Sentinel-1 OSW component, with corresponding metrics.

From the same figure is it possible to observe a slight underestimation of S-1 H_s when against to J-3 and S-3 H_s, which may be due to a number of reasons: first, only the 1st and 2nd dominant swell heights are being considered, leaving out the possible high frequency contributions of wind sea heights known to be captured by the altimetric observations; second, previous studies from [17, 18] concluded that wave H_s height derived from SAR is less accurate than the altimeter-measured H_s, which can explain some of the discrepancies; third, the sampling density of Sentinel-1 OSW component is of one imagette per 100 km, much lower than the altimeter measurements with a ground track spacing of 7 km, and thus containing less statistical significance. Figure 5.3b shows an expected higher scattering in comparison with the results for S-1/J-3, due to the greater temporal and spatial separation of S-1/S-3 collocated measurements, but even so, a correlation value of 0.74 is achieved, which may be considered acceptable given the constraints of the available observations.

As in the case for radar altimeter, the intensity of the backscattered signal of a SAR image (σ_0) is also strongly related to the ocean surface wind speed (U_{10}), and compared to the wave retrieval, the wind retrieval from SAR achieves better results since relies on more matured techniques combining the measured radar cross-section with the radar cross-section of geophysical models functions [19,20]. After comparison with global atmospheric models available from the European Centre for Medium-Range Weather Forecasts (ECMWF), calibration and validation results for polarisation and swath performance of S-1 L2 wave mode, better performances are achieved for VV polarization, with a bias < 0.26 m/s, being the main operational mode used in this study [21]. Figure 5.4 illustrates the analysis made for the derived Jason-3 and Sentinel-3 U_{10} compared with the wind speed estimation available in Sentinel-1 OSW component.

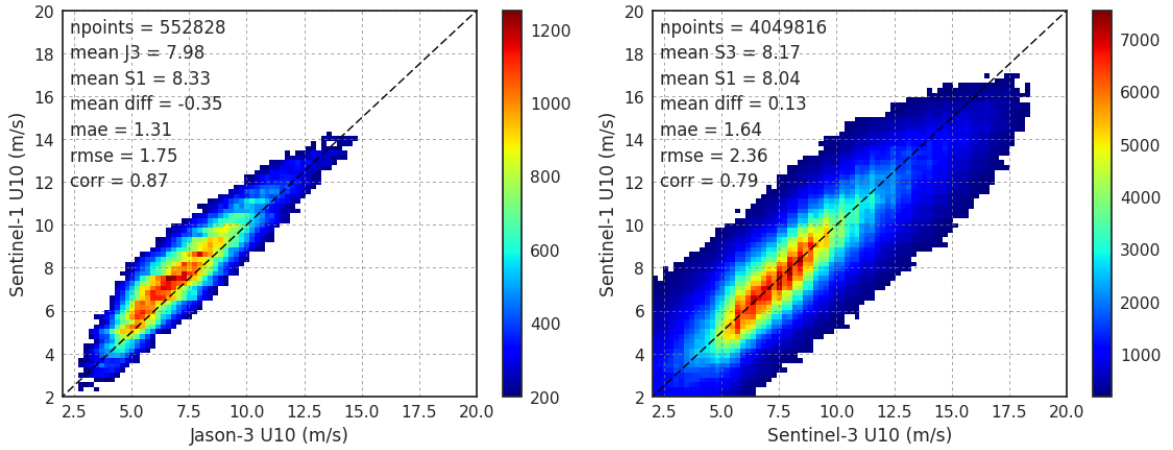

(a) Bi-dimensional histogram for S-1/J-3 U_{10}.

(b) Bi-dimensional histogram for S-1/S-3 U_{10}.

Figure 5.4: Scatter diagrams of Jason-3 and Sentinel-3 U_{10} altimeter observations against the derived U_{10} from Sentinel-1 OSW component, with corresponding metrics.

Again, due to the smaller temporal and spatial spacing, the collocated datasets for S-1/J-3 presents a lower MAE and a higher correlation coefficient when compared with the results obtained for S-1/S-3, but still, despite the greater lag of the Sentinel-3's orbit over Sentinel-1,

it is possible to obtain a high U_{10} correlation value of 0.79, thus making it feasible to compare parameters between both datasets. After the collocation procedure, a number of additional quality checks and selection criteria have been performed. From the altimeter side, only the open ocean measurements were selected with a distance to coast greater than 50 km to ensure the absence of any coastal region contamination in altimeter measurements. After this first step, the retrieved J-3/S-3 H_s and U_{10} have been limited to $0-6$ m and $1-20$ m/s respectively, in order to obtain a stable dataset whose parameters are less influenced by instrumental or geophysical residual errors. Taking the altimeter measurements as the quality control, the collocated S-1 parameters were subsequently subjected to necessary cleaning procedures, where some negative values of 1st and 2nd dominant swell height, length and direction had to be removed. After all these operations, both datasets had a matchup reduction of around 13%, reaching a final number of collocated points of 552,828 for S-1/J-3, and 4,049,816 for S-1/S-3, with a predominance of the density in the regional areas of South Pacific and North Atlantic, corresponding to the oceanic regions where the swell systems are fully developed and may cause a greater impact on the altimeter retrievals.

5.5 Combining S-1 swell with J-3 and S-3

In order to ascertain the variability of altimeter-derived geiphysical parameters in the presence of swell, a set of analyses has been carried out for H_s and σ_0. Additionally, since RADS provides altimeter statistics for 1-Hz averages based on higher rate (10, 20 or 40 elementary measurements per second), the standard deviation of the residuals (standard deviation or RMS of the differences between the valid high rate values and the corresponding 1-Hz mean value) was also inspected to better understand the swell impact on each altimetric parameter available on the database for all retrieving modes: Jason-3 LRM, Sentinel-3 SARM and PLRM.

5.5.1 Wave direction analyses

One of the wave parameters retrieved from the two-dimensional ocean wave spectra and available in Sentinel-1 OSW component, is the dominant direction, counting from the North, at the wave peak computed per each partitioned wave spectra ($\phi^{(p)}_{peak}$), this way allowing the possibility to estimate the 1st and 2nd dominant wave directions of swell systems. Figure 5.5 show how the altimeter retrievals H_s and U_{10}, and how the respective standard deviation of the residuals vary in the wave direction domain. The top, medium and bottom panels of this figure present the results for J-3 LRM, S-3 SARM and S-3 PLRM respectively. From left to right, the various panels show the results for H_s, RMS of H_s residuals, σ_0 and RMS of σ_0 residuals respectively. Each panel illustrates the 2D diagram of each of the mentioned variables against the 1st dominant wave direction (x-axis) and the 2nd dominant wave direction (y-axis). For Jason-3, results show a significant increase of H_s when the 1st dominant swell wave direction is in the range of $60° - 120°$, i.e., when the wave system is propagating roughly perpendicular to the altimeter ground track.

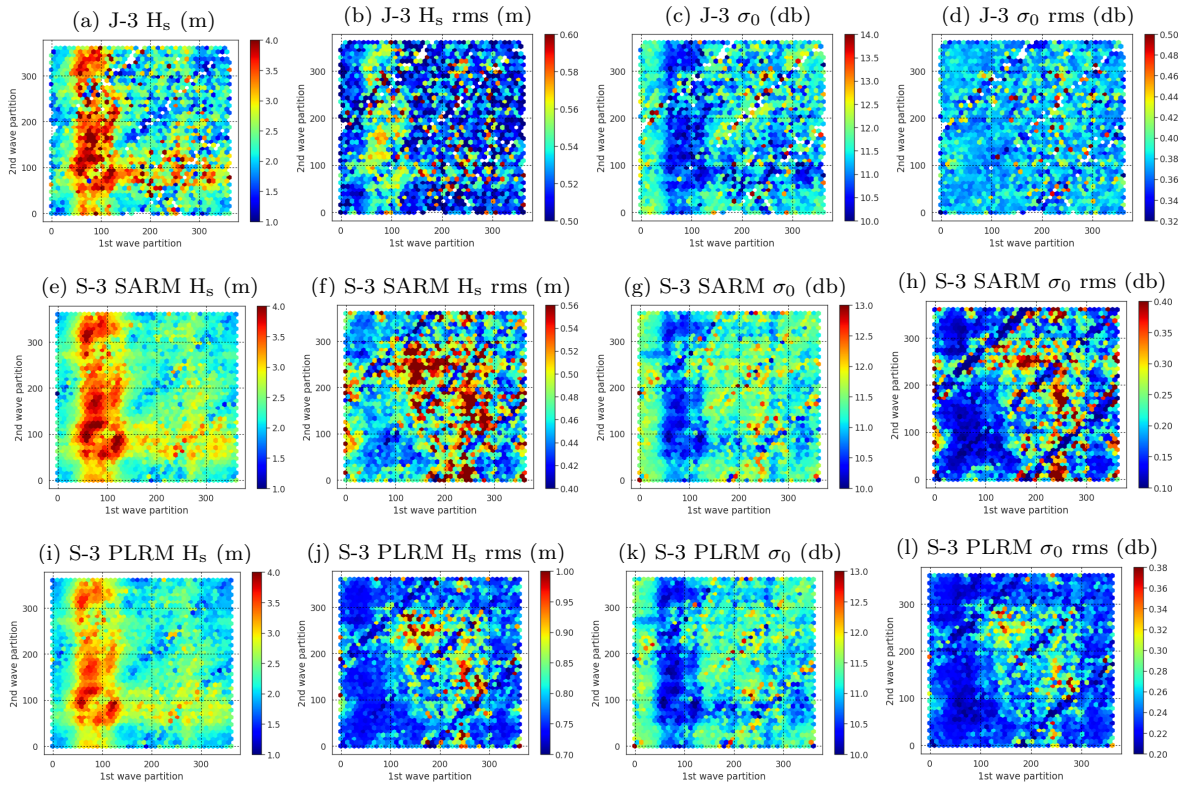

Figure 5.5: Bin averaged H_s, σ_0 and standard deviation of 1-Hz residuals of each parameter retrieved by Jason-3 (top), Sentinel-3 SARM (middle) and Sentinel-3 PLRM (bottom), plotted against the 1st and 2nd dominant wave directions of swell systems available in Sentinel-1 OSW component.

Although less relevant, this effect is also slightly observed for the 2nd dominant swell wave in the same range of propagation direction, but the focus will be put mainly on the first partition due to its higher wave height. Still concerning Jason-3, figure 5.5c shows a consistent decrease of σ_0 values on the same domain region where higher H_s values occur, indicating the presence of stronger wind speeds, and thus reducing the backscattered signal captured by the altimeter. The respective residuals associated to each altimetric parameter, show that J-3 H_s is subject to larger variability, reaching a root mean square (rms) of 0.56 m for the highlighted domain region (Fig. 5.5b), but the same is not verified for J-3 σ_0 rms (Fig. 5.5d). Figure 5.5 also shows how S-3 SARM/PLRM H_s and σ_0 vary with the swell dominant wave direction, and here is also possible to observe a strong increase of H_s accompanied by a decrease of σ_0 in the same domain region when waves have a propagation direction around 90° from the North. As it can be seen from figure 5.8 on page 89, these are expected results since most of the collocated measurements are located in the southern Pacific where the wind is blowing from the West with a stronger U_{10}, and the Antarctic Circumpolar current (ACC) is flowing in the same direction, thus leading to the generation of swell systems with higher wave heights. But despite the consistency of results achieved for the absolute values of J-3, S-3 SARM/PLRM H_s (Fig. 5.5e) and σ_0 (Fig. 5.5f), the same is not observed for the standard deviation of the residuals of 1-Hz averages, where

the highlighted domain region for the considered wave direction in the range of $60° - 120°$ have lower H_s and σ_0 root mean squared values for S-3 SARM when compared to J-3 (Fig. 5.5g and 5.5h) , decreasing roughly 12 cm and 0.25 db respectively, thus indicating better performances in the considered domain region where the retrieved parameters are less affected by swell impacts. In comparison with S-3 SARM, S-3 PLRM shows higher rms values for both altimeter H_s and σ_0, increasing the residuals by more than 30 cm and 0.1 db (Fig. 5.5j and 5.5l). In addition, the absolute values of both H_s and σ_0 from S-3 PLRM show a slight signal smoothing when compared with the corresponding values from J-3 LRM, evidencing that, in this respect, S-3 PLRM is closer to S-3 SARM than to J-3 LRM.

To better understand how altimetric parameters may be affected by the different swell wave systems when satellite overflies a given region, a thorough study has been conducted for the standard deviation of H_s and σ_0 residuals of 1-Hz averages, and how their behaviour varies with: i) the retrieved absolute values of H_s, ii) and the 1^{st} dominant wave direction provided by S-1. The analysis was performed by establishing 6 different intervals of significant wave heights, of 1 m width, containing all the measurements available in the datasets: low wave heights for H_s within [0,1) m and [1,2) m, medium wave heights in the range [2,3) m and [3,4) m, high wave heights within [4,5) m and [5,6) m. The wave direction was partitioned into the 4 cardinal directions of compass rose, following the clockwise criteria and limited by $\pm 20°$ with respect to each direction, therefore, the following limits were considered: North centred at 0° and limited between $[340, 20)°$, East centred at 90° and limited between $[70, 110)°$, South centred at 180° and limited between $[160, 200)°$, and West centred at 270° and limited between $[250, 290)°$. Figure 5.6 shows the obtained results for Jason-3, Sentinel-3 SARM and PLRM, where the first column represents the number of observations for each class of H_s and each cardinal direction adopted in the analyses of the standard deviation of H_s and σ_0 residuals. With regard to the number of available measurements, figures 5.6a, 5.6d and 5.6g show that for each cardinal direction, the number of entries are similar for both datasets S-1/J-3 and S-1/S-3, being the East direction the one that brings together the largest set of matchups. In addition, it is also possible to verify that the highest frequency of measurements is found for medium/high H_s with limits between [2,5) m, when the surface waves are propagating eastwards, but this frequency is reduced for all other directions, where the most frequent H_s values decrease to the intervals within [1,3) m. With respect to the standard deviation of H_s residuals, figure 5.6b for Jason-3 and 5.6e for Sentinel-3 SARM do not show significant differences for most of the H_s ranges considered in the 4 principal directions, despite a slight increase of ≈0.2 m for S-3 SARM H_s rms in the range of [5,6) m, similar results are achieved for low and medium H_s in both sensors, with slightly higher residuals for ranges in the height extremes, lowering for medium H_s heights around the 2-3 m. However, S-3 PLRM presents an overall increase of the H_s rms of ≈0.2 m, which are even higher for the lowest range considered when H_s is between [0,1) m, surpassing an rms of 1 m for all the 4 considered main wave directions. Finally, the analysis of standard deviation of the σ_0 residuals shows significant differences on the three studied datasets (Figs. 5.6c, 5.6f and 5.6i), where J-3 presents an uniform σ_0 rms of ≈0.4 db for all H_s ranges and wave directions.

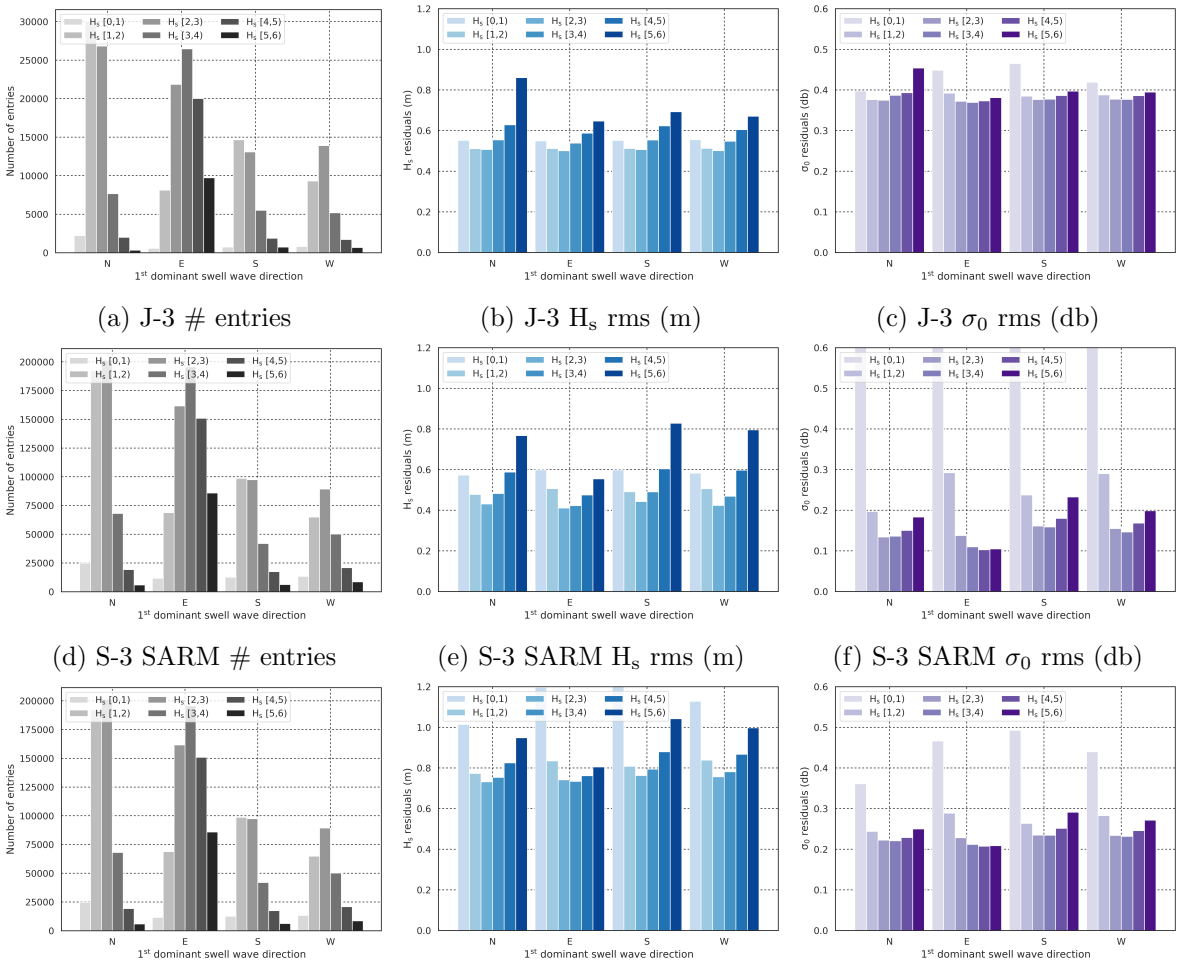

(a) J-3 # entries (b) J-3 H_s rms (m) (c) J-3 σ_0 rms (db)

(d) S-3 SARM # entries (e) S-3 SARM H_s rms (m) (f) S-3 SARM σ_0 rms (db)

(g) S-3 PLRM # entries (h) S-3 PLRM H_s rms (m) (i) S-3 PLRM σ_0 rms (db)

Figure 5.6: Standard deviation of the residuals for 1-Hz averages of H_s (central panels) and σ_0 (right panels) for low, medium and high 6 class intervals of H_s against the 4 defined cardinal directions (North, East, South and West) for J-3 (top), S-3 SARM (middle) and S-3 PLRM (bottom). The leftmost columns represent the number of observations (#) for each class interval of H_s and each cardinal direction.

Table 5.1: Mean values of Jason-3, Sentinel-3 SARM/PLRM standard deviation of the H_s and σ_0 residuals of 1-Hz averages, computed for each cardinal direction. Note: H_s rms in metres, σ_0 rms in decibels, and # defines the number of entries in thousand units.

	Jason-3			**Sentinel-3 SARM**			**Sentinel-3 PLRM**		
direction	**#**	**H_s rms**	**σ_0 rms**	**#**	**H_s rms**	**σ_0 rms**	**#**	**H_s rms**	**σ_0 rms**
North ↑	11	0.60	0.40	85	0.55	0.27	85	0.84	0.25
East →	14	0.56	0.39	112	0.49	0.31	112	0.85	0.27
South ↓	6	0.57	0.39	45	0.58	0.35	45	0.93	0.29
West ←	5	0.57	0.39	41	0.56	0.32	41	0.89	0.28

For S-3 SARM, these values decrease around 0.2–0.3 db depending on the cardinal direction, reaching the lowest level when waves are propagating eastwards, but curiously, a significant increase occurs when H_s is in the range of [0,1) m, surpassing the 1 db in almost every wave direction, raising the possibility of some instability in S-3 sensor for these ocean conditions when operating in the SAR mode. However, this behaviour is mitigated when S-3 PLRM measurements are considered, as shown by figure 5.6i). Table 5.1 summarizes these results for standard deviation of H_s and σ_0 residuals averaged for each cardinal direction and class of H_s values.

In order to give a global overview of the altimeter H_s and σ_0, figure 5.7 shows the distribution for the entire collocated datasets of S-1/J-3 and S-1/S-3 matchups. As expected, higher values of H_s are achieved mostly in the Southern Hemisphere in the latitude range between $-45°$ and $-65°$, and in the North Hemisphere for latitudes above 40° (Fig. 5.7a and 5.7b), the regions where longer waves under fully developed seas are more frequently found. However, these are also the regions where stronger winds are generated, thus causing a decrease on the altimeter backscatter cross section measurements σ_0, as shown by figures 5.7c and 5.7d for both retrievals of Jason-3 and Sentinel-3.

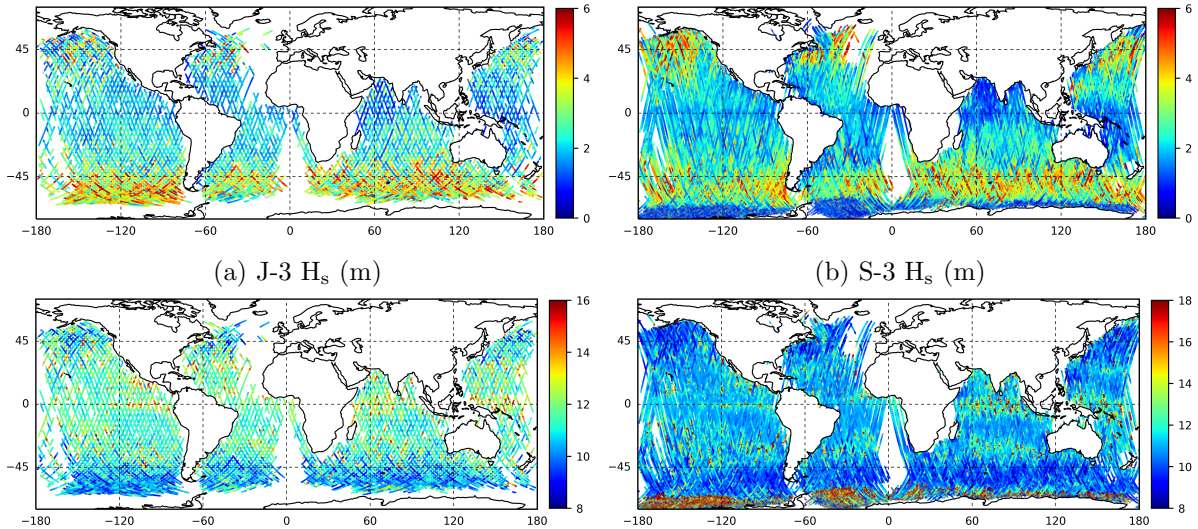

(a) J-3 H_s (m)

(b) S-3 H_s (m)

(c) J-3 σ_0 (db)

(d) S-3 σ_0 (db)

Figure 5.7: Global distribution of altimeter H_s and σ_0 for the entire collocated datasets of Sentinel-1 with J-3 and S-3.

As previously mentioned, the Southern Ocean is dominated by very strong winds blowing eastwards for long distances without interruption of landmasses (Westerlies). These persistent winds have a strong impact on ocean currents, such as the ACC, the largest ocean current which flows completely around the globe from West to East between the latitudes $-40°$ and $-60°$, connecting the Atlantic, Pacific, and Indian Oceans. Due to these combination of factors, the wind waves generated in these regions are among the highest found in the ocean, and as the prevailing winds and currents, have an eastwards propagation direction. Figure 5.8 shows

the location and respective H_s of the collocated measurements where the 1st dominant wave direction propagates from East to West, i.e., almost perpendicular to the altimeter ground track direction, in the range $70° - 110°$ counting from the North.

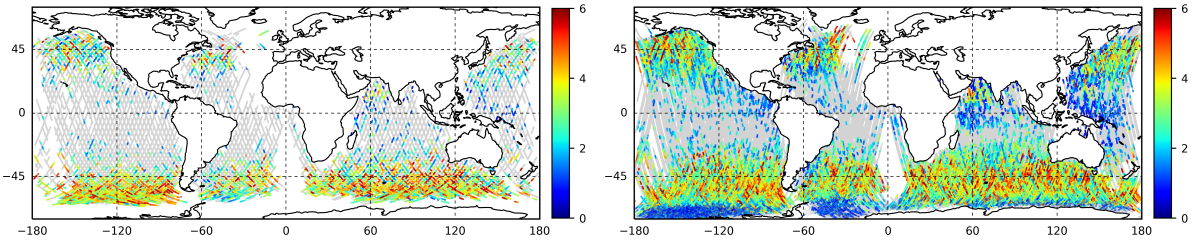

(a) J-3 H_s (m) (b) S-3 H_s (m)

Figure 5.8: Global distribution of altimeter H_s for the selected datasets of J-3 and S-3 collocated with S-1, where the 1st dominant swell wave direction is in the range of $70° - 110°$. Note: dots in grey corresponds to the full dataset.

This selection criteria shows similar outputs in the way both Jason-3 and Sentinel-3 retrieve the highest H_s values in the Southern Hemisphere, an expected result in line with the geophysical aspects of the region being considered. However, figure 5.8b shows that Sentinel-3 retains a large set of matchups with H_s below 2 m for similar wave propagation directions, and highlights extra dynamic patterns on these conditions not identified by Jason-3. This result could be due to the larger dimension of the available dataset for S-3, but may also be due to the higher along-track resolution of SARM, which with a footprint of ≈250 m, provides the ability to resolve shorter-scale ocean features and may thus have an impact on reducing the altimeter backscatter cross-section measurements, even though with a significant increase on the associated standard deviation of the linked residuals, as demonstrated by the previous figures 5.5g on page 85, 5.6f on page 87 and 5.7d on page 88.

5.5.2 Wavelength analyses

As for the 1st and 2nd dominant wave directions of swell systems, a similar analysis has been performed aiming at analysing possible dependencies and impacts on altimeter retrievals with respect to the dominant wavelength per each partitioned wave spectra ($\lambda^{(p)}_{peak}$) retrieved from the two-dimensional ocean wave spectra available in the Sentinel-1 OSW component. Therefore, for both datasets of the collocated measurements under this study (S-1/J-3 and S-1/S-3), figure 5.9 shows how the altimeter parameters H_s and σ_0, and respective root mean square of residuals differ across the wavelength range (between short and long wavelengths), considering 100 m and 600 m respectively. With regard to Jason-3, it is important to note that despite the lower temporal separation of S-1/J-3 matchups, the number of collocated measurements is roughly ten times shorter than the one available for Sentinel-3, which may compromise some of the accomplished results, specially in those cases where little information is available on the considered domain of 1st and 2nd wave partition. Nevertheless, from figure 5.9a it is possible to observe a clear increase

of the magnitude of altimeter H_s with wavelength across each dimension, stronger for the 2nd dominant wavelength, and thus reaching higher values on the domain extremes where longer waves are linked to higher heights. In addition, a considerable H_s decrease, of ≈2 m can also be observed, when both 1st and 2nd wave partitions exceed simultaneously wavelengths of ≈400 m, a trend that becomes even clearer for Sentinel-3 SARM (Fig. 5.9e) where there is a higher density of measurements in this domain region. With regard to the standard deviation of H_s residuals of 1-Hz averages, figure 5.9b also shows that for Jason-3 there is a clear relation of H_s rms against wave partition wavelength, increasing its average value by almost 0.1 m in the domain extremes, which could be associated to noisier altimeter measurements when satellite overflies a sea-state with longer wavelengths. However, as represented by figure 5.9f, Sentinel-3 SARM corroborates these results, clearly showing an H_s rms increase of almost 0.2 m when 1st and 2nd wave partitions surpass together wavelengths of ≈400 m. Figures 5.9c and 5.9g, corresponding respectively to J-3 and S-3 SARM altimeter σ_0 retrievals, denotes similar patterns as for H_s, where a decrease ≈1.5 db is verified across each dimension of the wave partition, but when both dominant wavelengths contribute equally to the altimeter backscatter cross-section measurements, a clear trend is observed to higher σ_0 values, reaching a 3 db difference with respect to the global mean when both 1st and 2nd wave partitions exceed the wavelength threshold of 400 m.

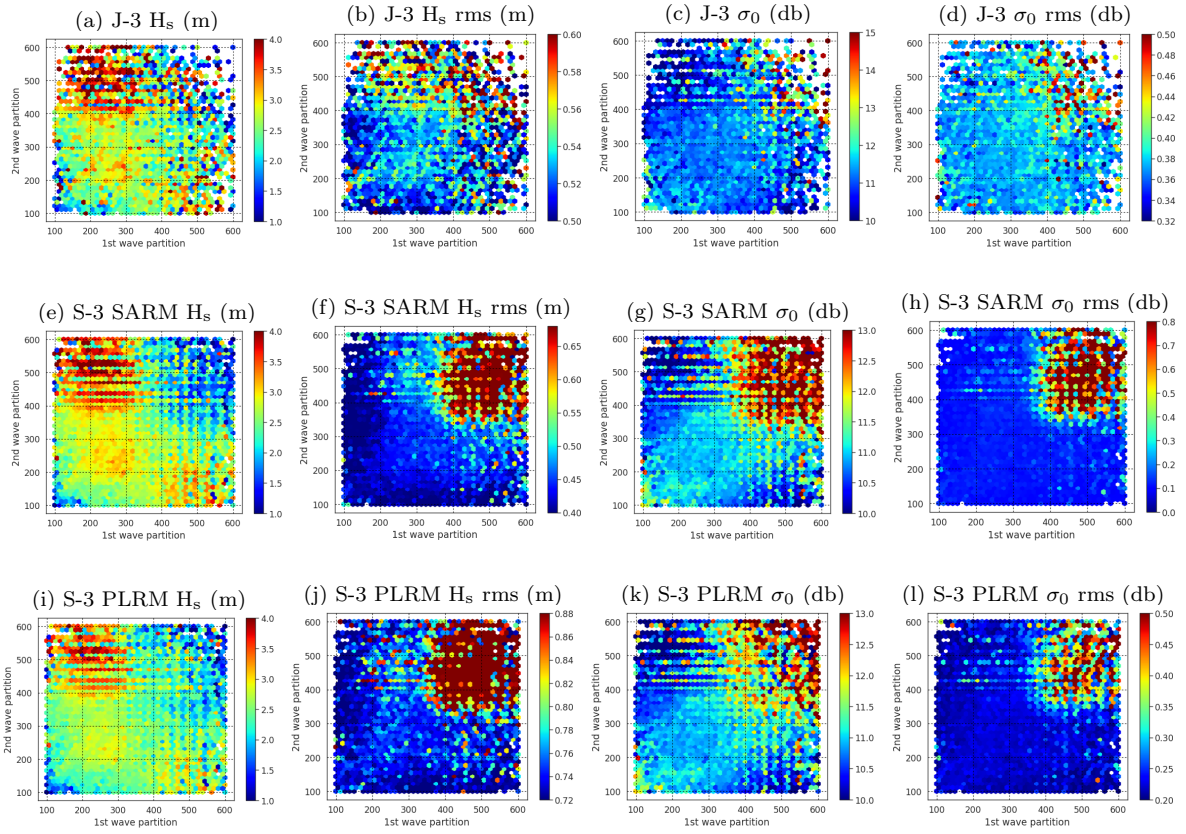

Figure 5.9: Bin averaged H_s, σ_0 and standard deviation of 1-Hz residuals of each parameter retrieved by Jason-3 and Sentinel-3 SARM/PLRM, plotted against the 1st and 2nd dominant wavelength of swell systems available in Sentinel-1 OSW component.

Although the increasing with wavelength effect becomes faded for σ_0 rms (Figs. 5.9d and 5.9h), S-3 SARM σ_0 standard deviation of the residuals show a similar trend as for H_s rms, increasing more than 0.8 db when 1st and 2nd dominant wave partitions surpass simultaneously wavelengths above 400 m. Finally, as verified for wave direction analysis in figure 5.5 on page 85, the achieved results for Sentinel-3 PLRM (Figs. 5.9i, 5.9j, 5.9k and 5.9l) follow the same trends as those for S-3 SARM in all analysed parameters, with a slight smoothing for H_s and σ_0 absolute values, and an increase of the respective rms of the altimeter retrievals for the considered wavelength domain.

In order to better evaluate the possible impact that 1st dominant swell wavelength may have on altimeter retrievals, a study of the standard deviation of H_s and σ_0 residuals of 1-Hz averages has been performed for increasing wavelength ranges. Figure 5.10 resumes the achieved results for Jason-3, Sentinel-3 SARM and PLRM.

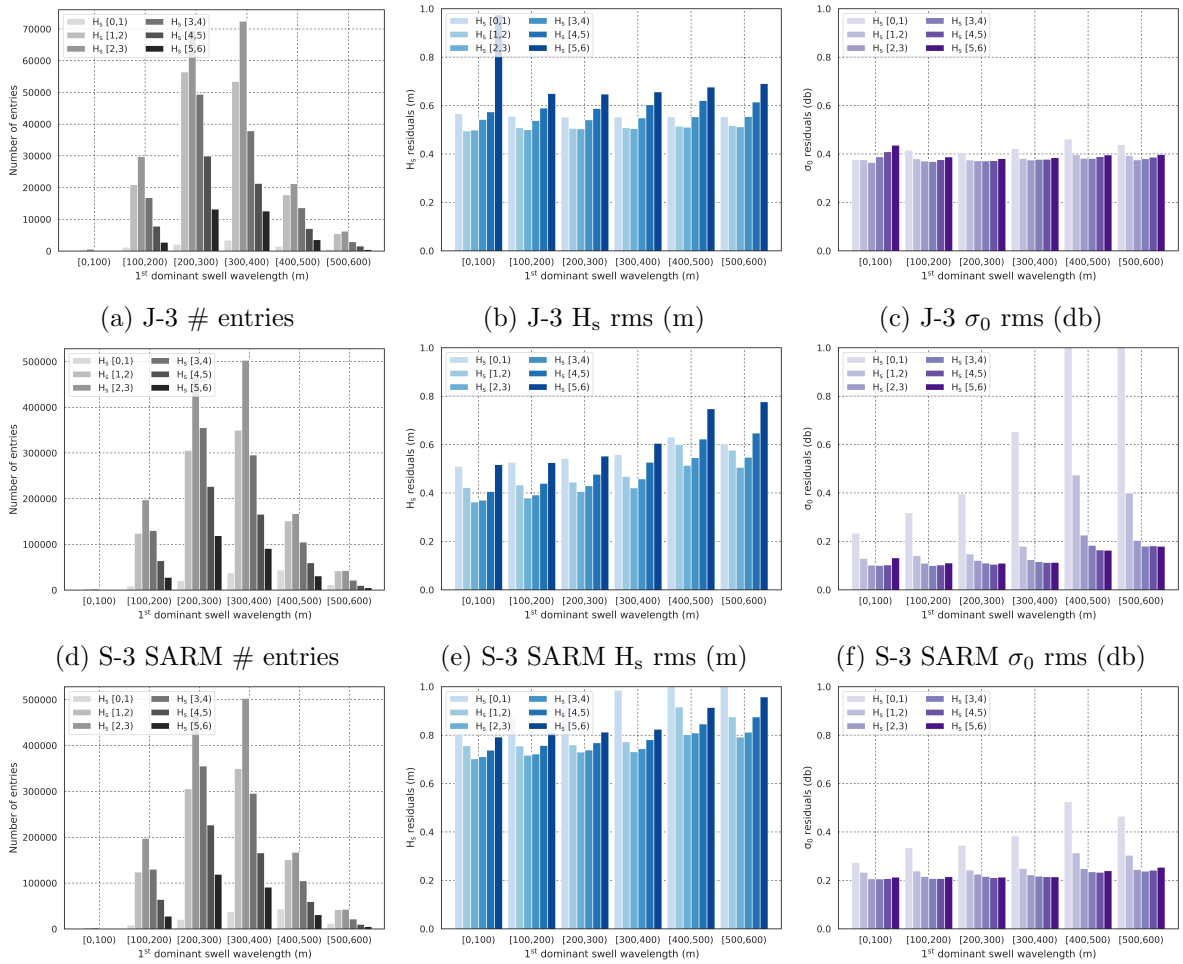

(a) J-3 # entries (b) J-3 H_s rms (m) (c) J-3 σ_0 rms (db)

(d) S-3 SARM # entries (e) S-3 SARM H_s rms (m) (f) S-3 SARM σ_0 rms (db)

(g) S-3 PLRM # entries (h) S-3 PLRM H_s rms (m) (i) S-3 PLRM σ_0 rms (db)

Figure 5.10: Standard deviation of H_s and σ_0 residuals of 1-Hz averages for 6 H_s intervals, for low, medium and high H_s values, against short, medium and long waves with 6 intervals of the 1st dominant wavelength, from 100 m to 600 m. The leftmost column show the number of observations (#) in each analysed class.

Similar to the analysis presented previously for the principal wave propagation directions, the same 6 H_s intervals established for low, medium and high significant wave heights have been considered, but this time tested against the 1st dominant wavelength partitions distributed in the following way: short wavelengths for limits between [0,100) m and [100,200) m, medium wavelengths for [200,300) m and [300,400) m, and high wavelengths for [400,500) m and [500,600) m. Several considerations may be drawn from figure 5.10, first, a very similar arrangement of the number of entries can be observed for both datasets S-1/J-3 and S-1/S-3 (Figs. 5.10a and 5.10d), where the highest number of collocated measures available are found in the middle wavelength ranges between [200,400)m, slightly decreasing when waves start to become extremely long or short, and denoting a lower frequency of its occurrence in the open ocean conditions considered in this study. It is important to note that despite the higher temporal separation of S-1/S-3 dataset due to less favourable orbital alignments between Sentinel-1 and Sentinel-3, the collocation procedure is still able to ensure an acceptable sample of the geophysical conditions, almost identical to the S-1/J-3 dataset where shorter separation times are achieved. With regard to the standard deviation of H_s residuals, figure 5.10b shows that J-3 performance is homogeneous for all considered wavelength ranges, remaining at an average level of ≈0.5 m, and slightly decaying when the altimeter H_s fall in the low/medium range of [1,3)m. For S-3 SARM, shown in figure 5.10e, the lowest H_s rms values are also observed when H_s is in the same middle range, but in this case it is possible to verify a clear global trend between the length of surface waves and the altimeter standard deviation of H_s residuals, indicating that SAR mode of Sentinel-3 could be more sensitive to the impact of longer waves on the altimeter H_s retrieval. As shown in figure 5.10f, a rising trend of different nature for S-3 SARM σ_0 rms with the 1st dominant wavelength is also observed, where low heights of H_s in the range of [0,2) m have σ_0 rms increases above 1 db as the surface waves become longer, but this effect is not observed in the medium/high H_s ranges, where σ_0 rms remains at a low level of ≈0.2 db.

Table 5.2: Mean values of Jason-3, Sentinel-3 SARM/PLRM standard deviation of H_s and σ_0 residuals of 1-Hz averages, computed for each wavelength range. Note: lengths and H_s rms in metres, σ_0 rms in decibels, and # defines the number of entries in thousand units.

	Jason-3			**Sentinel-3 SARM**			**Sentinel-3 PLRM**		
length	**#**	**H_s rms**	**σ_0 rms**	**#**	**H_s rms**	**σ_0 rms**	**#**	**H_s rms**	**σ_0 rms**
[000,100)	0.2	0.61	0.39	1	0.43	0.13	1	0.75	0.22
[100,200)	13	0.56	0.38	92	0.45	0.15	92	0.77	0.24
[200,300)	37	0.56	0.38	249	0.48	0.17	249	0.79	0.24
[300,400)	34	0.56	0.39	241	0.51	0.22	241	0.81	0.25
[400,500)	11	0.57	0.40	93	0.61	0.46	93	0.95	0.30
[500,600)	3	0.57	0.40	22	0.61	0.39	22	0.91	0.29

With regard to the results obtained for S-3 PLRM, figures 5.10h and 5.10i show similarities with S-3 SARM for both standard deviation of H_s and σ_0 residuals, with an expected increase of the global values between 0.2 m – 0.4 m for H_s rms, and ≈0.1 db for σ_0 rms, confirming the dataset smoothing effect previously referenced. Table 5.2 resumes the achieved results, aggregating H_s and σ_0 rms values for each of the 6 defined intervals of the dominant wavelength, from shorter to longer waves, and confirms the Sentinel-3 SARM trends, where both H_s rms and σ_0 rms show a clear upward trend as the surface waves become longer, starting from rms residuals of 0.43 m and 0.13 db for short waves in the wavelength range of [0,100)m, and reaching values of 0.61 m and 0.46 db for longer waves with wavelengths in the range of [400,600)m. These results may suggest a higher susceptibility of the SAR mode to fully developed seas where surface waves tend to propagate with large wavelengths.

In order to better understand the above results, figure 5.11 shows the altimeter global position of H_s from Jason-3 and Sentinel-3 SARM collocated measurements for longer waves, where 1st and 2nd dominant swell wavelength are above 400 m. For comparison, if we consider the full dataset shown in figure 5.7b on page 88, it is possible to observe that most of the matchups selected on these conditions have medium/low H_s, usually below 2 m height, and a large number of them are still located in the oceanic regions where waves are propagating eastwards, i.e., almost perpendicular to the altimeter ground track (Fig. 5.8 on page 89). Geographically, figure 5.11 shows that longer waves with relatively low H_s are mostly found in the tropical regions of northern Indian Ocean and western Pacific Ocean, but the largest area can be seen in the Southern ACC front at latitudes above −60° near the Antarctic Circle, where polar easterlies, mostly winds blowing in the East-West direction, have a strong effect on the ocean dynamics with waves propagating in the opposite direction due to influence of the Antarctic Circumpolar Current. From the altimeter point of view, specifically on S-3 SARM, these are the sea-state conditions causing larger impacts on the standard deviation of H_s and σ_0 residuals of 1-Hz averages, thus giving some indications that SAR altimetric sensors might be more sensitive than conventional LRM sensors to specific ocean conditions as the ones described above.

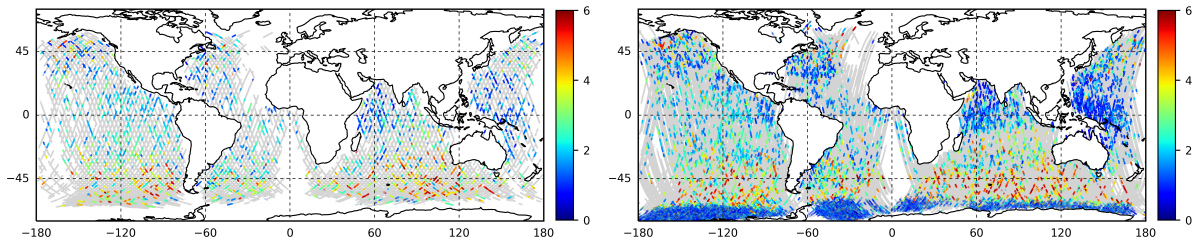

(a) J-3 H_s (m) (b) S-3 H_s (m)

Figure 5.11: Global distribution of altimeter H_s for the selected datasets of J-3 and S-3 collocated with S-1, where the 1st dominant swell wavelength is in the range of [400,600) m. Note: dots in grey correspond to the full dataset.

5.6 SSB and SSHA analysis

In view to better understand the sensitivity of SSB and SSHA to the 1st and 2nd dominant wave partitions, an analysis was carried out using the parameters available in RADS database. For the sea state bias, the SSB model developed by the Collecte Localisation Satellites (CLS), which is expressed by a non-parametric statistical approach in the form of a grid combining altimeter-derived H_s and U_{10} [22, 3] has been used. The choice of this model was due to two main reasons, the fact that it is one of the established SSB models widely used for this geophysical correction, and its availability for the two missions under investigation, J-3 and S-3 SARM, thus adding coherence to the analysis. With regard to SSHA, the RADS precomputed parameter, already available with all the corrections applied, including the SSB, and directly stored in RADS products, was used. Figure 5.12 shows the results both for SSB and SSHA, plotted against S-1 derived parameters, the 1st and 2nd dominant swell wave direction and wavelength. Being the SSB a 3-component correction, where the main contribution comes from the electromagnetic bias, which is highly dependent on the magnitude of H_s retrieval, figures 5.12a and 5.12e representing the J-3 and S-3 SARM SSB variability on the wave direction domain, show similar trends to those obtained previously on figures 5.5a and 5.5e (page 85) for H_s, where higher correction values are found for wave systems propagating almost perpendicular to the orbital ground track of the altimeter platform, in the range of $60° - 120°$. Since SSHA should not contain SSB effects, it would not be expected that this same pattern would be found in the SSHA plots.

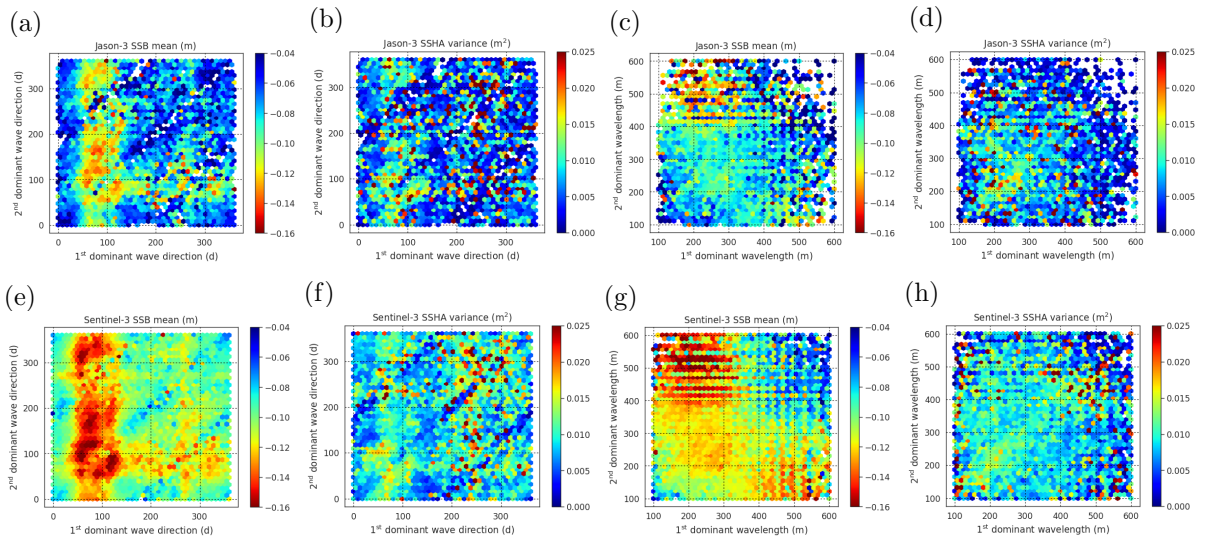

Figure 5.12: Bin averaged SSB and SSHA for Jason-3 and Sentinel-3 SARM, plotted against the 1st and 2nd dominant wave direction and wavelength of swell systems available in Sentinel-1 OSW component.

However, figures 5.12b (J-3) and 5.12f (S-3 SARM) clearly show an SSHA variance increase, in the order of a few tens of cm^2, for the same domain region where higher values of SSB are

settled. Since for SSB studies, no ground truth exists for validation purposes, the performance of different SSB models is analysed and evaluated according to the SSHA variance reduction, so the achieved results in this study may allow future perspectives on incorporating the dominant wave direction information in view to reduce the SSHA variance for the highlighted domains. Figure 5.12 also shows the plotted results for wavelength analysis, and as expected, the SSB variation across the 1st and 2nd dominant swell wavelength (Figs. 5.12c for J-3 and 5.12f for S-3 SARM) show identical patterns as the those found for H_s in the same domain (Figs. 5.9a and 5.9a on page 90), where the SSB increases for longer waves when the wave partitions are considered separately. But as exposed before for H_s, this SSB increase is not as pronounced when the 1st and 2nd dominant swell wavelength increase together, noting a serious reduction when both wave systems become simultaneously longer. Regarding SSHA, figures 5.12d (J-3) and 5.12h (S-3 SARM) show also a slight variance increase in these domains, mainly for wavelengths in the range of $100 - 400$ m, thus suggesting that SSB corrections are not entirely taking into account this particular sea-state conditions and need forthcoming attention if new model approaches will consider the impact of longer waves on the altimeter retrieved H_s and σ_0.

5.7 Conclusion

This paper presents an in-depth study on how the geophysical errors caused by the oceanic surface waves may affect both of the satellite altimeter observations, the significant wave height (H_s) and the signal backscatter cross section measurement (σ_0). The work has been performed for the entire year of 2017, and has been targeted specifically to the conventional low resolution mode (LRM) altimeter on board Jason-3, the SAR mode (SARM) and pseudo-LRM (PLRM) observations from the recent instrument of Sentinel-3A. The implementation was based on a collocation procedure between the measurements retrieved from each of these altimeters, with wave data provided by the Ocean Swell spectra (OSW) component, one of the components available in Sentinel-1 Level-2 Ocean (OCN) products.

It is known that non-linear ocean wave processes may play a role on altimeter retrievals, and consequently, may affect the sea state bias (SSB) empirical formulations to model the geophysical errors generated by wind-driven ocean gravity waves. For this study, two wave parameters have been used, the dominant wave direction and wavelength, both retrieved from the two-dimensional ocean wave spectra available on S-1 OSW component, which were studied against the altimeter H_s and σ_0, along with the associated standard deviation of the residuals of 1-Hz averages, aiming to evaluate the role of distinct ocean conditions on the targeted parameters and on the associated root mean square of 1-Hz altimeter observations, taken as indicators of the accuracy of these parameters.

The experimental investigations showed no particular evidence of wave direction and length effects on Jason-3 H_s and σ_0, since for the analysed dataset, the results are indistinct for shorter and longer waves propagating in any of the 4 considered cardinal directions. Nevertheless,

the results also show a variance increase of sea surface height anomaly (SSHA) when the 1st dominant swell waves have propagating directions in the range of $60° - 120°$, the region where H_s and the SSB correction are higher, thus indicating some leakage from SSB modulations to SSHA and opening new perspectives on the improvement of SSB algorithms adjusted to conventional altimeters for these particular sea-state conditions.

With regard to Sentinel-3 SARM, the SSB leakage to SSHA is also observed for the same domain region considered for wave direction, and for wavelength as well, where higher values of SSHA variance are found when both 1st and 2nd dominant wavelength increase simultaneously in the range of $100 - 400$ m, revealing some SSB dependencies in the altimeter H_s measurements when the two dominant wave systems contribute equally to this retrieval. The analysis of standard deviation of the residuals reveal higher values of σ_0 root mean square for all cardinal directions when the H_s retrieval is below 2 m, showing that S-3 SAR instrument could have an additional sensitivity to these ocean conditions when compared to the conventional LRM instrument of J-3. Adding to this, a linear dependency is found between all ranges of H_s and wavelength, since there is a clear increase of the residuals associated to this altimeter retrieval as the surface waves become longer. The same is observed for σ_0, where lower values of H_s propagate this altimeter residual across wavelength, reaching higher values for long waves. Since none of these outcomes are seen for Jason-3, a wavelength impact on S-3 SARM observations may be inferred, and should not be neglected when dedicated SSB modelling approaches are designed. Finally, the achieved results for S-3 PLRM do not add further information to these conclusions, since they produce smoothed observations when compared to SARM, but revealing a behaviour very similar to the latter in every aspect considered for this study, and therefore, should not be analysed in a comparison perspective with the conventional LRM instrument onboard Jason-3.

Acknowledgments

This work was funded by the European Space Agency (ESA) Support to Science Element (STSE) Program, in the scope of project SCOOP - SAR Altimetry Coastal & Open Ocean - Performance Exploitation and Roadmap Study.

Author Contributions

Nelson Pires and M. Joana Fernandes conceived the experiments; Nelson Pires designed and performed the experiments; All authors analysed the data and reviewed the study; Nelson Pires wrote the paper.

References

1. Chelton, D. (1994). The sea state bias in altimeter estimates of sea level from collinear analysis of TOPEX data. Journal of Geophysical Research, 99, 24995–25008. doi: 10.1029/94JC02113.

2. Gaspar, P.; Le Traon P.; Zanife, O. (1994). Estimating the sea state bias of the TOPEX and POSEIDON altimeteres from crossover differences. Journal of Geophysical Research, 99(12), 24981–24994. doi: 10.1029/94JC01430.

3. Labroue, S.; Gaspar, P.; Dorandeu, J.; Zanifé, O.; Mertz, F.; Vincent, P.; Choquet, D. (2004). Nonparametric estimates of the sea state bias for the Jason-1 radar altimeter. Marine Geodesy, 27(3–4), 453–481. doi: 10.1080/01490410490902089.

4. Tran, N.; Vandemark, D.; Chapron, B.; Labroue, S.; Feng, H.; Beckley, B.; Vincent, P. (2006). New models for satellite altimeter sea state bias correction developed using global wave model data. Journal of Geophysical Research, 111(C09009). doi: 10.1029/2005JC003406.

5. Tran, N.; Vandemark, D.; Labroue, S.; Feng, H.; Chapron, B.; Tolman, H.L.; Picot, N. (2010). Sea state bias in altimeter sea level estimates determined by combining wave model and satellite data. Journal of Geophysical Research, 115(C03020), 1–7. doi: 10.1029/2009JC005534.

6. Jiang, M.; Xu, K., Liu, Y.; Wang, L. (2016). Estimating the Sea State Bias of Jason-2 Altimeter From Crossover Differences by Using a Three-Dimensional Nonparametric Model. IEEE Journal Of Selected Topics In Applied Earth Observations And Remote Sensing, 9(11), 5023–5043. doi: 10.1109/JSTARS.2016.2557839.

7. Pires, N.; Fernandes, M.J.; Gommenginger, C.; Scharroo, R. (2016). A Conceptually Simple Modelling Approach for Jason-1 Sea State Bias Correction Based on 3 Parameters Exclusively Derived from Altimetric Information. Remote Sensing, 8(576), 1–13. doi: 10.3390/rs8070576.

8. Pires, N.; Fernandes, M.J.; Gommenginger, C.; Scharroo, R. (2018). Improved Sea State Bias Estimation for Altimeter Reference Missions With Altimeter-Only Three-Parameter Models. IEEE Transactions on Geoscience and Remote Sensing, PP, 1–15. doi: 10.1109/TGRS.2018.2866773.

9. Glazman, R.E.; Greysukh, A.; Zlotnicki, V. (1994). Evaluating models of sea state bias in satellite altimetry. Journal of Geophysical Research, 99(C6), 12581–12591. doi: 10.1029/94JC00478.

10. Glazman, R.; Fabrikant, A.; Srokosz, M. (1996). Numerical Analysis of the Sea State Bias for Satellite Altimetry. Journal of Geophysical Research, 101(C2), 3789–3799. doi: 10.1029/95JC03619.

11. Gommenginger, C. P.; Martin-Puig, C.; Amarouche, L.; Raney, R. K. (2013). Jason-CS SAR Mode Error Budget Study: Review of State of Knowledge for SAR Altimetry Over Ocean. National Oceanography Centre. EUMETSAT. Ref: EUM/RSP/REP/14/749304.

12. Bouzinac, C. (2013). CryoSat Product Handbook. ESRIN-ESA and Mullard Space Science Laboratory-University College London.

13. Bellingham, C.; Srokosz, M.; Gommenginger, C.; Cipollini, P.; Snaith, H. (2016). Jason-CS SAR Mode Sea State Bias Study: Final Report. National Oceanography Centre. EUMETSAT. Invitation to Tender: 14/209556.

14. Moreau, T.; Tran, N.; Aublanc, J.; Tison, C.; Le Gac, S.; Boy, F. (2018). Impact of long ocean waves on wave height retrieval from SAR altimetry data. Advances in Space Research, 62(6), 1434-1444. doi: 10.1016/j.asr.2018.06.004.

15. Scharroo, R. (2018) RADS Data and User Manuals, version 4.3.1, 4 September 2018.

16. Johnsen, H.; Collard, F. (2009) Sentinel-1 Ocean Swell Wave Spectra (OSW) Algorithm Definition. Northern Research Institute (NORUT) Tromso. ISSN: 1890-5226.

17. Queffeulou, P.; Ardhuin, F.; J.-M. Lefevre, J.M. (2011). Wave height measurements from altimeters: Validation status and applications. OSTST Meeting, Ocean Surface Topography Science Team, San Diego, California, 19–21 Oct.

18. Wang, H.; Zhu, J.; Yang, J. (2014). Error analysis on ESA's Envisat ASAR wave mode significant wave height retrievals using triple collocation model. Remote Sensing, 6, 12217–12233.

19. Johnsen H.; Engen G.; Guittion G. (2008). Sea-Surface Polarisation Ratio from Envisat ASAR AP Data. IEEE Trans. on Geo. Rem. Sensing, Vol.46, No.11, Nov.

20. Hersbach, H. (2010). Comparison of C-Band scatterometer CMOD5.N equivalent neutral winds with ECMWF. J. Atmos. Ocean Tech. 27, 721–736.

21. Mouche, A. (2015). Sentinel-1A: Status & Opportunities. MetOp-SG Scatterometer Science Advisory Group 2nd Meeting, 16-17 June.

22. Gaspar, P.; Labroue, S.; Ogor, F. (2002). Improving Nonparametric Estimates of the Sea State Bias in Radar Altimeter Measurements of Sea Level. Journal of Atmospheric and Oceanic Technology, 19, 1690–1707.

THIS PAGE IS INTENTIONALLY LEFT BLANK.

Chapter 6

Overall Conclusion and Perspectives

This thesis resumes all the work done over the last four years of research in the scope of the Ph.D. programme of Surveying Engineering at FCUP. The thorough study was entirely dedicated to sea state bias, through the developing and assessment of new techniques and methodologies to find new ways of minimizing the impact of the sea-state effect on the altimeter radar pulse.

Over the last 25 years trying to improve satellite altimetry measurements, different approaches based on theoretical, numerical and empirical techniques were developed in view to reduce this altimetric range error, but only empirical methods presently provide a practical solution to estimate SSB. In this sense, the work developed over the last 4 years, and presented in this thesis, intend to go further on SSB modelling based on empirical principles, proposing new ideas for the inclusion of sea-state effects not addressed by the standard altimetric retrievals alone, and able to overcome some of the limitations identified in current SSB models.

One of the main achievements of this work, was the concept, development, implementation and validation of a new global and multi-mission SSB model, based on three parameters solely derived from altimetric data. The proposed approach relies on a model design based on the classical altimeter retrievals H_s and U_{10}, but also on a third predictor acting as a mediator parameter gathered by the mean wave period (T_z) estimated directly from altimeter data. The methodology has been implemented through non-parametric statistical model techniques, using penalized regression splines embedded in a framework provided by generalized additive models, and employing a direct estimation based on SSH-MSS residuals, in order to obtain a reliable SSHA input for model development.

After a thorough investigation regarding the modulation criteria, where several approaches were tested for selecting the best design concerning the different model inputs and their interactions related with the final response, it is shown that the proposed methodology achieves promising results in several aspects: (1) an SLA variance reduction was verified for most of the oceanic regions, allowing to conclude that the achieved results show clear improvements when the model gathers extra information from sea-state conditions through the mean wave period; (2) being the SSB an instrumental dependent error, the proposed approach was also designed to

be applied to all reference missions, showing that it is flexible enough to be adopted for TOPEX, Jason-1, Jason-2 and Jason-3 missions; (3) the suggested methodology also benefits from the high resolution of SSHA estimations provided by the amount of data available through the direct method, turning possible to derive a robust SSB model with only 20 cycles of data, turning it as valuable option to rapidly estimate SSB for newly-launched missions.

Despite the observed improvements and favourable performance benchmarks, the proposed approach has some limitations that should be taken into account: the applied mean wave period algorithms were initially developed for TOPEX and Jason-1, and given the satisfactory behaviour when confronted with T_z retrieved from numerical wave models on periods outside the time range of these missions, it is still recommended to design an exclusive algorithm to be adapted for each mission and after ingested by the SSB model. Additionally, it is known that these algorithms are better suited for wind-dominated seas than to swell regions, increasing the noise of SSB estimations when the model uses T_z algorithms for all sea-state regimes.

Aiming to better understand the swell effects on the altimeter retrievals used for SSB estimations, H_s and U_{10} derived from σ_0, the ocean products from Sentinel-1 L2 have been used in synergy with Jason-3 and Sentinel-3. From this study, several conclusions have been drawn: (1) the swell wave systems produce no impact on Jason-3, meaning that conventional LRM altimeter retrievals are indistinct for shorter and longer waves propagating in any of the 4 considered cardinal directions; (2) the swell wavelength has repercussions on Sentinel-3 SARM altimeter standard deviations of H_s and σ_0 residuals, specially when the dominant swell wave system become longer; (3) the swell wavelength also has a role on the altimeter H_s, since for all the considered wavelength ranges, the H_s below 2 m reveal higher values of σ_0 root mean square; (4) this H_s and σ_0 dependency on swell wave direction and wavelength is also observed on SSHA, which may have repercussions on SSB estimates and should not be neglected.

The technique of satellite altimetry is constantly evolving, new technologies and processing methodologies are emerging as the new future into ocean surface topography measurements. Delay-Doppler altimetry exploiting coherent processing of groups of transmitted pulses, very high-frequency electromagnetic waves such as Ka-band altimetry, new retrackers bringing altimeter-derived measurements of sea level into coastal regions, or innovative sensors as the upcoming SAR interleaved mode of Sentinel-6/Jason-CS scheduled to be launched in November 2020 and the wide-swath Surface Water Ocean Topography (SWOT) mission scheduled for launch in 2021, are examples of the scientific advances expected in this remote sensing technique in the near future, and the study of SSB will be relevant for all of them.

As a future perspective, it is expected to conduct further developments on SSB modelling and on improving the altimeter-derived measurements in view to extract the largest amount of information from the altimeter signal for SSB studies. It is intended to continue with the development of the proposed SSB model with additional predictors and new calibration methods, allowing its implementation for different altimetric missions and instruments. It is also expected to expand the studies for coastal regions and inland waters, since the SSB is an altimetric

bias caused by the oceanic conditions at regional scales, the electromagnetic bias is affected by waves and wind propagation in coastal zones, waves/currents interactions and regions defined by the continental shelf, slope and shape. Due to these constrains, the main challenge to find a reliable SSB model applied to coastal regions and inland waters can be described into three main research topics: (1) understand the coastal and enclosed retracking impacts on H_s, U_{10} and range; (2) the requirement to use additional sea state descriptors to better describe the physics on these regions (wave period and direction, wavelength and others); (3) understand the different sea-state descriptors and their correlations with SSB.

This dissertation also shows promising results for further studies in the instrumental component of SSB, the so-called *tracker bias*. The use of mission tandem phases with a dedicated SSB model for each mission showed residuals in the order of a few centimetres, the same order of magnitude estimated for this SSB component. Therefore, for regions with low prevalence of swell fields, mostly of them found in the mid-latitude regions, but also in enclosed seas, it is possible to raise the assumption that electromagnetic and skewness biases have lower contributions to SSB due to lower ocean dynamics. These cases provide the ideal conditions to further explore this SSB instrumental component, which is affected by possible changes on retracking algorithms and assumptions made in the processing methodologies adopted in the retrieval of the geophysical information from averaged ocean waveforms.

With regard to the mean wave period algorithms derived from altimetry-only information, it is expected to develop new and flexible approaches designed for each altimetric mission in order to be later integrated into SSB models. This line of research may incorporate empirical observations and/or analytical approaches based on recent advances on the theory of weak turbulence for wind-driven waves, which predicts the link of instant wave energy to instant energy flux to/from waves. Since this kind of approach operates with wave height and its spatial derivative, does not refer to normalized radar cross-section (σ_0) measured by the altimeter, not containing any empirical parameters and not requiring any features of a particular satellite altimeter or calibration for specific region. The exploitation of these theoretical methods could be of fundamental importance for SSB characterization, as being independent of altimetric information will allow to evaluate how the mean wave period estimated from the empirical methods is affected by the H_s and σ_0 retrieved by the altimeter.

Finally, it is expected to proceed with synergetic combinations of satellite altimetry with other remote sensing techniques. The promising results achieved from information provided by Sentinel-1 Level-2 ocean products in order to better understand the swell impact on altimeter retrievals, open good perspectives to go deeper on this approach. The technique of satellite altimetry has been shown capable of providing a near global view of sea surface topography, significant wave height and wind velocity, but the effect of local sea state on altimetric measurements may be better known with the help of other satellite oceanography techniques and missions. The better understanding of SAR-imaging mechanisms for two-dimensional views of the ocean surface waves and ocean currents, or the scatterometers designed to gather data on the speed and direction of winds responsible for ocean waves formation, could be an added-value

for future SSB studies. Lastly, the Chinese-French Oceanography Satellite (CFOSAT) mission, launched on 29 October 2018, promises to expand the fundamental knowledge on surface processes linked to wind and waves, and will certainly deepen the development of new methodologies for the characterizations of sea-state effects on radar signals.

In conclusion, the last four years of research work presented in this document, should not be seen as an end of itself, but rather as the beginning of new perspectives for forthcoming studies on interpreting the errors induced by the ocean sea-surface roughness on satellite altimetry and how they affect the altimetric observations, continuing this way with the path to ensure the retrieval of high accurate and reliable oceanographic information from remote sensing platforms for the years to come.

References

[1] V. Rosmorduc, J. Benveniste, E. Bronner, et al. *Radar Altimetry Tutorial*. J. Benveniste and N. Picot (Editors), http://www.altimetry.info. 2016.

[2] D. Chelton, J. Ries, P. Callahan, et al. "Satellite Altimetry and Earth Science: A Handbook of Techniques and Applications". In: ed. by L. Fu and A. Cazenave. Academic Press Inc., 2001. Chap. Satellite Altimetry. ISBN: 0122695453.

[3] W. K. Melville, R. H. Stewart, .W C. Keller, et al. "Measurements of electromagnetic bias in radar altimetry". In: *Journal of Geophysical Research* 96.C3 (1991), p. 4915. ISSN: 0148-0227. DOI: 10.1029/90JC02114.

[4] A. Ghavidel, D. Schiavulli, and A. Camps. "Numerical Computation of the Electromagnetic Bias in GNSS-R Altimetry". In: *IEEE Transactions on Geoscience and Remote Sensing* 54.1 (2016), pp. 489–498. DOI: 10.1109/TGRS.2015.2460212.

[5] J. Morison, R. Kwok, S. Dickinson, et al. "Sea State Bias of ICESat in the Subarctic Seas". In: *IEEE Geoscience and Remote Sensing Letters* 15.8 (2018), pp. 1144–1148. ISSN: 1545-598X. DOI: 10.1109/LGRS.2018.2834362.

[6] R. Glazman, A. Fabrikant, and M. Srokosz. "Numerical Analysis of the Sea State Bias for Satellite Altimetry". In: *Journal of Geophysical Research* 101.C2 (1996), pp. 3789–3799. DOI: 10.1029/95JC03619.

[7] N. Tran, D. Vandemark, B. Chapron, et al. "New models for satellite altimeter sea state bias correction developed using global wave model data". In: *Journal of Geophysical Research* 111.C09009 (2006). DOI: 10.1029/2005JC003406.

[8] N. Tran, D. Vandemark, S. Labroue, et al. "Sea state bias in altimeter sea level estimates determined by combining wave model and satellite data". In: *Journal of Geophysical Research* 115.C03020 (2010), pp. 1–7. DOI: 10.1029/2009JC005534.

[9] M. Jiang, K. Xu, Y. Liu, et al. "Estimating the Sea State Bias of Jason-2 Altimeter From Crossover Differences by Using a Three-Dimensional Nonparametric Model". In: *IEEE Journal Of Selected Topics In Applied Earth Observations And Remote Sensing* 9.11 (2016), pp. 5023–5043.

[10] P. Gaspar, P. Le Traon, and O. Zanife. "Estimating the sea state bias of the TOPEX and POSEIDON altimeteres from crossover differences". In: *Journal of Geophysical Research* 99.12 (1994), pp. 24981–24994. DOI: 10.1029/94JC01430.

[11] D. B. Chelton. "The sea state bias in altimeter estimates of sea level from collinear analysis of TOPEX data". In: *Journal of Geophysical Research: Oceans* 99.C12 (1994), pp. 24995–25008. DOI: 10.1029/94JC02113.

[12] P. Gaspar and J. Florens. "Estimation of the sea state bias in radar altimeter measurements of sea level: Results from a new nonparametric method". In: *Journal of Geophysical Research* 103.98 (1998), pp. 803–814. DOI: 10.1029/98JC01194.

[13] P. Gaspar, S. Labroue, and F. Ogor. "Improving Nonparametric Estimates of the Sea State Bias in Radar Altimeter Measurements of Sea Level". In: *Journal of Atmospheric and Oceanic Technology* 19 (2002), pp. 1690–1707. DOI: 10.1175/1520-0426.

[14] S. Labroue, P. Gaspar, J. Dorandeu, et al. "Nonparametric estimates of the sea state bias for the Jason-1 radar altimeter". In: *Marine Geodesy* 27.3-4 (2004), pp. 453–481. DOI: 10.1080/01490410490902089.

[15] H. Feng, S. Yao, L. Li, et al. "Spline-Based Nonparametric Estimation of the Altimeter Sea-State Bias Correction". In: *IEEE Geoscience and Remote Sensing Letters* 7.3 (2010), pp. 577–581. DOI: 10.1109/LGRS.2010.2041894.

[16] S. Martin. *An Introduction to Ocean Remote Sensing*. Cambridge University Press, 2014. ISBN: 9781107019386.

[17] H. R. Stanley. "The Geos-3 Project". In: *Journal of Geophysical Research: Solid Earth* 84.B8 (1979), pp. 3779–3783. DOI: 10.1029/JB084iB08p03779.

[18] J. Benveniste. "Coastal Altimetry". In: ed. by S. Vignudelli, A. Kostianoy, P. Cipollini, et al. Springer-Verlag, 2011. Chap. Radar Altimetry: Past, Present and Future. ISBN: 9783642127953.

[19] R. Scharroo. "A Decade of ERS Satellite Orbits and Altimetry". PhD thesis. TU Delft, 2002. ISBN: 9040723699.

[20] G. Brown. "The average impulse response of a rough surface and its applications". In: *IEEE Transactions on Antennas and Propagation* 25.1 (1977), pp. 67–74. DOI: 10.1109/TAP.1977.1141536.

[21] D. Chelton, E. Walsh, and J. MacArthur. "Pulse Compression and Sea Level Tracking in Satellite Altimetry". In: *Journal of Atmospheric and Oceanic Technology* 6 (1989), pp. 407–438. DOI: 10.1175/1520-0426.

[22] I. Young. *Wind Generated Ocean Waves*. Elsevier B.V., 1999, p. 307. ISBN: 0080429998.

[23] O. Phillips. "On the generation of waves by turbulent wind". In: *Journal of Fluid Mechanics* 2.5 (1957), 417–445. DOI: 10.1017/S0022112057000233.

[24] J. Miles. "On the generation of surface waves by shear flows". In: *Journal of Fluid Mechanics* 3.2 (1957), 185–204. DOI: 10.1017/S0022112057000567.

[25] K. Hasselmann, P. Barnett, E. Bouws, et al. "Measurements of wind-wave growth and swell decay during the Joint North Sea Wave Project (JONSWAP)". In: 8 (1973), pp. 1–95.

[26] L. H. Holthuijsen. *Waves in Oceanic and Coastal Waters*. Cambridge University Press, 2007. ISBN: 9780521129954.

[27] N. Nordenstrom. *Methods for Predicting Long Term Distributions of Wave Loads and Probability of Failure for Ships: Part 2. Relations between visually estimated and theoretical wave heights and periods*. Research Department, Report n. 69-22-S. Det Norske Veritas, 1971.

[28] C. Bretschneider. *Generation of Waves by Wind - State of the Art*. Office of Naval Research, Department of the Navy, Washington, 1964.

[29] T. Kitano, H. Mase, and W. Kioka. In: *Ocean Wave Measurement and Analysis*. Proc. 4th Int. Symp. Ocean Wave Measurement and Analysis WAVES, San Francisco, 2001. Chap. Theory of Significant Wave Period Based on Spectral Integrals.

[30] Y. Goda. "Statistical Variability of Sea State Parameters as a Function of Wave Spectrum". In: *Coastal Engineering in Japan* 31.1 (1988), pp. 39–52. DOI: 10.1080/05785634.1988.11924482.

[31] A. J. Kuik, G. PH. van Vledder, and L. H. Holthuijsen. "A Method for the Routine Analysis of Pitch-and-Roll Buoy Wave Data". In: *Journal of Physical Oceanography* 18.7 (1988), pp. 1020–1034. DOI: 10.1175/1520-0485.

[32] J. Portilla-Yandún, A. Salazar, and L. Cavaleri. "Climate patterns derived from ocean wave spectra". In: *Geophysical Research Letters* 43.22 (2016), pp. 11736–11743. DOI: 10.1002/2016GL071419.

[33] S. Hasselmann, C. Bruning, K. Hasselmann, et al. "An improved algorithm for the retrieval of ocean wave spectra from synthetic aperture radar image spectra". In: *Journal of Geophysical Research* 101.C7 (1996), pp. 16615–16629. DOI: 10.1029/96JC00798.

[34] J. Schulz-Stellenfleth, S. Lehner, and D. Hoja. "A parametric scheme for the retrieval of two-dimensional ocean wave spectra from synthetic aperture radar look cross spectra". In: *Journal of Geophysical Research* 110.C05004 (2005), pp. 1–17. DOI: 10.1029/2004JC002822.

[35] B. Chapron, H. Johnsen, and R. Garello. "Wave and wind retrieval from SAR images of the ocean". In: *Annales des telecommunications* 56.11-12 (2001), pp. 682–699. DOI: 10.1007/BF02995562.

[36] F. Collard, F. Ardhuin, and B. Chapron. "Extraction of Coastal Ocean Wave Fields From SAR Images". In: *IEEE Journal of Oceanic Engineering* 30.3 (2005), pp. 526–533. DOI: 10.1109/JOE.2005.857503.

[37] G. Engen and H. Johnsen. "SAR-Ocean Wave Inversion Using Image Cross Spectra". In: *IEEE Transactions on Geoscience and Remote Sensing* 33.4 (1995), pp. 1047–1056. DOI: 10.1109/36.406690.

[38] H. Johnsen and F. Collard. *Sentinel-1 Ocean Swell Wave Spectra (OSW) Algorithm Definition*. Northern Research Institute (Norut). 2009.

[39] D. Stammer and A. Cazenave. *Satellite Altimetry over Oceans and Land Surfaces*. CRC Press, 2018. ISBN: 9781498743457.

[40] M. Srokosz and M. S. Longuet-Higgins. "On the skewness of sea-surface elevation". In: *Journal of Fluid Mechanics* 164 (1986), p. 487. ISSN: 0022-1120.

[41] F. C. Jackson. "The reflection of impulses from a nonlinear random sea". In: *Journal of Geophysical Research: Oceans* 84.C8 (1979), pp. 4939–4943.

[42] D. E. Barrick and B. J. Lipa. "Chapter 3 Analysis and Interpretation of Altimeter Sea Echo". In: *Satellite Oceanic Remote Sensing*. Ed. by Barry Saltzman. Vol. 27. Advances in Geophysics. Elsevier, 1985, pp. 61–100. DOI: 10.1016/S0065-2687(08)60403-3.

[43] M. S. Longuet-Higgins. "The effect of non-linearities on statistical distributions in the theory of sea waves". In: *Journal of Fluid Mechanics* 17.3 (1963), 459–480. DOI: 10.1017/S0022112063001452.

[44] T. Elfouhaily, D. Thompson, B. Chapron, et al. "Improved electromagnetic bias theory". In: *Journal of Geophysical Research* 105 (2000), pp. 1299–1310. DOI: 10.1029/1999JC900277.

[45] T. Elfouhaily, D. Thompson, B. Chapron, et al. "Improved electromagnetic bias theory: Inclusion of hydrodynamic modulations". In: *Journal of Geophysical Research* 106.C3 (2001), pp. 4655–4664. DOI: 10.1029/1999JC000086.

[46] C. P. Gommenginger, M. Srokosz, J. Wolf, et al. "An investigation of altimeter sea state bias theories". In: *Journal of Geophysical Research* 108 (2003), pp. 1–13. DOI: 10.1029/2001JC001174.

[47] M. Srokosz. "On the joint distribution of surface elevation and slopes for a nonlinear random sea, with an application to radar altimetry". In: *Journal of Geophysical Research* 91.C1 (1986). ISSN: 0148-0227. DOI: 10.1029/JC091iC01p00995.

[48] G. H. Born, M. A. Richards, and G. W. Rosborough. "An empirical determination of the effects of sea state bias on SEASAT altimetry". In: *Journal of Geophysical Research: Oceans* 87.C5 (1982), pp. 3221–3226. DOI: 10.1029/JC087iC05p03221.

[49] N. Pires, M. J. Fernandes, C. Gommenginger, et al. "A Conceptually Simple Modeling Approach for Jason-1 Sea State Bias Correction Based on 3 Parameters Exclusively Derived from Altimetric Information". In: *Remote Sensing* 8.7 (2016), pp. 2072–4292. DOI: 10.3390/rs8070576.

[50] N. Pires, M. J. Fernandes, C. Gommenginger, et al. "Improved Sea State Bias Estimation for Altimeter Reference Missions With Altimeter-Only Three-Parameter Models". In: *IEEE Transactions on Geoscience and Remote Sensing* (2018), pp. 1–15. ISSN: 0196-2892. DOI: 10.1109/TGRS.2018.2866773.

[51] R. Scharroo and J. Lillibridge. "Non-Parametric Sea-State Bias models and their relevance to sea level change studies". In: *Proceedings of the 2004 Envisat & ERS Symposium*. Vol. 2004. April. 2005.